Template-assisted grown III-V semiconductor nanowires: A transmission electron microscopy study

Thèse N° 9454

Présentée le 17 mai 2019

à la Faculté des sciences et techniques de l'ingénieur
Laboratoire des matériaux semiconducteurs
Programme doctoral en science et génie des matériaux

pour l'obtention du grade de Docteur ès Sciences

par

Nicolas BOLOGNA

Acceptée sur proposition du jury

Dr Y. Leterrier, président du jury
Prof. A. Fontcuberta i Morral, Dr. M.-D. Rossell Abrodos, directrices de thèse
Prof. J. Arbiol, rapporteur
Dr D. Cooper, rapporteur
Dr M. Cantoni, rapporteur

2019

ÉCOLE POLYTECHNIQUE
FÉDÉRALE DE LAUSANNE

Acknowledgments

The realization of this project was possible thanks to the constant presence of a lot of people I interacted with during these four years. I would like to thank **Rolf Erni** and **Marta Rossell** for giving me the possibility to join the group and their supervision throughout the entire project. You were always supporting me with the development of my research skills in order to always extract the best out of my project. I really appreciated every new topic you were able to explain to me and the friendly environment you were able to create within the group. In fact, the **Electron Microscopy Center** at Empa was one of the best research groups I have been working in. The professional, as well as personal interactions, were daily habits that each research group should have. I would like to thank **Roksolana Kojak, Debora Keller, Yucheng Zhang, Marta Bon, Yadira Arroyo, Feng Wang, Alex Vogel,** and **Trond Henninen**. Thanks to **Piyush Agrawal** for what he taught me about computer simulations, for the funny evenings spent in Lausanne and the dinners based on traditional Indian (very spicy…) food. I really appreciated the time with **Gabriele Ilari**, who gave me also the first trainings at the beginning of my first year of Ph.D. Thanks also to **Nabeel Ahmad** for our discussions on a wide variety of topics and **Robin Pauer** for the help he was always able to provide to me, especially in efficiently ordering every kind of tool once needed. **Marco Campanini** revealed himself to be a very important colleague and friend during the last three years. We shared a lot of professional moments where he was able to explain to me a large amount of information on how TEM works at the possible deepest level. However, our relationship was also constituted of funny moments spent on the Zürich lake and in Australia. I'll never forget the amount of Matcha ice-cream you were able to eat.

Being part of a collaborative project allowed me to get in touch with very smart people also from the **IBM-Research** laboratory in Rüschlikon. I would like to thank all the former and present members of the **M.I.N.D. Group** of the **S&T Department**. In particular, I am really thankful for the guidance given by **Heike Riel** and **Walter Reiss** throughout these four years. I would like to thank **Kirsten Moselund**, who took the leadership of our group and improved its research skills. She also gave a special effort to strengthen the bonding between colleagues outside of the working environment. All the members of the group were really important for the development of this project and, among the others, I want to thank **Davide Cutaia, Lukas Czornomaz, Stephan Wirths, Philipp Staudinger, Nico Mosso, Yannick Baumgartner, Andrea Gemma, Elisabetta Corti, Fabian Könemann** and **Cezar Zota**. I had a lot of professional discussions with all of them and I certainly improved my scientific knowledge. **Clarissa Convertino** and **Svenja Mauthe**, my office-mates for the last three years, were always able to lighten our

afternoons, even during the most intense periods. **Maryline Sousa** and **Steffen Reidt** represented important pillars for teaching me how to use the FIB and prepare the electron-transparent lamellas. We all know how this instrument can easily lead a scientist to a brain-burnout. **Heinz Schmid** for our continuous discussions on the faceting of the nanowires I investigated with the TEM**.** I will always remember the patience you had in explaining me the crystal growth dynamics and for making me grow as a professional scientist.

Special thanks are certainly addressed to **Anna Fontcuberta i Morral** and the whole **LMSC group** at EPFL for the useful discussions and the constant support in order to improve my project.

I would like also to express my gratitude to **Jordi Arbiol** and the **GAeN group** at ICN2 for the useful training on 3D modeling with Rhodius software.

Then, I would like to thank **my friends** in Italy. They have been part of the largest portion of my life and, despite the distance, we always try to catch up and have fun when I come back in Monza.

Big thanks go to **my entire family** and in particular my parents (**Ceferino** and **Sandra**) and my two sisters (**Alessandra** and **Serena**) who were always willing to help me when I needed. Finally, I would like to thank my wife, **Licia**, for always standing by my side during our professional and private decisions.

Lausanne, le 17 Mai 2019

Abstract

III-V semiconductor nanowires are, due to their unique properties, one of the most promising nanostructures developed in the last decades. However, the realization of commercial devices made of III-V nanowires, such as transistors and solar cells, has not become feasible yet. In fact, the incompatibility with the CMOS industrial process and the low control on their crystallographic defects, able to strongly reduce the device performance, represent key obstacles to their implementation. In this thesis, an innovative catalyst-free method called template-assisted selective epitaxy (TASE) is used to grow CMOS-compatible nanowires on different Si substrate orientations by achieving a very high level of confidence on the structural quality at the atomic level. The nanowires are grown by metal-organic chemical vapor deposition and characterized in detail by various transmission electron microscopy techniques.

In the first part of this thesis, we demonstrate the first planar defect-free GaAs nanowires grown on a CMOS-compatible substrate. The polytypism and the high density of planar defects are successfully suppressed thanks to the high degree of freedom allowed by the TASE method. In fact, TASE allows for a wide growth parameter window, still maintaining control of the morphology and growth direction of the nanowire. We also analyzed the atomic structure and composition of stair-rod dislocations, a particular type of defect occurring under certain growth parameters. A correlation with the electronic properties of the defect is achieved by the aid of DFT simulations. They suggest the possibility to obtain strongly localized mono-dimensional charge channels running along these particular defects, which could be relevant for electronic applications.

The second part of the thesis is dedicated to the investigation of the effects induced by p- and n-dopants on the structure and properties of $Ga_xIn_{(1-x)}P$ and GaAs nanowires. We demonstrate that TASE permits a good control of the doping incorporation and that dopant atoms modify the crystal structure and composition of the nanowires. Moreover, we present a series of off-axis holography experiments for the mapping of potential fields in doped nanowires.

We consider these results to play a key role in the advancement of III-V nanowires integration in electronic and optoelectronic devices and anticipate that this innovative growth method will open new paths for novel device architectures.

Keywords: III-V semiconductors, nanowires, doping, transmission electron microscopy, tunnel field-effect transistor, solar cells, crystallographic defects, electron energy-loss spectroscopy, energy dispersive x-ray spectroscopy, off-axis holography

Zusammenfassung

III-V-Halbleiternanodrähte sind aufgrund ihrer einzigartigen Eigenschaften eine der vielversprechendsten Nanostrukturen, die in den letzten Jahrzehnten entwickelt wurden. Die Realisierung kommerzieller Geräte aus III-V-Nanodrähten wie Transistoren und Solarzellen ist jedoch noch nicht möglich. Tatsächlich stellen die Inkompatibilität mit dem industriellen CMOS-Prozess und die geringe Kontrolle über ihre kristallographischen Defekte, die die Leistung der Geräte stark reduzieren können, wichtige Hindernisse für ihre Umsetzung dar. In dieser Arbeit wird eine innovative katalysatorfreie Methode namens TASE (Template-assisted Selective Epitaxy) verwendet, um CMOS-kompatible Nanodrähte auf verschiedenen Si-Substratausrichtungen zu züchten, wodurch ein sehr hohes Maß an Sicherheit der Strukturqualität auf atomarer Ebene erreicht wird. Die Nanodrähte werden durch metallorganische chemische Gasphasenabscheidung gezüchtet und anschliessend durch verschiedene Verfahren der Transmissionselektronenmikroskopie detailliert charakterisiert.

Im ersten Teil dieser Arbeit zeigen wir die ersten planaren, defektfreien GaAs-Nanodrähte, die auf einem CMOS-kompatiblen Substrat gewachsen sind. Der Polytypismus und die hohe Dichte an planaren Defekten werden durch den hohen Freiheitsgrad der TASE-Methode erfolgreich unterdrückt. TASE ermöglicht ein breites Fenster der Wachstumsparameter, wobei die Kontrolle über die Morphologie und die Wachstumsrichtung des Nanodrahts erhalten bleibt. Ebenso haben wir die atomare Struktur und Zusammensetzung von sogenannten Treppenstabversetzungen analysiert, eine bestimmte Art von Defekt, der unter bestimmten Wachstumsparametern auftritt. Eine Korrelation mit den elektronischen Eigenschaften des Defekts wird mit Hilfe von DFT-Simulationen erreicht. Sie legen die Möglichkeit nahe, entlang dieser speziellen Defekte stark lokalisierte, eindimensionale Ladungskanäle zu erhalten, die für elektronische Anwendungen relevant sein könnten.

Der zweite Teil der Arbeit beschäftigt sich mit der Untersuchung der Auswirkungen von p- und n-Dotierungen auf die Struktur und Eigenschaften von $Ga_xIn_{(1-x)}P$- und GaAs-Nanodrähten. Wir zeigen, dass TASE eine gute Kontrolle der Dotierung erlaubt und dass Dotieratome die Kristallstruktur und Zusammensetzung der Nanodrähte verändern. Darüber hinaus präsentieren wir Studie Off-Axis-Holographie zur Abbildung potentieller Felder in dotierten Nanodrähten.

Wir sind der Ansicht, dass diese Ergebnisse eine Schlüsselrolle bei der Weiterentwicklung der Integration von III-V-Nanodrähten in elektronische und optoelektronische Bauelemente spielen und gehen davon aus, dass diese innovative Wachstumsmethode neue Wege für neuartige Bauelementarchitekturen eröffnen wird.

Schlüsselwörter: III-V-Halbleiter, Nanodrähte, Dotierung, Transmissionselektronenmikroskopie, Tunnelfeldeffekttransistor, Solarzellen, kristallographische Defekte, Elektronenenergieverlust-Spektroskopie, energiedispersive Röntgenspektroskopie, Off-Axis-Holographie

Riassunto

I nanofili a semiconduttore III-V sono, grazie alle loro proprietá uniche, una delle nanostrutture piu promettenti sviluppate nelle ultime decadi. Tuttavia, la realizzazione di dispositivi commerciali realizzati con nanofili III-V, come transistor e celle solari, é ancora inattuabile. Infatti, l'incompatibilitá con i tradizionali processi CMOS industriali e il basso controllo sulla densitá di difetti presenti, in grado di ridurre fortemente la prestazione del dispositivo, rappresentano ostacoli chiave alla loro implementazione. In questa tesi, un metodo innovativo esente da particelle catalitiche chiamato "template-assisted selective epitaxy (TASE)" é usato per crescere i nanofili su diversi substrati di silicio in modo del tutto compatibile con gli standard industriali, ottenendo inoltre un elevato livello di fiducia sulla qualitá strutturale a livello atomico. In questo progetto, i nanofili sono cresciuti tramite deposizione in fase di vapore di elementi chimici organo-metallici e caratterizzati attraverso varie tecniche di microscopia elettronica a trasmissione.

Nella prima parte di questa tesi dimostriamo per la prima volta nanofili di GaAs senza difetti su un substrato CMOS compatibile. Il politipismo e l'alta densitá di difetti sono soppressi con successo grazie all'alto grado di libertá permesso da TASE. Infatti, TASE permette un ampio range di parametri di crescitá, pur mantenendo il controllo della morfologia e della direzione di crescita del nanofilo. Abbiamo poi analizzato la struttura atomica e la composizione di dislocazioni-scalino, un tipo particolare di difetto presente con certi parametri di crescitá. Una correlazione con le properietá elettroniche del difetto é ottenuta implementando simulazioni DFT. Questo suggerisce la possibilitá di ottenere canali mono-dimensionali di carica fortemente localizzati lungoquesti difetti, che potrebbero essere di importanza rilevante per future applicazioni elettroniche.

La seconda parte della tesi é dedicata all'investigazione degli effetti indotti da drogaggi p ed n su struttura e proprietá di nanofili $\mathrm{Ga_xIn_{(1-x)}P}$ e GaAs. Dimostriamo che TASE permette un buon controllo dell'incorporamento di drogaggio e che gli atomi di drogante modificano la struttura cristallina dei nanofili. Inoltre, mostriamo studi sperimentali di olografia fuori asse per la mappatura di campi di potenziale in nanofili drogati.

Consideriamo questi risultati come un tassello importante verso l'integrazione di nanofili III-V in dispositivi elettronici ed optoelettronici e anticipa che questo metodo di crescita innovative aprirá nuove strade nella realizzazione di architetture avanzate dei dispositivi.

Parole chiave: semiconduttori III-V, nanofili, drogaggio, micorscopio elettronico a trasmissione, transistor a effetto campo tunnel, celle solari, difetti cristallografici, spettroscopia di perdita di energia, spettroscopia EDX, olografia fuori asse.

Contents

Acknowledgments i

Abstract (English/Deutsch/Italiano) iii

List of publications xi

List of figures xiii

List of acronyms xvii

Chapter 1 Introduction & Motivation **1**

1.1 The two challenges of the modern era 2

1.1.1 No More Moore's Law? 2

1.1.2 Towards an energy crisis? 4

1.2 A unique solution with semiconductor nanowires 6

1.3 Crystal structure of III-V nanowires 7

1.4 Growth techniques 11

1.5 Solving the Si integration issue with TASE 13

Chapter 2 Techniques and methods **17**

2.1 A very brief historical introduction to microscopy 17

2.1.1 Basic principles in conventional TEM 18

2.1.2 STEM techniques 22

2.1.3 Off-axis electron holography 33

2.1.4 TEM instrumentation 38

2.2 Cathodoluminescence 39

2.3 Sample preparation 39

2.4 3D modeling and simulations 40

Chapter 3 Integration of planar GaAs nanowires on a CMOS compatible substrate...... 43

3.1 Nanowires growth 43

3.2 Defect-free GaAs nanowires and tuning of their front facets 45

3.3 Study of dislocation cores as mono-dimensional potential channels 55

Chapter 4 Doping investigation of vertical nanowires for PV applications 69

4.1 Nanowires growth 69

4.2 Dopant-induced modifications of $Ga_xIn_{(1-x)}P$ p-n junctions monolithically integrated on Si (111) 70

4.3 Investigation of electrostatic potential in doped GaAs nanowires by off-axis holography 82

Chapter 5 Conclusion & Outlook 99

Bibliography 103

Curriculum Vitae

List of publications

The results presented in this thesis have been published in peer-reviewed scientific journals or presented in scientific conferences. All the information is reproduced in this thesis with the permission of the corresponding publishers.
I performed the majority of the experimental investigations and data analysis and wrote most of the published manuscripts/proceedings.

•Article: M. Knödler, N. Bologna, H. Schmid, M. Borg, K. E. Moselund, S. Wirths, M. D. Rossell, H. Riel, "Observation of twin-free GaAs nanowire growth using template-assisted selective epitaxy", Crystal Growth and Design 17(12), 6297-6302 (2017)

•Article: N. Bologna, P. Agrawal, M. Campanini, M. Knödler, M. D. Rossell, R. Erni, D. Passerone, "Stair-rod dislocation cores acting as one-dimensional charge channels in GaAs nanowires", Physical Review Materials 2(1), 014603 (2018)

•Article: N. Bologna, S. Wirths, L. Francaviglia, M. Campanini, H. Schmid, V. Theofylaktopoulos, K. E. Moselund, A. Fontcuberta i Morral, R. Erni, H. Riel, M. D. Rossell, "Dopant-induced modifications of $Ga_xIn_{(1-x)}P$ nanowire-based p-n junctions monolithically integrated on Si (111)", ACS Applied Materials & Interfaces 10, 32588 (2018)

Moreover, I collaborated with several other projects by providing support in the analysis of materials and devices with TEM-related techniques. This led to the publication in peer-reviewed journals and conference proceedings.

•Article: G. Signorello, S. Sant, N. Bologna, M. Schraff, U. Drechsler, H. Schmid, S. Wirths, M. D. Rossell, A. Schenk, H. Riel, "Manipulating surface states of III-V nanowires with uniaxial stress", Nano Letters 17, 2816−2824 (2017)

•Article: C. Convertino, D. Cutaia, H. Schmid, N. Bologna, P. Paletti, A. M. Ionescu, H. Riel, K. E. Moselund, “Investigation of InAs/GaSb tunnel diodes on SOI”, IEEE International EUROSOI Workshop and International Conference on Ultimate Integration on Silicon, 148-151 (2017)

•Article: M. Borg, H. Schmid, J. Gooth, M. D. Rossell, D. Cutaia, M. Knödler, N. Bologna, K. E. Moselund, H. Riel, “High-Mobility GaSb Nanostructures Co-integrated with InAs on Si”, ACS Nano 11(3), 2554–2560 (2017)

•Article: J. Gooth, V. Schaller, S. Wirths, H. Schmid, M. Borg, N. Bologna, S. Karg, H. Riel, “Ballistic one-dimensional transport in InAs nanowire monolithically integrated on silicon”, Applied Physics Letters 110, 083105 (2017)

•Article: H. Schmid, D. Cutaia, J. Gooth, S. Wirths, N. Bologna, K. E. Moselund, H. Riel, “Monolithic integration of multiple III-V semiconductors on Si for MOSFETs and TFETs”, IEEE International Electron Devices Meeting (IEDM), 3.6.1−3.6.4 (2016)

•Article: D. Cutaia, H. Schmid, M. Borg, K. E. Moselund, N. Bologna, A. Olziersky, A. M. Ionescu, H. Riel, “Investigation of doping in InAs/GaSb hetero-junctions for tunnel-FETs”, IEEE Silicon Nanoelectronics Workshop (SNW), 152-153 (2016)

•Conference: The 16th European Microscopy Congress in Lyon (FR), Poster presentation, 28/08/2016-02/09/2016

•Conference: Empa PhD students symposium in Dübendorf (CH), Poster presentation, 14/11/2016

•Conference: Materials Research Day in Lausanne (CH), Poster presentation, 09/06/2017

•Conference: Microscopy Conference 2017 in Lausanne (CH), Oral presentation in ‘Quantification and Modeling Symposium’, 21-25/08/2017

•Conference: The 19th International Microscopy Congress in Sydney (AU), Oral presentation in ‘Physical Sciences – Semiconductors and materials for communication’, 09-14/09/18

List of figures

1.1 Moore’s law distribution 3

1.2 Energy consumption forecast 5

1.3 Zincblende-Wurtzite graphical scheme 8

1.4 Dislocation structure diagram 9

1.5 Graphical representation of the planar defects present in III-V NWs 10

1.6 TASE process graphical scheme 15

2.1 Electron-matter interactions 19

2.2 TEM setups 20

2.3 STEM diagram and detectors 24

2.4 Aberrations effects on the probe size 27

2.5 EDX physical principle 28

2.6 EELS diagram 30

2.7 Off-axis holography diagram 36

2.8 FIB lift-off procedure 40

2.9 3D model realized with Rhodius 42

3.1 Planar TASE procedure 44

3.2 Front facet morphologies in planar nanowires 46

3.3 Type I facet STEM structure analysis 47

3.4 Planar defects distribution 48

3.5 Type III facet STEM structure analysis 49

3.6 Facet occurrence with temperature 51

3.7 Facets temperature transitions 52

3.8 Facets growth rates 54

3.9 HAADF planar front section 56

3.10 Burgers circuits representation 57

3.11 Atomic EDX investigation 58

3.12 Experimental GPA on stair-rod dislocation 59

3.13 Simulated GPA on stair-rod dislocation 60

3.14 DFT bulk/defective system comparisons 61

3.15 PDOS distributions on bulk model 62

3.16 Wannier orbital representation of dislocation cores 63

3.17 Calculated DOS distribution along the stacking fault 64

3.18 Electron density and electrostatic potential maps 65

3.19 Isosurface potential charge simulation 66

4.1 $Ga_xIn_{(1-x)}P$ SEM overviews 71

4.2 HAADF-STEM structural analysis of undoped nanowire 72

4.3 EDX analysis on doped nanowire 74

4.4 HAADF-STEM structural analysis of doped nanowire 75

4.5 EDX analysis on undoped nanowire 77

4.6 EELS map and bulk plasmon peak profile 79

4.7 CL map 81

4.8 Off-axis holography on n-p GaAs nanowire 83

4.9 Magnified phase map of n-p GaAs nanowire 84

4.10 n-p comparison between experimental and simulated phase maps 86

4.11 SEM overview of TASE-SAG hybrid nanowires 87

4.12 Off-axis holography on first i-n-i GaAs nanowire 89

4.13 First i-n-i comparison between experimental and simulated phase maps 91

4.14 Off-axis holography on second i-n-i GaAs nanowire 93

4.15 Second i-n-i comparison between experimental and simulated phase maps 95

List of acronyms

NW	Nanowire
TEM	Transmission electron microscope
CL	Cathodoluminescence
SEM	Scanning electron microscope
DFT	Density-functional theory
GaAs	Gallium arsenide
CMOS	Complementary-metal-oxide-semiconductor
TFET	Tunnel field effect transistor
SS	Subthreshold slope
MOSFET	Metal-oxide-semiconductor FET
BTBT	Band-to-band-tunneling
OECD	Organization for economic co-operation and development
COP	Climate change conference
PV	Photovoltaic
ZB	Zincblende
WZ	Wurtzite

SF	Stacking fault
TW	Twin
APB	Anti-phase boundaries
VLS	Vapor-liquid-solid growth
SAG	Selective-area growth
MOCVD	Metal-organic chemical vapor deposition
TMGa	Trimethylgallium
Lch	Channel length
TASE	Template assisted selective epitaxy
HSQ	hydrogen silsesquioxane
GPA	Geometric phase analysis
VLM	Visible light microscope
STEM	Scanning TEM
EPW	Exit-plane wave
CCD	Charge-couple device
CTF	Contrast transfer function
XRD	X-ray diffraction
T(r)	Transmission function
ABF	Annular bright-field
HAADF	High-angle annular dark field
cFEG	Cold field emission gun
EDX	Energy-dispersive x-ray
VEELS	Valence electron energy-loss spectroscopy
SDD	Silicon drift detector
ZLP	Zero-loss peak
E_p	Plasmon energy

FWHM	Full-width at half maximum
ELNES	Energy-loss near edge structure
EXELFS	Extended energy loss fine structure
μ	Visibility of fringes
N_{el}	Number of electrons
φ	Phase resolution
I	Intensity
VB	Valnce band
CB	Conduction band
FIB	Focused ion beam
LDA	Local density approximation
GGA	Generalized gradient approximation
DZVP	Double-zeta valence polarized
PBA	Perdew-Burke-Ernzerhof
ELO	Epitaxial lateral growth
SOI	Silicon-on-insulator
TMAH	Tetramethylammonium hydroxide
TMGa	Trimethylgallium
TBA	Tertiary buthylarsine
HF	Hydrofluoric acid
SE	Secondary electron
PDOS	Localized projected density of states
LUMO	Lowest unoccupied molecular orbital
TMIn	Thrimethylindium
DEZn	Diethylzinc

1 Introduction & Motivation

This thesis focuses on the characterization of III-V semiconductor nanowires (NWs) grown by a novel epitaxy technique, Template Assisted Selective Epitaxy (TASE), by means of transmission electron microscopy (TEM). These nanostructured materials offer new possibilities toward solving two of the biggest problems affecting the present and the future of our global society: the apparent end of the Moore's Law within the information industry and the unsustainable increase in the fossil fuel consumption. Hence, in this research, we address the possibility to integrate defect-free III-V NWs on industry-compatible Si (100) substrates -without any metal catalyst- for photovoltaic and optoelectronic applications. Since the properties of these nanostructures are strongly related to the presence of electronic inhomogeneities, a particular focus is laid on the characterization of structural defects and compositional variations.

The present chapter mainly aims at introducing the two challenges of the modern era in the electronic and photovoltaic industry, highlighting the political, social, economic and scientific aspects. Then, it is explained why semiconductor nanowires are expected to play a critical role in future electronic and photovoltaic devices. Their beneficial properties, as well as the difficulties of integrating them on Si, are thoroughly described.

In the second chapter, the TEM techniques used in this project are described. The cathodoluminescence (CL) setup employed in the scanning electron microscope (SEM) is also discussed. Then, a description of the different steps performed to prepare the TEM lamellas for atomic-resolution imaging and compositional analysis is given. Finally, the last part is dedicated to the description of the 3D atomic modeling and density-functional theory (DFT) simulations used to simulate the influence of structural defects on the physical properties of the material.

Chapters 3 and 4 contain the core of the thesis and give a thorough overview of the results achieved during the entire doctoral project. Chapter 3 concerns the integration of defect-free gallium arsenide (GaAs) horizontal NWs on a complementary-metal-oxide-semiconductor (CMOS) compatible substrate. The obtention of high-quality crystals by tuning specific growth parameters represents an important step ahead in this field. A specific type of dislocation occurring in the GaAs crystal structure is also analyzed in depth and studied by means of DFT simulations.

Chapter 4 describes the first successful catalyst-free growth of indium gallium phosphide ($Ga_xIn_{(1-x)}P$) vertical NWs on a Si substrate for photovoltaic applications. Here, the effects induced by p-n dopants on the crystal structure, composition, and optical properties are assessed. The second part of chapter 4 presents off-axis holography experiments performed on GaAs NWs exhibiting different junctions, and a discussion of the limitations and artefacts of the method.

Finally, in chapter 5, the conclusions and a discussion of possible future developments which might take place in the field of III-V NWs on Si are given.

1.1 The two challenges of the modern era

Two technological challenges are threatening the modern era more than others: the saturation of the Moore's Law and the lack of efficient and sustainable energy solutions able to satisfy the rapid increase in the global energy demand. Even though hundreds of institutions and technology start-ups around the world have been making an important effort in trying to solve these two issues, the solution is still far distant.

1.1.1 No More Moore's Law?

A field effect transistor (FET) is the fundamental building block of all integrated circuits present in modern electronic devices [1]. This element is made of four components (i.e. source, gate, drain, and body) able to amplify or switch electronic signals and electrical power, by means of an applied electric field [2,3]. In this way, logic operations can be performed in virtually all the digital devices used nowadays. Integrated circuits have performances which can be directly related to the number of single transistors present on it. Every engineer working in the electronic industry in the early '60s was aware of the following apparently simple empirical relationship: the higher is the transistors' density, the higher will be the performance of the integrated circuit [4]. It was in 1965 when Dr. Gordon Moore, co-founder of Intel Corporation and considered as one of the fathers of the semiconductor era, described the increase in the number of transistors per chip with the so-called "Moore's Law". He predicted a doubling every year (which was in 1975 corrected at 18-24 months) [5]. On the other side, the cost per component was nearly inversely proportional to the number of components themselves [6]. This trend was perfectly matched for decades thanks to the continuous miniaturization process [7]. Thus, billions of silicon (Si) FETs were successfully integrated on commercial integrated circuits (Figure 1). This enabled a large increase in the number of logic operations while reducing the costs per single chip. For example, the Intel Xeon Broadwell chip, with one of the latest 14 nm technologies, implements around 7.2 billion transistors on a 456 mm^2 chip area.

However, the entire information industry is currently living one of the most challenging periods since the invention of the first computer. In fact, in the imminent future, some fundamental physical and technological limitations are expected to slow down or even arrest the pace of the above-mentioned trend [8–10]. The continuous reduction in the size of the transistor's gate can lead to the leakage of current through the very narrow dielectric layer even in the off-state [11–13]. On-chip interconnect scaling has also become a bottleneck to high-performance integrated circuits [14–16]. In fact, this process is physically limited by the electron scattering at the edges of the metallic wires, which becomes inevitable at the atomic scale [17]. Another crucial point is the saturation of the energy supply which cannot be sustained to be doubled every year [18]. All these factors are the main obstacles for the continuation of Moore's law. Indeed, it is Intel itself to predict the ultimate Si node size limit to 7 nm [19] while modern laptops mount a 14 nm.

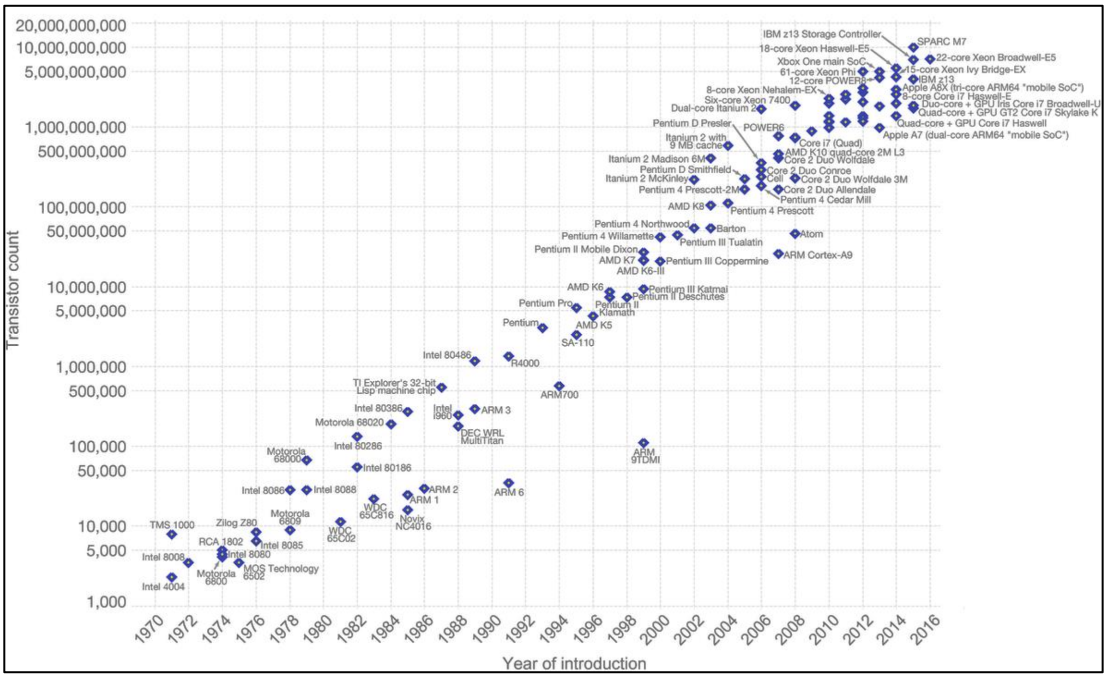

Figure 1.1 – Graphical representation of the Moore's Law. The number of transistors per chip is plotted with respect to the year of introduction of the specific commercial processor models. The linear trend and the saturation reached in the last years are both clearly visible [20] .

In order to solve these issues, new strategies addressing the use of novel materials for the channel and the dielectric, new device operation mechanisms and innovative device architectures are needed [21]. One of the possibilities is to use semiconductor materials combined with a tunnel FET (TFET) technology. This is expected to reduce the supply voltage needed to perform operations while maintaining a high I_{ON} and low I_{OFF} current [22,23]. This could lead to a reduction in the so-called subthreshold slope (SS), actually limited at 60 mV/decade for metal-oxide-semiconductor FETs (MOSFETs) technologies [24,25]. In fact, thermally injected carriers in MOSFETs have a SS limited by equation (1.1) where k_B is the Boltzmann constant, T is the temperature in Kelvin and q is the magnitude of the electrical charge [26].

$$SS = 2.3k_BTq \sim 60\ mV/dec \tag{1.1}$$

In TFETs, charge carriers tunnel from one energy band to another through quantum–mechanical Band-To-Band-Tunneling (BTBT) [27], rather than being thermally injected into the channel. In this respect, recent results show that this new approach could potentially reduce the supply voltage to 0.3 V [28], as compared to the present 0.5 V. However, beside the use of new physical principles to perform logic operations, a modification in the structures and materials used to build a transistor can greatly contribute to the continuation of the Moore's Law.

1.1.2 Towards an energy crisis?

Since the industrial revolution of the 18th century, the energy industry is experiencing one of the most challenging periods in human history due to the constant growth of the world population. In fact, the world inhabitants are growing at unprecedented rates and it is expected to reach around 10 billion in 2050 [29]. This phenomenon will certainly lead to a higher demand of energy, especially in the non-OECD (Organisation for Economic Co-operation and Development) countries, for industrial production and for the normal domestic economy (Figure 1.2). At the moment, the global energy consumption is around 150 PWh but it is expected to increase by more than 30% within the next decades and reach 200 PWh by 2050 [30]. Besides the inability to produce enough energy, environmental and climate concerns arise on the use of the present type of energy resources. Currently, more than 85% of the world energy production comes from oil, gas and coal resources [30]. However, the headlines of the most notable newspapers from around the world report every day about abnormal meteorological events caused, among others, by the extremely high CO_2 emissions. This phenomenon is leading to a mutation of the climate at an increasing pace. For example, the global average temperature has raised constantly in the last decades and the polar ice caps are melting at an unprecedented rate [31–33]. This is expected to cause a rise of the water level of the oceans within a few years [34]. All these interconnected phenomena represent a serious threat for the Earth's geological, biological and ecological systems. For this reason, increasing the amount of produced energy in order to satisfy the global demand is not a feasible solution if the CO_2 emissions related to the present technology generation are not strongly decreased.

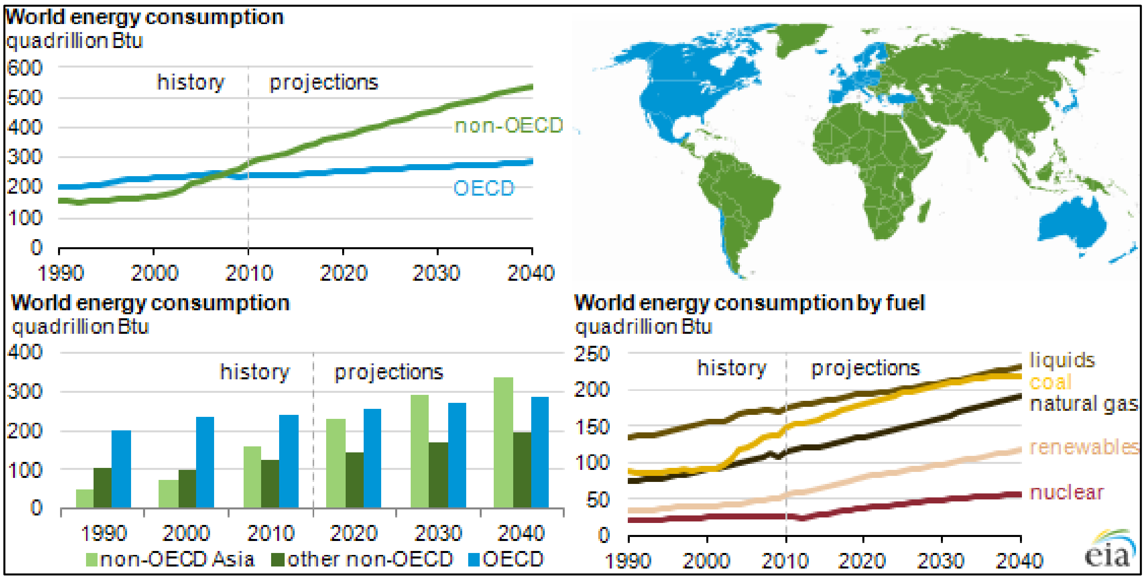

Figure 1.2 – Energy consumption predictions for OECD and non-OECD members. The distribution of the different energy resources is also plotted as a function of time. The image is adapted from [35].

It was in December 2015, at the United Nations Climate Change Conference (COP 21) in Paris, when a first tangible tentative to act against this crisis was planned. With the so-called “Paris Agreement”, 174 countries agreed to pursue efforts to limit the increase in the global temperature by 1.5°C. This will require zero emissions sometime between 2030 and 2050 and a radical modification of the energy production industry. For this reason, more than 1 trillion dollars were invested globally since 2015 in the research and development of renewable energies [36] such as wind, biofuel and solar photovoltaics (PV). In particular, the latter is considered to be the most promising technology to overcome the energy and pollution issues and to generate a virtually infinite amount of clean energy. Solar cells are, indeed, able to convert the solar radiation captured on their surface in working current [37]. By considering the annual solar radiation hitting the surface of the earth, an infinitesimal portion could supply enough energy to meet the entire global demand. This is one of the reasons why more than half of the investments in renewable energies were assigned to solar energy technologies.

However, the current Si solar cells mounted on the roofs of private and industrial buildings have rather low efficiencies as compared to the theoretical maximum efficiency that a perfect device could reach, and the reasons are multiple. First of all, Si p-n junction solar cells are intrinsically limited by the Schockley-Queisser limit which gives a maximum level of efficiency of 30% by absorbing a wavelength of 1.12 µm from the solar spectrum [38–40]. Second of all, there are many recombination mechanisms limiting the conversion efficiency. Many of them, unfortunately the most effective ones, are given by the material quality at the atomic level, the device design and the fabrication process [41,42]. Different strategies have been studied and developed with concept devices in all the major institutions and laboratories achieving very high efficiencies up to 45% [43]. However, costs are still one of the most important limiting factors preventing the photovoltaic technology to overcome the fossil fuel energy generation.

1.2 A unique solution with semiconductor nanowires

In the last decade, III-V semiconductor nanowires (NWs) have been regarded as the definitive solution for both the electronic and the photovoltaic industry. The III-V prefix is related to the type of atomic species they are composed of. In fact, they are made of combinations of elements from the group IIIA (13) and VA (15) of the periodic table. Typical binary compounds are GaAs, GaSb, InP, etc. Ternary compounds are also possible such as InGaAs and GaAsSb. Compared to group IVA elements (Si, Ge), III-V materials exhibit very unique properties. For example, in specific combinations of group III and V, they show a direct bandgap which is crucial for optoelectronic applications [44]. As opposed to Si, a direct bandgap allows the conservation of the momentum during recombination processes without the use of phonons, leading to higher radiative recombination coefficients. The possibility to engineer their bandgap is also a fundamental aspect of III-V materials, especially in ternary compounds. The combination of these properties with a high surface-to-volume ratio, high miniaturization and strain relaxation of the nanowires makes them very appealing for a huge variety of applications. In fact, a lot of effort was given to apply these nanostructured materials to the two above-mentioned industries, namely in TFET and PV devices.

TFETs devices have been built from III-V NWs by several research groups. TFETs with InAs NW/p-Si and InAs-InAlAs/p-Si heterojunctions were proposed by Tomioka et al. in 2011 [45]. They demonstrated one of the first working devices made of III-V NWs. However, the quality of the nanostructures was far from excellent and several crystallographic defects, especially misfit dislocations at the different interfaces, were present. The performance of the fabricated devices was certainly degraded by the inhomogeneities present in it resulting in a subthreshold slope under reversed bias conditions of 104 mV/dec. In the same year, n-i-p InAs-Si-Si gate-all-around NW TFETs were fabricated at IBM-Research in Zürich by Schmid et al [46]. As in the previous cases, growth defects and unperfect device contacts limited the drive current to ~ 0.4µA/µm and the SS to 220 mV/dec. The potential of III-V heterostructures in TFETs was demonstrated for the first time by Dey et al. and Ganjipour et al. of the Department of Information Technology and the Department of Solid State Physics at the Lund University in Sweden [47,48]. A record high I_{ON} current of 110 µA/µm and a minimum SS equal to 50 mV/dec represented important results for the research community, proving the real potential of this combination between new engineering technology and novel materials as a new building block for future low-power electronics. However, the strong temperature dependence of SS and I_{ON} current suggested a trap-assisted tunneling and a thermal emission from the traps. Once again, the low quality of the grown structures had a significant influence on the overall device performance. Zhao et al. in 2014 performed other experiments on ternary heterostructures made of InAs/InGaAs, confirming the high potential of such a structure in electronic devices [49]. In fact, he was able to reach an average value of SS equal to 79 mV/dec at V_{ds}=0.3 V and a I_{ON} current of 0.27 µA/µm in the best performing device. Then, in 2016 a triple structure device made of vertical InAs/GaAsSb/GaAs heterostructures NWs was demonstrated by Memisevic et al., again at the Department of Solid State Physics at the Lund University [50]. Here, a minimum SS of 48 mV/dec was obtained, confirming the promising nature of III-V NWs for TFETs devices. With these reported examples, it becomes clear that the growth of high-quality NWs is crucial for the realization of efficient TFETs devices and more research focusing on the optimization of NWs growth on a CMOS compatible substrate is needed.

III-V nanostructures could represent a further step ahead also for the photovoltaic technologies. In fact, recent years have seen the realization of multi-junction solar cells made of III-V semiconductor thin films [51]. The efficiency of these devices reached 45% by absorbing different wavelengths of the solar spectrum under concentrated sunlight illumination [43]. This value is about twice the highest value achieved with crystalline Si solar cells [52]. Being NWs a high aspect ratio crystalline structure, when implemented on a Si platform they would allow to significantly reduce III-V material usage and the associated costs. At the same time, they can ensure an extremely high absorption of light thanks to the optimal light coupling [53,54]. Additionally, the small interface area of the NWs is very effective at minimizing stresses commonly arising during the epitaxial growth of lattice and thermal mismatched thin films [55,56]. Thus, the efficient strain relaxation in thin nanowires allows extending the possible material combinations needed to grow NW heterostructures. $Ga_xIn_{(1-x)}P$ NWs are currently attracting great interest as a promising nanostructured material system for efficient photovoltaic solar cells [57,58]. Due to their direct and tunable bandgap over a wide range of compositions (1.35-2.26 eV), $Ga_xIn_{(1-x)}P$ NWs, integrated on a Si substrate (1.12 eV), can be designed to absorb light from the major part of the visible solar spectrum [59–61]. Thus, by intentionally varying the composition, the dopant type and concentration along the NWs, different parts of the spectrum can be absorbed and loss of energy through carrier thermalization minimized. These properties have important economic implications to meet the demand for both high efficiency and low-cost solar cells. However, as in the case of TFETs devices, two critical aspects connected to the growth of the materials still need to be optimized in order to obtain high-efficient NWs solar cells: i) the demonstration of composition controlled high-quality $Ga_xIn_{(1-x)}P$ nanowires on Si substrates and ii) the effect of doping on the NW composition, microstructure, and morphology.

Since a critical step towards the optimization of TFET and PV devices is the investigation of the defect formation mechanisms, a complete description of the structural defects that occur in semiconductor heterostructures is given in detail in the next section. It treats, in particular, crystallographic defects caused by discontinuities in the stacking sequence of the atomic layers as well as defects arising when growing III-V NWs on different substrates.

1.3 Crystal structure of III-V nanowires

III-V NWs are elongated crystals with diameters typically below 100 nm and lengths up to several micrometers. This quasi mono-dimensional structure allows, unlike in thin films, to relax the possible stresses arising at the interface between different materials [62]. They can either exhibit zincblende (ZB) or wurtzite (WZ) crystal structure depending on the stacking sequence of the atomic bilayers in a cubic or hexagonal crystal packing as shown in Figure 1.3, respectively [63]. ZB can be described as two interpenetrating systems of close-packed cubic structures located at (0,0,0) and (1/4, 1/4, 1/4), respectively. The stacking sequence of the atomic bilayers in the ZB structure is ABCABC... in the <111> direction. WZ is the equivalent hexagonal structure with a stacking sequence of atomic bilayers of the type ABABAB... in the $[000\bar{1}]$ direction.

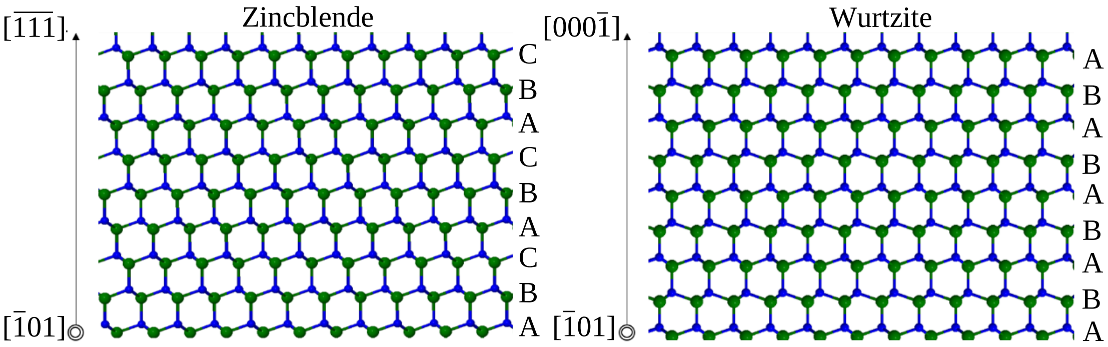

Figure 1.3 – Schematic representation along the $[\bar{1}01]$ zone axis of the Zincblende and the Wurtzite stacking sequence of atomic planes. The green spheres correspond to the IIIA atoms while the blue ones to the VA atoms.

III-V NWs are mainly affected by two types of discontinuities: mono-dimensional and bi-dimensional defects. The first type, also called dislocations, corresponds to the front of propagation of a line defect due to the sliding of atomic planes over each other. A dislocation is characterized by two parameters: the direction of the propagation of the dislocation in the crystal, namely dislocation line, and its Burgers vector. The Burgers vector defines the magnitude and direction of the slip. It can be identified by making a closed circuit around the hypothetical dislocation by jumping from one lattice point to the neighboring one until the starting point is reached again. If the circuit fails to close, then a dislocation is surrounded, and the lattice vector needed to complete the circuit is the Burgers vector of the dislocation. Two main types of dislocations can be distinguished: edge and screw dislocation. The first one has the Burgers vector perpendicular to the dislocation line while in the second case it is parallel.

Besides, mixed dislocations where the line direction and Burgers vector are neither perpendicular nor parallel can also be found; they have both screw and edge character. In the case of nanowires, misfit edge dislocations are commonly observed [64], and they form, as the name suggests, due to the misfit at the interface between two crystals. This can occur either at the substrate-nanowire interface or between two different semiconductors in nanowire heterostructures. Then, an extra half-plane of atoms is present in the crystal causing the region around it to be in compression and the region at the other side of the dislocation to be in tension. Both dislocations are represented in Figure 1.4.

The presence of dislocations in semiconductor crystals used for electronic devices can result in a complete failure of performance [65–67]. The benefit in using a nanowire geometry is that, as opposed to thin films, the range of critical dimensions below which we can have defect-free nanowires is higher, allowing a more efficient growth. These critical dimensions are the nanowire diameter and axial distance, along the nanowire growth direction, after the interface with the Si seed [55]. Another type of dislocations which often occur when growing III-V NWs are the so-called stair-rod dislocations and, given the importance in this project, they will be discussed ahead in a dedicated chapter.

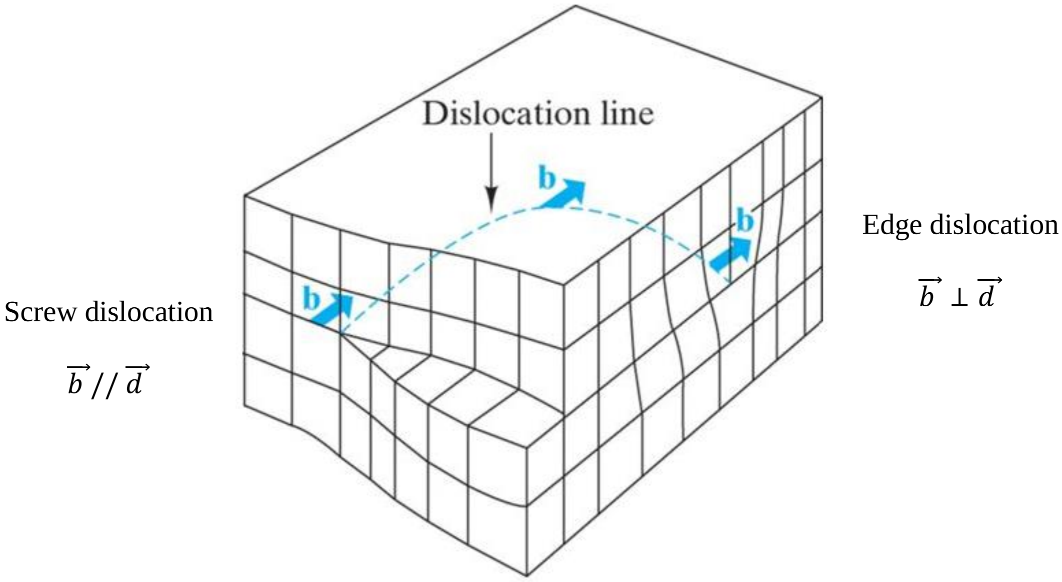

Figure 1.4 – Schematic diagram showing a screw and an edge dislocation with the Burgers vectors and the dislocation line indicated by the blue arrows and the dashed line, respectively. Adapted from [68]

When considering planar defects, we can distinguish stacking faults (SFs), rotational and mirror twins (TWs) and antiphase boundaries (APBs). They are all related to the stacking of the atomic bilayers and can be associated to dislocations, caused by a high thermal expansion coefficient mismatch or by the high susceptibility of the (111)B surface to twinning [69,70]. A SF is the local interruption in the regular stacking sequence which continues in the same manner after it; SFs can be either intrinsic (a single missing layer) or extrinsic (a single additional layer). A rotational TW, also denoted as ortho-twin, can be illustrated by considering a segment with a ZB crystal structure and then rotating it 60° around the <111> axis. The bond over the twin is heteroatomic and the polarity of the crystal is maintained. A mirror twin, also called para-twin, occurs due to a 180° rotation in the twin plane. In this case, the bond over the twin is homoatomic (III-III or V-V) and the polarity is therefore reversed. An APB is a special case of planar defect in which two non-equivalent polar orientations of the III-V structure associated with the interchange of the group III and V sublattices are in contact. This can occur due to intrinsic single steps of a/4 <001> high on the Si surface or simply due to mixed nucleation on Si. Hence, between domains in anti-phase relation, the crystal polarity and bonding directionality are reversed. The presence of all these defects in III-V nanowires can highly affect the efficiency of the final device. In fact, they act as preferred sites for impurities, high diffusivity paths for dopants and non-radiative recombination centers [66,71] resulting, for example, in an increased leaking current in TFET devices [72]. Additionally, the band gap energy might also be modified since twinning can induce the alternation of ZB and WZ sections [63,73,74], not allowing a good control of the optical properties for PV applications. The described planar defects are shown in Figure 1.5.

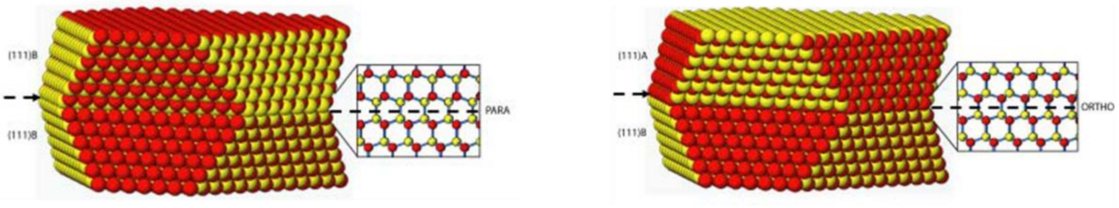
Mirror (para-) twin

Rotational (ortho-) twin

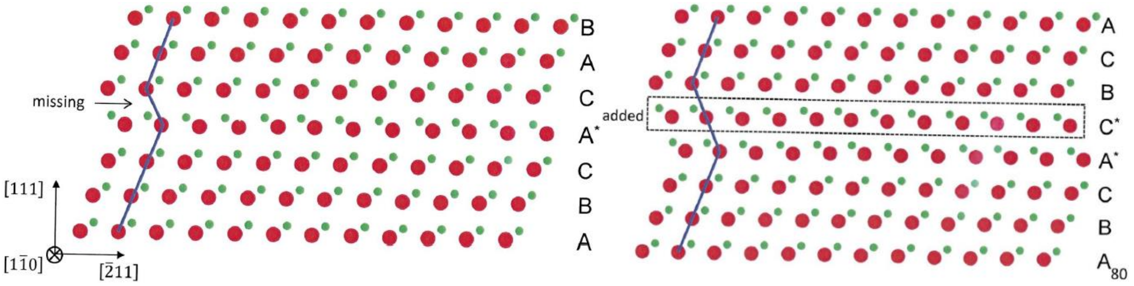
Intrinsic stacking faults

Extrinsic stacking faults

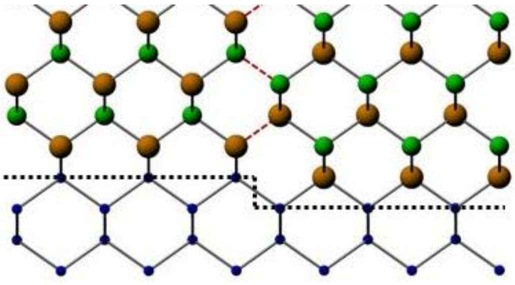
Anti-phase boundary

Figure 1.5 – Graphical representations of the planar defects that can be encountered in semiconductor NWs. Reproduced after [75,76]

Two main methods have been developed to grow III-V NWs and, in the following section, I will explain the benefits but especially the limitations associated to each technique.

1.4 Growth techniques

Performing high-quality growth of III-V NWs on different substrates is pivotal in order to obtain high-performance devices. Indeed, the NW quality depends strongly on the growth technique and process conditions. Here, we introduce the two main techniques used so far, i.e. vapor-liquid-solid growth (VLS - the most common) and selective-area growth (SAG).

VLS This technique is the most widely used because of its simplicity and versatility. In this method, the metal catalyst, usually a gold particle, forms liquid alloy droplets at a high temperature by adsorbing vapor components from the precursors. Given their continuous supply, the components coming from the precursors will reach a concentration higher than the equilibrium one, reaching the so-called supersaturation. At this stage, in order to return to the minimum free energy of the system, the molecules of the vapor precursor will start to precipitate forming the solid part. This happens directly at the interface with the liquid particle. This leads to the growth of the mono-dimensional structure which continues as long as the gas precursors are kept active. Since this process takes into account the three different states of the matter (the vapor precursor, the liquid metal particle and the solid precipitate), it is called VLS growth [77]. The diameter and position of the 1D structures are related to the size and position of the catalyst, as the liquid phase is confined to the area of the precipitated solid phase. However, the VLS technique has some important drawbacks: (i) the growth direction is strictly related to the substrate orientation [78,79], (ii) there is no precise control on nanowire location, and (iii) the gold is not compatible with the industrial standards [80]. Furthermore, the alloy particle can act as a trapping site for carriers, affecting the device performance [81,82].

The amount of publications reporting on the growth of III-V nanowires obtained with this method is very large. The very high flexibility in growing axial heterostructures, for example, is one of the key benefits in using the VLS method. In fact, modifying the nature of the precursor during the growth allows to obtain heterointerfaces in the range of few nanometers but with a high density of dislocations [83–88]. Similarly, radial heterostructures can be grown as well. However, the temperature must be increased such that the axial growth is suppressed and the precipitation of the solid component occurs on the lateral sides of the NW [89]. The direction of the growth corresponds to the one that minimizes the total free energy of the system, which is generally given by the free energy at the S-L interface between the NW and the metal particle. For example, cubic lattices like InP and GaAs, present for most of the growth conditions the formation of a single (111) plane at the S-L interface, which leads to a growth in the <111> direction [90]. Depending on the stacking sequence of the atomic planes, there can be a <111> A or B growth direction, i.e. Group-III or group-V terminated. The latter is the most common one since leads to a higher reduction in the free energy [91]. However, the growth in the <111>B direction often leads to a very high density of planar defects which are able to affect most of the optical and electrical properties of devices integrating NWs. Since the optical, electrical and mechanical properties of the nanowires are strongly dependent on their growth direction, much research has been conducted to control their orientation. In fact, a lot of interest is dedicated to the growth in other more uncommon directions which could lead to defect-free nanostructures [92]. One efficient and simple way to do this resides in modifying the growth conditions of the NW itself, at the initial stage of the process, as a sort of in-situ method. The main parameters to be tuned during the growth process are generally the partial pressure of the precursors, their molar ratios (the so-called V/III ratio) and the growth temperature. Several examples on how these parameters are able to affect the growth orientation have been reported in literature [93].

Concerning the device integration, the possibility to grow co-planar III-V nanowires directly on the substrate is highly desirable. Using metal organic chemical vapor deposition (MOCVD), the temperature variation has been one of the metrics mostly used to modify growth orientation of GaAs NWs on GaAs substrates. In fact, when grown on the (100)-oriented substrate at low temperatures (~ 420 °C), the common growth direction is the <111>B. On the other hand, if the temperature is raised above 450 °C, the preferred reported growth direction is the <110>, i.e. the two directions along the plane of the substrate [94]. Similar growth orientations were recently demonstrated with GaAs NWs grown on a (001) GaAs substrate by using the atmospheric pressure MOCVD [95]. Similar planar NWs were also observed by Zhang et al. when growing InAs NWs on a (111)B-oriented GaAs substrate. In this case, the Au catalyst plays a key role since it maintains the {111} interface with the InAs NW and the (111)B interface with the GaAs of the substrate. In this way, the NW is forced to grow in one of the <112> six equivalent directions of the substrate surface [96].

Concerning the V/III ratio of the precursors flow rates, it has been already demonstrated how they can significantly affect the growth rate and overall morphology of the NWs [97–99]. High V/III ratios induced kinking and non-<111>B growth directions when using AsH3 and Trimethylgallium (TMGa). The possible reason was proposed by Joyce et al. [100]. In fact, he suggested that stable As trimers forming on the (111)B surface might modify the surface free energy, allowing other growth directions. Moreover, the high V/III ratio could also modify the eutectic alloy composition of the metal catalyst particle and, as a consequence, the growth direction [100]. Several groups achieved also a good level of control of the polytypism in III-V NWs. The possibility to tune the presence of planar defects along the nanowire in order to obtain ZB or WZ sections has been demonstrated and used for bandgap engineering [63,101,102]. Both vertical and horizontal TFETs obtained with III-V VLS-nanowires were demonstrated showing high Ion current and low SS [72,103]. However, industrial compatibility and perfect crystal quality are still the major challenges of the VLS method.

SAG This technique uses a different approach in which top-down and bottom-up methods are combined. In Selective-Area Growth, a patterned oxide mask is deposited on the III-V substrate and the nanowires are allowed to grow only where the apertures are located [80]. The important benefits of this method are the absence of a metal catalyst and the precise location of the nanowires.

The first GaAs and InGaAs nanowires were grown directly on (111) III-V substrates having very small diameters (50 nm) and high aspect ratios closely related to the mask opening size. No tapering and atomically flat lateral surfaces were observed. Any inhomogeneity of the oxide mask can, however, be transferred to the nanowires giving rise to the formation of defects [104]. The control of the growth conditions can lead to the realization of axial and radial heterostructures [105] but with the formation of non-intentional core-shell features at the heterointerface [106]. Some problems arise when SAG is applied to non-polar substrates like Si since growth occurs in four equivalent <111> directions. This results in the formation of NWs tilted with respect to the (111) surface, which is not advantageous for attaining high-density integration of NW-based devices on Si [107,108]. This problem was overcome by surface pretreatment obtaining a Si (111)B top surface allowing the vertical integration of III-V nanowires [109]. The obtained nanowires contain, as expected, a high density of planar defects and dislocations at the substrate-nanowire interface. Polytypism was also observed [110].

Concerning device integration, III-V heterojunction interface is used for steep-SS switches thanks to the pseudo-staggered type-II band discontinuity. When the voltage is applied and the TFET is turned on, band-to-band tunneling occurs. A SS=12mV/decade for InGaAs nanowire on Si (111) at room temperature was reported [111]. Anyway, the coexistence of steep SS and large SS was observed where the latter was due to trap-assisted tunneling through the defect level originated from misfit dislocations. A relationship with the channel length (Lch) was also verified, showing a steepness in SS with decreasing L_{ch} [112]. A relationship between nanowire diameter and the presence of misfit dislocations was observed also for this technique. In fact, for different Si/III-V heterojunctions (InAs, InGaAs and GaAs) a critical diameter (~ 18nm) below which no misfit dislocations occur was reported. In this way tunneling via dislocations level is suppressed and BTBT dominates [113]. Finally, even if high-performance TFET were demonstrated with a very small SS [114], [111], (i) a very small growth rate and (ii) a high substrate dependence remain key challenges for their implementation in the semiconductor industry since no nanowires grown on top of Si (100) have been successfully reported.

All the drawbacks reported for VLS and SAG techniques could be overcome by the use of a novel epitaxy technique developed in the recent years at IBM-Zurich called Template Assisted Selective Epitaxy (TASE).

1.5 Solving the Si integration issue with TASE

This newly developed technique is very similar to SAG in avoiding any form of catalyst particles which could affect the sharpness of the interfaces and contaminate the nanowire. Basically, the nanostructures are grown in nanotube templates by MOCVD on Si wafers at temperatures ranging from 450°C to 650°C. A typical procedure to fabricate the vertical templates is the following and is illustrated in Figure 1.6. A sacrificial amorphous α-Si layer is sputtered on the wafer's surface. The thickness of the α-Si layer determines the height of the templates, while the diameter (30-500 nm) and position of the templates are defined by patterning hydrogen silsesquioxane (HSQ) dots by electron beam lithography. Inductively-coupled plasma reactive-ion etching using HBr/O_2 is employed to etch out vertical Si nanowires. SiO_2 is then subsequently deposited on the Si nanowires by plasma enhanced chemical vapor deposition at 400 °C. In order to empty the nanotube templates and to obtain a pristine (111)-terminated crystalline Si surface at the bottom, a patterned resist mask is deposited to protect the substrate and a 25% tetramethylammonium hydroxide solution is used to selectively etch away the Si sacrificial nanowires. The III-V semiconductor NW is then grown inside the remaining cavity by MOCVD.

The TASE technique offers highly valuable advantages compared to VLS and SAG since no metal particle is used as catalyst, there is no dependence on the substrate orientation [115] and the growth parameters can be modified still maintaining the same nanowire shape and direction [116]. Furthermore, with this method any substrate-dependency on the NW morphology is avoided since the nanotube template defines the shape of the targeted NW, preventing also the formation of non-intentional core-shell structures at the interface in axial-heterostructures [117].

At the first stage, InAs on Si (111) and InAs/InSb heterostructures were studied [117]. In both cases, a relationship between the nanotube filling and the V/III ratio was observed. Thus, for a low V/III ratio, partial filling of the template is achieved, while with higher ratios, complete filling of the structures is obtained [116]. These results show that the TASE method allows using a larger window of growth parameters compared to a template-free NW growth. This allowed to completely avoid the formation of non-intentional core-shell structures as in the case of normal SAG. The InSb sidewalls reflect the hexagonal facets of the six equivalent <110> directions given by the InAs NW structure. TEM analysis showed a close contact between the template and the deposited InSb with no voids. The chemical transition between the two semiconductors occurs over a distance of ~2 nm, so much smaller than in the case of the VLS technique where the transition for the same heterostructure was observed to be ~20 nm [118]. The use of the Geometric Phase Analysis (GPA) allowed measuring and mapping the displacement and strain fields at the hetero-interfaces. The formation of periodic misfit dislocations at an average distance of 7 nm along the radial direction was observed to release the 7% lattice mismatch between InAs and InSb [117], allowing the strain relaxation to happen within 4 nm along the axial direction. It is important to differentiate the growth direction of the nanowire inside the template and the final orientation of the structure, which is only imposed by the template. To confirm this behavior, InAs nanowires were grown on several differently oriented Si substrates, i.e. (100), (110), (112) and polycrystalline Si substrate [115]. This demonstrated that the shape, dimension and final orientation of the nanostructure are only given by the SiO_2 nanotube template down to a diameter of 25 nm. Yet, the final facet of the nanowires shows different orientations for the same Si substrate and does not seem to be consistent. The possibility to control the final facet orientation would represent an additional benefit of this method. By atomic-resolution imaging, planar defects were observed in the InAs nanowires [115]. Furthermore, the nanotube diameter was found to be affecting the nanowire length since a small diameter (few tens of nm) reduces the length of the nanowire on a Si (110) substrate. On the contrary, the NW length was increasing on the Si (111) substrates because of a different effective V/III ratio inside the tube [116].

A key benefit of this technique is the simple realization of nano-devices. The first p-i-n TFET, with planar InAs nanowires integrated on Si(100), was demonstrated by Schmid et al. in 2015 showing that their performances match the ones of devices based on conventional nanowire growth process with a SS = 160 mV/dec [119]. Co-planar InGaAs and InAs nanowires directly integrated on Si (100) were also fabricated [120]. TEM cross-sectional analysis confirmed a very good control over position, dimension and surface roughness also for these lateral samples. The possibility to grow vertically stacked 3D structures, nanostructures containing a pre-defined constriction and nano-scale cross-junctions were all achieved showing the high versatility of the TASE method [120].

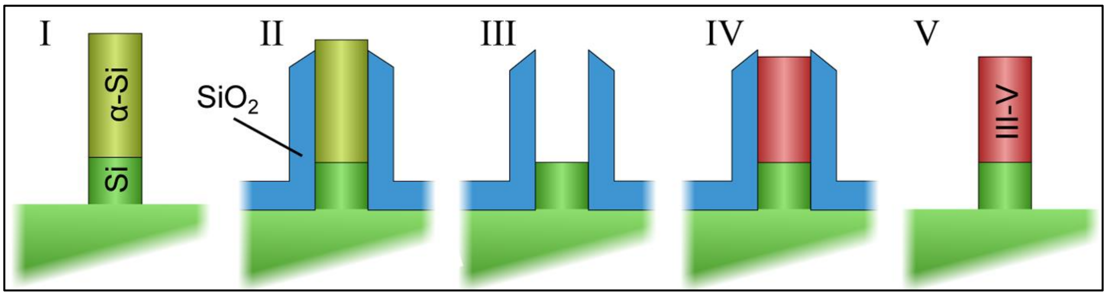

Figure 1.6 – Graphical scheme showing the different steps in the realization of a vertical III-V NW using the TASE technique. The first step is the deposition and the subsequent creation of a Si sacrificial NW by e-beam lithographic process. The SiO_2 layer is deposited on the surface by PECVD. The top facet of the NW is exposed by dry-etching the SiO_2 layer while the rest of it is protected by a photoresist. The sacrificial NW is then etched away, leaving an empty cavity. Finally, the III-V NW can be grown inside, and the template is removed by dry-etching. Image adapted from [115].

Nevertheless, although TASE decidedly offers important advantages, III-V NWs grown with this method often present numerous crystallographic defects. Moreover, the effect of dopant incorporation in TASE grown NWs is a highly significant, yet unexplored, issue. The present research project addresses these topics thoroughly and brings out several key results for the future integration of NWs in electronic and photovoltaic devices. This is achieved by means of several electron microscopy techniques. In particular, TEM provides the spatial resolution to study the structure and properties of materials at the atomic level. Accordingly, the next chapter is mainly devoted to the description of the TEM techniques that were used for this work.

2 Techniques and methods

This chapter contains a thorough description of the different techniques and methods used in this research project. Therefore, the main part of this chapter is devoted to the description of the TEM techniques utilized to characterize the III-V NWs. Besides, the CL setup is also introduced. The physics related to each method is explained in detail. Moreover, a dedicated section explaining the necessary steps to obtain optimal TEM specimens for atomic-resolution imaging and spectroscopy is included. Finally, the approaches and software used to create the 3D atomic models and to perform the DFT simulations to study the electronic properties of the investigated nanostructures are presented. Note that as the growth conditions of the studied NWs are very specific to each system, they are not given here but in their respective chapters 3 and 4.

2.1 A very brief historical introduction to microscopy

Mankind has always been interested in observing very small objects which are not visible to the naked eye. The early microscopes were optical (or light) microscopes and were developed in the late 16th century. They were compound microscopes, which used two lenses: the objective lens positioned close to the object (used to focus a real image of the object inside the microscope) and a magnifying lens, or eye piece (used to form an enlarged inverted virtual image of the object). These instruments were able to magnify microscopic objects, allowing scientists to reveal very small details of the objects surrounding them, like the body components of a bee for example [121]. One of the first scientific applications was proposed by Antonie van Leeuwenhoek (1700) who was able to image biological organisms like bacteria and protists for the first time [122]. Since then, microscopy has evolved exceptionally, in particular, thanks to the technological and scientific breakthrough in electron optics in the early 20th century. This revolution, initiated by Louis de Broglie (1924) and Hans Busch (1926), led to the development of electron sources and electron lenses crucial for the realization of the first TEM by Max Knoll and Ernst Ruska in 1931 [123]. However, this microscope was far from approaching the theoretical resolution of 2 Å. The factors hampering the resolution limit of the early TEMS were, among others, the brightness of the electron sources, the (mechanical) stability of the systems, and the inherent aberrations of the electrostatic electron lenses. Several decades of research and engineering have been necessary to overcome these issues and build electron microscopes able to deliver a spatial resolution of even less than 50 pm [124]. Nowadays, a large amount of information can be obtained with a TEM: imaging of structural defects [125], strain mapping [126], elemental composition [127], doping evaluation [128], optical [129] and electrical properties [130], etc. On the other hand, the realization of samples for TEM analysis can be tedious and often take several hours [131]. Additionally, as discussed towards the end of the chapter, special care needs to be taken in order to prevent undesirable structural and compositional sample preparation artifacts [132]. Finally, TEM has been applied in basically all fields of research, from molecular biology to materials science and medicine. Given the many imaging and analytical capabilities - at a unique spatial resolution - of modern TEMs s, TEM was selected in this thesis as the primary tool to characterize III-V NWs.

In the following sections, I describe the basic working principles of the TEM and the physics behind the different techniques used in this research.

2.1.1 Basic principles in conventional TEM

The working principle of the TEM is to some extent similar to what happens in conventional visible-light microscopes (VLM). In fact, both tools use lenses to direct a wave in a specific direction and to magnify a very small object. However, some important differences are present. In optical microscopes, an objective lens is used to create a magnified image of the specimen which is magnified further by the use of an eyepiece. This creates an enlarged inverted virtual image of the specimen, revealing details which were not visible by naked eye. At the bottom of the microscope, another series of lenses is able to guide the illumination coming from the source directly to the sample. In TEMs, light is replaced by electrons. The electron beam is generated from an electron source, generally located at the top of the microscope. Several condenser lenses shape the electron beam while the condenser apertures, which are placed below the condenser lenses, are used to define a specific illuminated area and to set the convergence angle. Then, a series of apertures and electromagnetic lenses form, depending on the operation mode, a near-parallel (TEM mode and diffraction) or a focused beam (scanning TEM mode). The beam then interacts with an electron transparent sample, typically thinner than about 100 nm. Multiple electron-specimen interactions might take place resulting in different emitted signals, as shown in Figure 2.1 [131]. These signals can be efficiently used for creating images, diffraction patterns, and spectroscopic analyses. Thus, TEM techniques can deliver information on the sample’s microstructure, chemical composition, and electronic and magnetic properties.

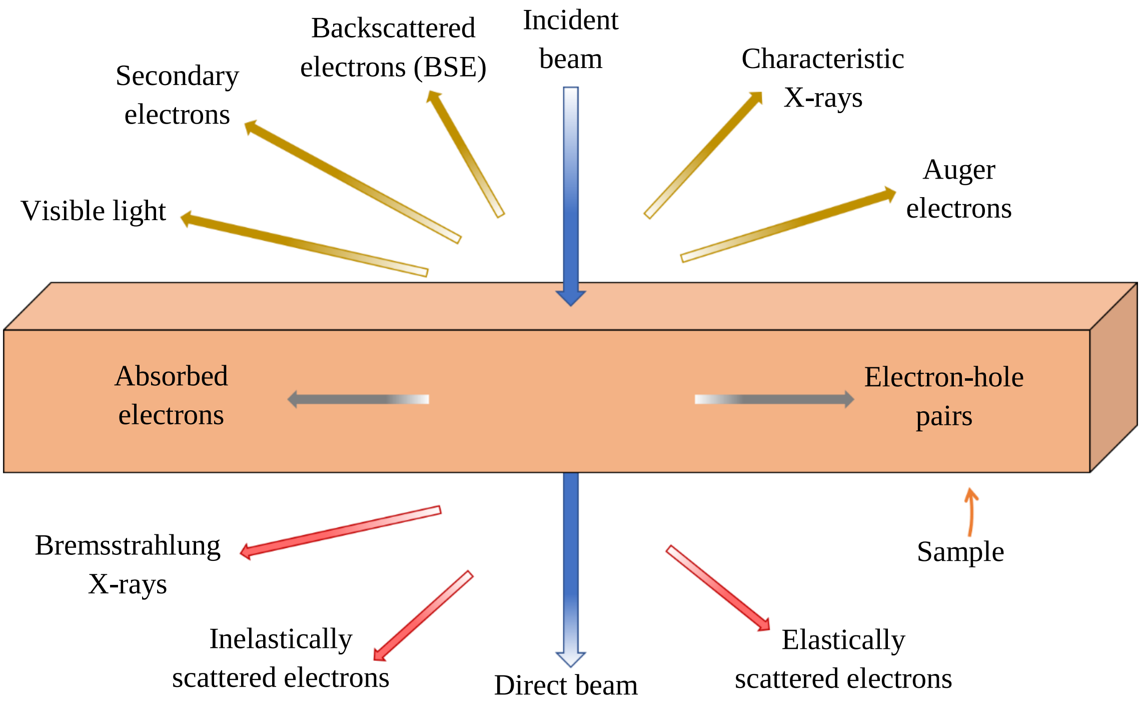
Backscattered electrons (BSE)
Incident beam
Secondary electrons
Characteristic X-rays
Visible light
Auger electrons
Absorbed electrons
Electron-hole pairs
Bremsstrahlung X-rays
Sample
Inelastically scattered electrons
Direct beam
Elastically scattered electrons

Figure 2.1 – Graphical representation of the different types of emitted signals occurring when a high-energy electron beam interacts with a thin specimen. Reproduced from [131].

When an electron impinges the specimen, it interacts with the Coulomb potential of the atomic columns which causes its diffraction and a change of its propagation velocity. Consequently, the sample induces a modification of the amplitude and phase of the incident electron wave which leaves the specimen with modified characteristics, resulting in the so-called exit plane wave (EPW). The EPW then is projected onto the fluorescent screen or recorded by a charge-coupled device (CCD) camera, through another series of apertures and lenses. Depending on the used technique and the properties of the material, the final image reveals a contrast arising from different phase and amplitude mechanisms. When working in high-resolution TEM mode, the phase contrast is the main image contrast mechanism containing structural information of the sample. This contrast is the result of a modification process by which the phase modulation of the EPW is transferred to amplitude contrast. This is possible by convoluting the EPW with the so-called contrast transfer function (CTF) which is specific for each microscope and is given by equation 2.1 where the different contributions are highlighted.

$$\zeta\,[t(\boldsymbol{q})] = t_a(\boldsymbol{q})t_c(\boldsymbol{q})E_t(\boldsymbol{q})E_s(\boldsymbol{q}) \tag{2.1}$$

The different contributions are: $t_a(\mathbf{q})$ is a top hat function describing the effect of the objective aperture, $t_c(\mathbf{q})$ is the exponential of the aberration function and $E_t(\mathbf{q})$, $E_S(\mathbf{q})$ are envelope functions related to the partial temporal and partial spatial coherence, and **q** represents a two-dimensional vector in the reciprocal space. There exists an optimal defocus of the objective lens by which the CTF can be optimized and the highest amount of information can be extracted from the EPW. This condition occurs at the so-called Scherzer focus [133,134]. Finally, a highly magnified representation of the sample or its diffraction pattern is revealed, depending on whether the projector system is focused on the image plane or on the back focal plane, respectively. The image intensity is then given by equation 2.2 where $\psi_{ep}(\mathbf{r})$ is the wave function of the exit plane wave and $t(\mathbf{r})$ is the complex transfer function in the real space **r**.

$$I(\boldsymbol{r}) = |\psi(\boldsymbol{r})|^2 = \left|\psi_{ep}(\boldsymbol{r}) \otimes t(\boldsymbol{r})\right|^2 \tag{2.2}$$

The ray diagrams showing how the different lens/apertures are used in combination when the TEM is operated in imaging or in diffraction mode are shown in Figure 2.2.

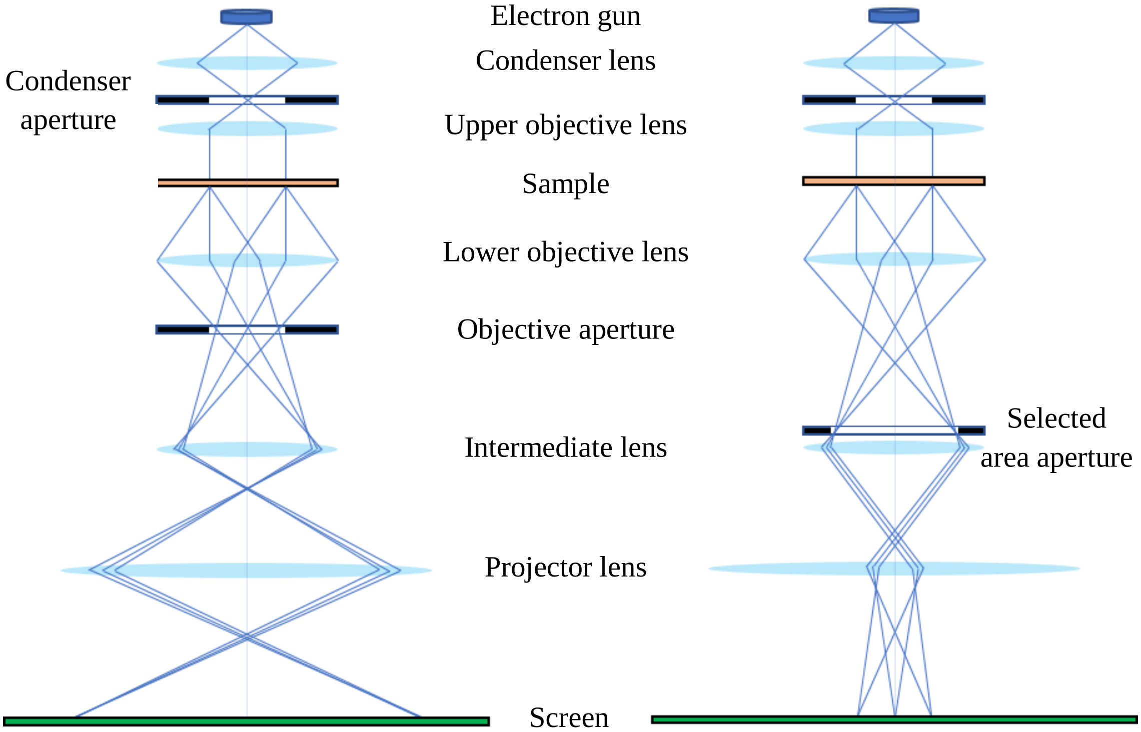
Condenser aperture
Electron gun
Condenser lens
Upper objective lens
Sample
Lower objective lens
Objective aperture
Intermediate lens
Selected area aperture
Projector lens
Screen

Final image

Diffraction pattern

Figure 2.2 – Schematic diagram showing the ray diagrams in two different setups available in TEM mode.

TEMs allow reaching much higher resolutions than normal VLMs or other techniques such as x-ray diffraction (XRD). This can be explained by the use of the Rayleigh criterion showed in equation 2.3, where λ is the ray wavelength, μ is refractive index of the medium in between the lenses and α is the convergence semi-angle of the aperture [131]. This formula defines, in diffraction-limited imaging, the smallest distance at which two different features can be resolved. Wavelengths of electrons accelerated by typical TEM voltages are shorter than those of x-rays (0.01-10 nm) and thus electron microscopes have a highest resolving power. Furthermore, due the particle nature of electrons, they have a much higher interaction with the atoms (nuclei + electron cloud) as compared to x-rays in which the interaction is just between the electromagnetic wave and the electron cloud [131].

$$r = \frac{0.61\lambda}{\mu \sin \alpha} \tag{2.3}$$

The wavelength of an electron can be calculated with the de Broglie relation given in equation 2.4, where *h* is the Planck constant, m_0 is the rest mass of the electron, *e* is the electron charge, *V* is the accelerating potential and *c* is the speed of light. Considering that the velocities of electrons in typical commercial TEMs (with operating voltages of 60-300kV) approach the speed of light, relativistic effects need to be taken into consideration. These effects, considered in equation 2.4, include significant length contraction, time dilation and an increase of mass.

$$\lambda = \frac{h}{\sqrt{2m_0eV(1+eV/2m_0c^2)}} \tag{2.4}$$

Thus, for a typical operating voltage of 300 kV, the wavelength of the electron equals to 1.97 pm and the resolution achievable by the TEM is 48 pm, i.e. smaller than the average distance between two atoms in a solid. From equations 2.3 and 2.4 it is inferred that in order to increase the resolution of the TEM, one should employ electrons of high energy. This is only partially true since equation 2.3 gives the resolution criterion of an optical system which is solely limited by diffraction. Indeed, several TEMs were fabricated with very high accelerating voltages up to 3 MV [131], but no substantial improvement in their resolving power was demonstrated. This was partially due to the sample knock-on damage by the high-energy electrons [135]. However, there are many other resolution limiting factors affecting the TEM microscopes, mainly related to the brightness of the electron sources, the mechanical stability of the systems and the unavoidable aberrations of round electromagnetic lenses [134]. These limitations and how they can be overcome are discussed in the next section when describing the STEM operation mode and the associated analytical techniques.

2.1.2 STEM techniques

The working principle of STEM is very different from that of the conventional TEM method. In fact, when working in STEM mode, the condenser lenses and the condenser apertures between the source and the specimen create a strongly focused beam, the so-called electron probe [136]. A series of deflection coils then guide the convergent beam onto the sample which is scanned sequentially within a specific rectangular area, as shown in Figure 2.3. The wave function ψ_{in} incident on the sample is given by equation 2.5. Here, $\boldsymbol{r}$ is a two-dimensional vector located in the sample plane (r_x,r_y), $\boldsymbol{k}$ is the vector composed of (k_x,k_y) located in the reciprocal space of the Fourier transform $F(\boldsymbol{k})$, shown in equation 2.6 and 2.7 [137].

$$\psi_{in}(\boldsymbol{r}) = F\{\psi(\boldsymbol{k})\}(\boldsymbol{r}) \tag{2.5}$$

$$F\{f(\boldsymbol{r})\}(\boldsymbol{k}) = \iint_{-\infty}^{\infty} f(\boldsymbol{r}) e^{-2\pi i \boldsymbol{k}\cdot\boldsymbol{r}} d^2\boldsymbol{r} \tag{2.6}$$

$$F^{-1}\{f(\boldsymbol{k})\}(\boldsymbol{r}) = \iint_{-\infty}^{\infty} f(\boldsymbol{k}) e^{2\pi i \boldsymbol{k}\cdot\boldsymbol{r}} d^2\boldsymbol{k} \tag{2.7}$$

When the electron wave interacts with the sample, the amplitude and phase will be altered by the so-called transmission function T(r), reported in equation 2.8.

$$T(\boldsymbol{r}) = e^{i\varphi(\boldsymbol{r})} \tag{2.8}$$

The wave, after the interaction with the sample, is defined by equation 2.9 where $\mathbf{r}_p$ is the position of the probe (r_{px},r_{py}) with respect to the sample.

$$\psi_{out}(\boldsymbol{r},\boldsymbol{r}_p) = \psi_{in}(\boldsymbol{r}) \cdot T(\boldsymbol{r}+\boldsymbol{r}_p) = \psi_{in}(\boldsymbol{r}) e^{i\varphi(\boldsymbol{r}+\boldsymbol{r}_p)} \tag{2.9}$$

The lenses present below the sample, guide the wave to the detector located in the far field and perform a second Fourier transform, defining the so-called detected wave $\psi_D(\boldsymbol{k},\boldsymbol{r}_p)$ shown in equation 2.10.

$$\psi_D(\boldsymbol{k},\boldsymbol{r}_p) = F\{\psi_{out}(\boldsymbol{r},\boldsymbol{r}_p)\}(\boldsymbol{k}) = F\{\psi_{in}(\boldsymbol{r})e^{i\varphi(\boldsymbol{r}+\boldsymbol{r}_p)}\}(\boldsymbol{k}) \tag{2.10}$$

Since we are dealing with a convergent electron beam, there are no diffraction spots like in normal TEM mode. Indeed, a diffraction disk (also called bright-field disk) is formed, and its size is related to the convergence angle created with the optical system. The intensity of the diffraction disk is given by equation 2.11.

$$I_D(\boldsymbol{k},\boldsymbol{r}_p) = \left|\psi_D(\boldsymbol{k},\boldsymbol{r}_p)\right|^2 \tag{2.11}$$

With the detection step 2.9 the phase of the electron wave at the detection plane is lost but, as explained later, there are different techniques to retrieve this component. The transmitted and scattered electrons are typically collected at various concentric annular detectors with different ranges of collection angles located at the diffraction plane. In this way, different information about the sample can be collected simultaneously. Usually, three main detectors are present in STEMs. The bright field (BF) detector is placed in the center of the optical axis and records the forward-scattered electrons. If we consider the principle of reciprocity, BF STEM and conventional TEM imaging generate an equivalent phase contrast governed by the aberration of the lenses and their associated CTF [138]. In BF STEM, the atomic columns appear as dark spots, but the contrast can be altered due to variations in the sample thickness. This makes the interpretation of the images more complicated. The second detector is the annular dark field (ADF) detector. In ADF, electrons scattered at higher angles (few tens of mrad) are collected and the incoherency of the signal is enhanced. Lastly, the high-angle annular dark field (HAADF) detector a shape similar to that of ADF but with a higher collection angle range, usually from 100 to a few hundreds of mrads. This high angle allows detecting nearly only incoherent Rutherford scattered electrons and obtaining images with strong chemical contrast. The image intensities are proportional to $Z^{\sim 1.6}$, where the phase information cancels out, allowing a much easier interpretation of the recorded micrographs. These three detectors are shown in Figure 2.3. There are also some other imaging modes such as the annular bright field (ABF). In some microscopes, this imaging mode makes use of the BF detector but the central part of the disk is removed. ABF imaging can also be achieved by using a combination of two annular dark field detectors. These approaches allow detecting the light atoms present in the sample.

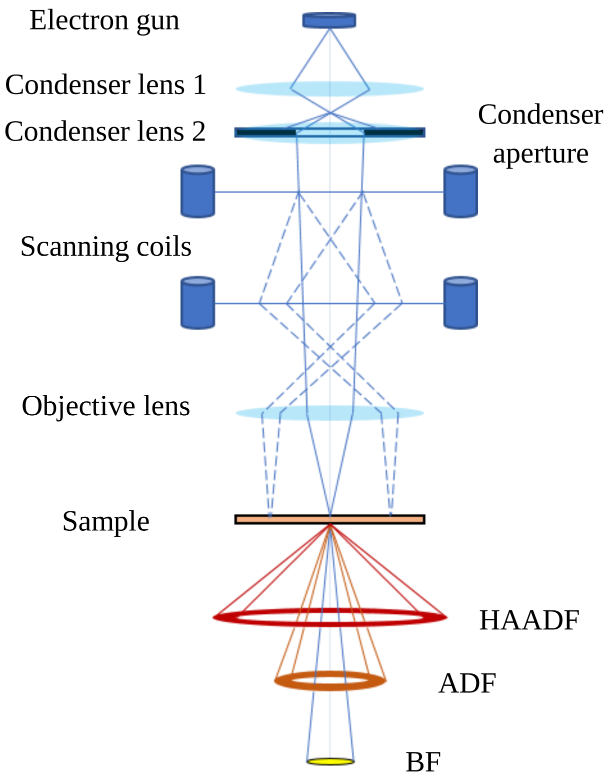

Figure 2.3 – Schematic diagram of a typical STEM setup showing how the electron beam is deflected by the scanning coils and the transmitted and scattered electrons are collected at different angles by the three detectors.

Concerning the achievable resolution, we saw in the previous section that, in conventional TEM imaging, the information limit transferred in phase contrast is related to the CTF of the lenses affecting the EPW. In STEM mode, the resolution achievable in the microscope is given mainly by the size of the electron probe scanned on the specimen plane, which is defined by an illumination (or condenser aperture), as shown in Figure 2.3 [134]. However, this aperture leads to the formation of an Airy pattern at the objective plane, characterized by a central maximum surrounded by several concentric lobes of decreasing intensity. We can choose the first zero of the Airy pattern as the radius δ_D of the diffraction-limited electron probe. This value, δ_D, expresses the size of an electron probe solely determined by the geometry of the coherent illumination and is given by the Rayleigh criterion reported in the equation 2.3 in the previous section. Thus, the width of an electron probe increases with increasing λ and decreasing convergence angle α. It is important to highlight that, in order to resolve certain lattice spacings, the convergence angle must be large enough such that the diffraction disks at the diffraction plane overlap. For example, in BF STEM imaging there are two regions of overlap given by the direct beam and two opposite diffracted beams. The overlap is described by the 0.61 factor present in the Rayleigh criterion [134]. When the diffraction disks do not overlap, the lattice spacing cannot be resolved. These considerations about the diffraction limit of the electron probe are purely geometrical and do not take into account the microscope specifications. In fact, as introduced in the previous section, there are other factors limiting the resolution of the electron probe, i.e. the aberrations [134]. Spherical aberration in STEM arises because the rays passing the pre-field of the objective lens in a distance from the optical axis are brought to focus closer to the lens than rays that run near the optical axis. Thus, the different rays do not meet in a single focal point after the lens, but they form a broad disk. This results in an increased electron beam radius, reducing in the resolution of the instrument. In fact, in a certain distance from the Gaussian focal plane, there is an area where the rays form a disc which is distinctly smaller. This is the so-called disk of least confusion and defines the smallest achievable electron probe. Its radius is given by the equation 2.12, and the constant C_S describes the spherical aberration of the pre-field lens.

$$\delta_S = {}^1\!/_4 \; C_S \alpha^3 \tag{2.12}$$

It is important to note that the relationship between the probe size and the convergence angle is opposite to the one described in the diffraction-limited electron probe; see equation 2.3. So, the reduction in probe size occurring when the aperture angle is increased in the diffraction limit is actually increasing the effect induced by the spherical aberration, and vice-versa. Then, it is very important to find the correct balance in order to optimize the two relationships. An optimal convergence angle exists and, at the Scherzer focus, is given by equation 2.13.

$$\delta_{min} = 0.43\sqrt[4]{C_S \lambda^3} \tag{2.13}$$

Nowadays, state-of-the-art microscopes are able to correct the spherical aberrations in the microscope, allowing a net improvement in the resolution of TEMs. The spherical aberration correctors present in the microscopes exploit an important property of geometrical aberration which is the possibility to sum them up [134]. In this way, if we consider the lens A with spherical aberration S_A and lens B with spherical aberration S_B, the total spherical aberration will be simply given by the sum of two. This aspect, known as “Addition Theorem”, allows us to concatenate several lenses such that the final spherical aberration output is null. This correction is based on the use of multi-pole lenses in two specific ways: correctors with two hexapoles and correctors combining quadrupole and octupole elements. These multi-pole correctors induce a negative spherical aberration, able to counter-balance the intrinsic spherical aberration of the microscope.

In the presence of a spherical aberration corrector system, the resolution of the microscope will be limited by another type of aberration called chromatic aberration. The electrons emitted by the source will have a distribution of energies rather than a single energy. When reaching the electromagnetic lenses, they will be deflected in different ways depending on their wavelength. In this way, only those electrons perfectly matching the nominal energy will be deflected in the correct image plane. All the others will find the focal point behind or in front of that plane, hence resulting in a disk of confusion instead of a point-like image of the source. As in the case of the spherical aberration, the probe size will become larger the more chromatic aberration is present in the microscope and the relationship is described by equation 2.14.

$$\delta_C = C_C \alpha \, {}^{\Delta E}/_{E} \tag{2.14}$$

Here, Cc represents the chromatic aberration constant of the lens, α is the convergence angle and ΔE corresponds to the energy spread of the electron source. A lot of research and engineering methods have been applied in order to limit as much as possible the effects induced by chromatic aberrations. The main strategy relies on the use of electron sources with very narrow energy distribution. Initially, thermionic sources like W or LaB_6 have been used to generate the electron beam but, nowadays, they have been replaced mostly by Schottky emitters and cold field emission guns (cFEG). The latter, in particular, can create a highly coherent beam with a very high brightness and a very low spread of the emission energy, usually around 0.3 eV [131]. The implementation of an electron monochromator allows to further reducing the energy spread below 100 meV. Finally, being the electron source of finite dimensions, the electron probe cannot have a lower size than that. The only way to reduce its dimensions to a point-like image of the source would be to increase the demagnification to infinite but this would lead to a zero-current beam. In Figure 2.4, the probe size is represented as a function of the semi-convergence angle by taking into account all the limiting factors explained up to now.

Now that the working principle of a TEM in scanning mode has been explained, I list all the different techniques associated to STEM that have been used in this research project, such as energy-dispersive x-ray (EDX) spectroscopy and electron energy-loss spectroscopy (EELS). An explanation of their working principle and the information that can be extracted with them is explained.

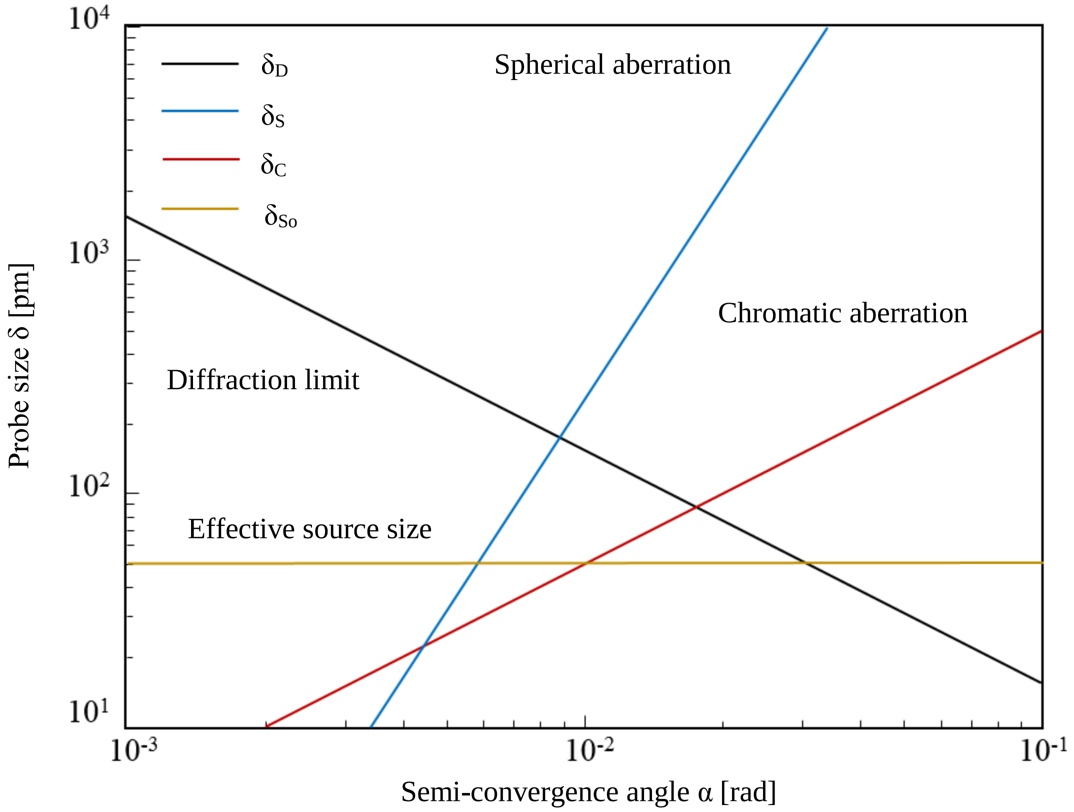

Figure 2.4 – Graphical representation of how the diffraction limit and the different aberrations can affect the electron probe size as a function of the semi-convergence angle. For spherical-aberration corrected microscopes, the chromatic aberration becomes the most limiting factor. Ultimately, this can be corrected by using a strongly coherent source or a monochromator (reproduced after [134]).

EDX This technique is one of the most widely used to extract the chemical composition of a specimen. It is based on the inelastic interaction of the electron beam with the electrons present in the atom's inner shell or core [131]. Each shell is classified depending on the distance from the nucleus with K being the closest shell, L the intermediate and M the farthest shell. Basically, some of the highly energetic electrons of the electron beam interact with those of the atoms present in the sample. If more than a certain amount of critical energy E_c is transferred to an electron located in a specific shell, it will be ejected from the atom, leaving an empty hole. Since the atom is now energetically unstable, an electron from the outer shells will decay to occupy the vacant site, decreasing the overall energy to the ground state and nearly stabilizing the system. The reality is that this process occurs by multiple transitions and not by a single event, depending on the complexity of the electronic structure and the number of electrons occupying the different shells [131]. This relaxation process will induce the emission of either an X-ray or an Auger electron. The latter is an electron with typically low binding energy to which a certain amount of energy has been transferred allowing it to escape the shell. In general, it is easier to detect x-rays than Auger electrons since they have a much higher energy. In fact, most of the x-rays generated during the decay process are able to escape the specimen. It is important to note that the associated emitted energy both for x-rays and Auger electrons has a characteristic value equal to the difference between the energy at the vacant site and the energy of the original shell of the decaying electron. This process can be observed in Figure 2.5.

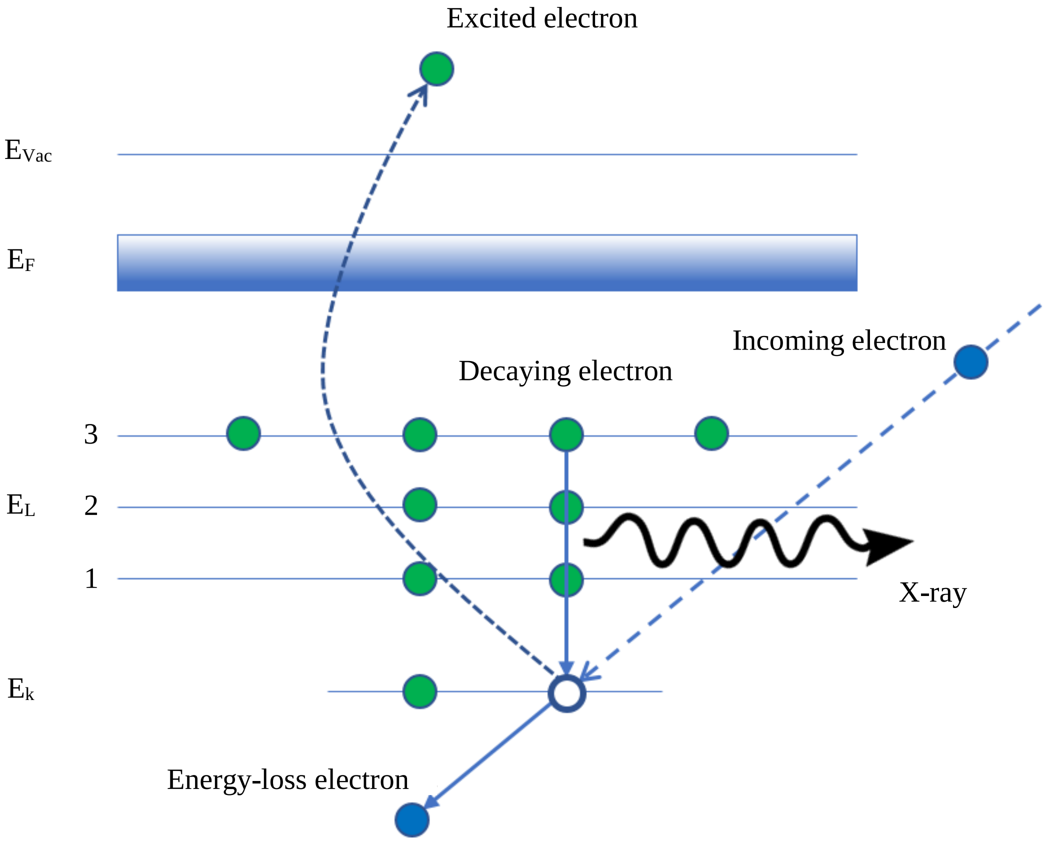

Figure 2.5 – Diagram showing the different energy levels for K and L shells in a Ne atom. The incoming electron transfers a sufficient amount of energy to an electron in the K shell such that it can escape the potential of the atom and be released in the vacuum. An electron from the outer shell L_3 decays at the K level releasing an x-ray of characteristic energy equal to the difference between these two levels.

The energy of the emitted x-rays can be detected by means of a detector located at a short distance above the sample. The characteristic energy will reveal which element emitted those specific radiations. Beside the generation of x-rays and Auger electrons, the electrons can also interact with the Coulomb field of the atom creating a background emission of non-characteristic energy called Bremsstrahlung radiation.

The amount of energy needed to ionize an atom strongly depends on its atomic number and it increases with the number of protons binding the core electrons to the nucleus. For example, ionizing an atom with fully occupied K, L and M shells like in the case of Nickel will require a much larger amount of energy with respect to the ionization of a Nitrogen atom in which only the K and L shells are occupied. However, providing an energy E_c can be not enough to ionize an atom since a higher amount of energy must be provided. This value can be defined with the over-voltage U which is given by the ratio between the beam energy E_0 and the critical energy E_c [131]. The absolute value of the ionization cross section can be calculated by the use of equation 2.15 where e is the electron charge, b_s and C_s are constants related to the specific shell and n_s are the number of electrons in that specific shell.

$$\sigma_T = \left(\frac{\pi e^4 b_s n_s}{E_0 E_c}\right)\left(\frac{c_s E_0}{E_c}\right) \tag{2.15}$$

A very important advantage of using EDX in STEM is the strong localization of small features thanks to the very fine probe. Single atomic column detections have been demonstrated [139]. Beside single point acquisitions, the spectra can be acquired also along specific trajectories along different interfaces or over an entire area of the sample. Then, the intensities of the emission peaks can be plotted as a function of their position, obtaining line profiles or intensity distribution maps. The number of emitted x-rays can be increased by illuminating the sample for a longer time with a higher beam current. This procedure can improve the efficiency of the detection process. It is important, however, to understand that a very high resolution, especially when performing atomic-resolution STEM, a high exposure time and a high current performed on a very small region, can increase drastically the probability of damaging the sample [140]. For this reason, it is always critical to find a good balance among the different parameters. EDX can be used also to quantify the amount of a specific element present in a specific region. Usually, the transitions related to the K shells are used for this purpose since they have a higher detection efficiency with respect to the L or M transitions [141]. Different types of detectors have been developed in the last decades but, in state-of-the-art microscopes, x-rays are normally detected by the use of Si-drift detectors (SDD) [131,138]. This element is composed of a series of concentric rings of p-doped Si implemented in a n-doped Si crystal disk. When x-rays enter the surface of the detector opposite to the Si rings, a certain number of electrons are produced and collected by the p-rings which will convert them in an electric signal. This tool allows obtaining higher detection efficiencies at a reduced applied voltage.

EELS As explained in the previous section, some of the high energetic electrons can interact in an inelastic way with the atoms of the sample by transferring a certain amount of energy to the electrons present in the shells. After this interaction, the incoming electrons will have an energy lower than their initial one. Depending on their energy, a magnetic prism disperses the electrons by exploiting the Lorentz force. Then, a CCD camera acquires a spectrum called electron-energy-loss spectrum where the electron counts are plotted as a function of the energy they have lost due to the inelastic process [131]. A microscope with a typical post-column EELS setup is depicted in Figure 2.6. As a first approximation, the spatial resolution achievable with EELS can be defined by the dimension of the electron probe. However, other aspects are significant to the spatial resolution of EELS, such as the mechanical and electric stability of the instrumentation, and the elastic scattering in the specimen, particularly in thicker specimens. Aside, inelastic scattering itself is somewhat delocalized, especially at lower energy loss [142]. Energy resolution depends on the design and stability of the microscope and spectrometer, the type of electron source and whether a monochromator is used. Additionally, the resolution of core-loss fine structures is considerably affected by the core-level width and scattering of the excited electron, that is the initial-state and final-state broadening [142]. Thus, EELS-dedicated STEMs are often equipped with aberration correctors, cFEG sources and monochromators, leading to an energy resolution in the order of tens of meV [143–146]. Such a high energy resolution is opening up new possibilities in the determination of vibrational states and energy gaps [147–152].

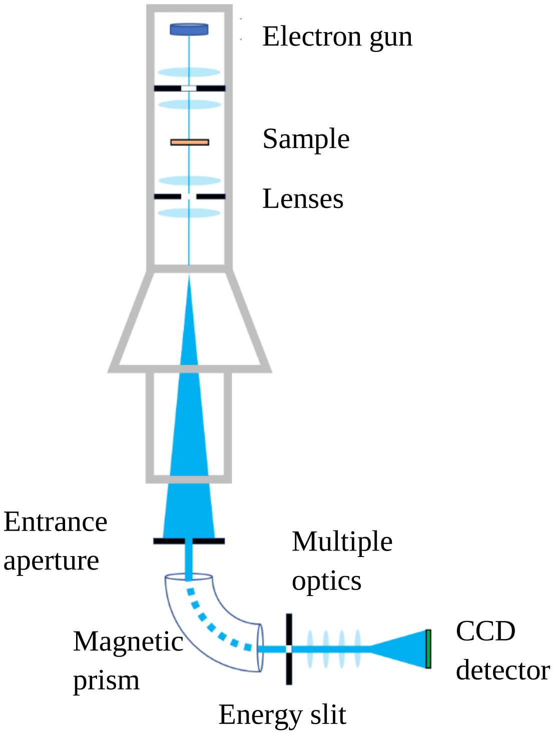

Figure 2.6 – Scheme of a typical TEM with a post-column spectrometer. The beam enters the spectrometer through an entrance aperture and pre-prism focusing and alignment coils. Then, the electrons are deflected by means of a 90° magnetic prism which disperses the electrons depending on their energy. A series of lenses is finally used to guide the electrons to a CCD camera from which a spectrum profile can be extracted through vertical integration. The energy slit located right after the magnetic prism can be used to filter the dispersed electrons in order to select only specific energy ranges.

The incoherent scattering event leading to an energy-loss of the incoming electrons can be described with the dielectric formalism, where the probability σ that an electron is scattered into a solid angle ∂Ω suffering from an energy loss equal to ∂E by equation 2.16 [153]. Here, it is assumed that the electron beam interacts with the entire solid via Coulomb interactions. The term Ç represents the energy-loss function of the material, θ is the scattering angle, t is the foil thickness and ε is the dielectric function equal to $\varepsilon_1+i\varepsilon_2$, i.e. the sum of the real and imaginary part of the dielectric function.

$$\frac{\partial^2\sigma}{\partial\Omega\partial E} \propto Ç\left(\frac{-1}{\varepsilon(E,\theta)}\right)\frac{t}{\theta^2+\theta_E^2} \tag{2.16}$$

Different types of information can be obtained with EELS and are in some way complementary to those of the EDX. In fact, also by performing EELS line profiles and maps it is possible to extract compositional information of the specimen, with the advantage that lighter elements are easier to detect [154]. However, as described in the previous equation, many other properties can be investigated depending on which range of the spectrum is analyzed. The EELS spectrum can be mainly divided in two regions: the low-loss and the core-loss sections. The low-loss region spans from 0 to ~ 50 eV and its analysis is often referred to as valence EELS (VEELS) because the electron beam interacts inelastically with the valence electrons of the material, inducing a limited loss of energy [155]. Here, the electronic and optical properties of the specimen can be extracted. The investigation of VEELS allows also to determine the energy gap of the material [148].

The low-loss region of the spectrum is mainly constituted by five contributions:

- Zero-loss peak (ZLP): this feature is given by the forward elastically scattered electrons which did not lose any amount of energy when interacting with the atoms in the sample [131]. The number of detected electron counts associated with the ZLP is the highest in the entire spectrum. The intensity of the ZLP may be used to obtain the specimen thickness by measuring its relative intensity with respect to the rest of the EELS spectrum [131,156]. This feature can also be used to give a rough estimation of the energy resolution by measuring the full width at half maximum (FWHM) [157].
- Dielectric losses: this type of contribution occurs in the 0-10 eV range and it is given by the loss of energy due to the excitation of single valence electrons to the conduction band [153]. Since this feature is present immediately after the ZLP, it is necessary to use a monochromator, which enables energy resolutions in the meV range and a clear separation from the ZLP.
- Volume/surface plasmon losses: when a highly energetic electron beam is transmitted through the sample, a certain amount of energy can be transferred to the electron cloud of the atoms which can undergo a displacement from its original position. The amount of energy lost by the incoming electron is in the 2-30 eV range and it has the second most pronounced intensity after the ZLP [157]. After the incoming electron has passed by, the loosely bound electrons of the atoms start to oscillate collectively in order to relocate to their original position. This oscillation is called bulk or volume plasmon and can give information on the electron density of the atoms present in the material [155]. The bulk

plasmon is related to the free-electron density cloud, which changes with the chemistry and the bonding state of the specimen. Hence, this feature has been used to quantify in an indirect way the fractions of elements present in the sample [158]. In fact, the volume plasmon energy is linearly proportional to the composition, as described in the empirical equation 2.17, where $E_p(0)$ is the plasmon energy loss for the pure component and C is the composition [159–163]. In TEM thin samples, the transmitted beam can also induce electron oscillations on the surface or at the interfaces. These oscillations are called surface plasmons [164]. The associated energy losses are lower with respect to the bulk plasmon losses and can be visible around 1-5eV.

$$E_p = E_p(0) \pm C\left({}^{dE_p}/_{dC}\right) \tag{2.17}$$

- Radiation losses: The oscillation of loosely bound electrons can occur also through the TEM sample thickness inducing the creation of guided light modes which can be both radiative and non-radiative depending on the material, its geometry and its attitude to emit light when undergoing a decay process. Cherenkov radiations are another type of beam-induced radiations which may generate energy losses in the electron beam [157]. Basically, when a high energy electron goes through the material, its velocity can become even higher than that of the light, if the real part of the dielectric function is large enough. The electron is then retarded in the material releasing a certain amount of energy. This energy loss is also called retardation loss. The position of this loss peak in the spectrum is right after the ZLP and can overlap with the one of the energy gap. The latter can also experience a slight shift to higher energies due to the Cherenkov radiation [148,165].
- Phonons: Vibrational excitations are also responsible for energy losses usually in the range of 10-100 meV, but this extremely low value did not allow their visualization in EELS spectra. Recently, thanks to the use of dedicated STEM instruments, they have been demonstrated [149,152]. This was possible by using a specific monochromator design able to reduce the energy resolution of the spectrum down to 9 meV [152]. In this way, the phonon peaks were resolved and separated from the strong intensity of the ZLP. This feature can be particularly important for the development of low-loss infrared nanophotonic devices and the investigation of thermal properties at the atomic scale [149,166].

The second region of the EELS spectrum, i.e. the core-loss region (E_{loss} > 100 eV), is mainly used to determine the composition of the specimen. However, this part of the spectrum presents also other features which provide important information on the analyzed material [131]. Electron energy-loss near edge structures (ELNES) provide information on the bonding and valence state of the atoms. Another type of feature is the extended energy loss fine structure (EXELFS) from which the local coordination of atoms can be extracted.

In order to obtain the larger amount of information from the acquired EELS, it is important to consider some practical aspects related to the data analysis. For example, in order to determine the exact energy-loss of the plasmon peaks, the subtraction of the ZLP is necessary since it could induce a small shift in energy [167]. This can be done by applying some pre-defined subtraction models, such as the inverse power law function, the Gaussian or Lorentzian function or a combination of them [148]. However, this step is more critical during the determination of the energy gap.

2.1.3 Off-axis electron holography

An electron wave interacting with an electromagnetic potential undergoes a modification of its amplitude and phase [131]. However, being the intensity of the signal at the detector given by the square modulus of the transmitted wave, the phase shift is lost together with all the information connected to the electric and magnetic potentials of the specimen. A way to investigate the local electric and magnetic fields in nanostructured materials, by retrieving the phase component of the transmitted wave, is to use the so-called off-axis holography in TEM (in both conventional or Lorentz modes) [168]. Due to the charged states of dopants in semiconductors, holography can give information on their distribution inside nanostructures by measuring the local electric fields and potential variations [169–176]. In this technique, a positively charged electrostatic biprism (also called Möllestedt biprism) placed below the specimen plane is able to overlap two different electron waves: one which has passed through the specimen and represents the object wave and a second one guided through the vacuum only that represents the reference wave. The overlapped wave will be recorded on the camera as a fringe pattern, the so-called electron hologram. With respect to other techniques like differential phase contrast, electron holography allows a quantitative measurement of the phase variation, thus making possible quantitative estimation of local electrostatic potential and magnetic fields.

In order to explain the procedure to extract the phase from the hologram, one should consider the intensity distribution in normal BF-TEM imaging mode. When dealing with the coherent image formation in BF-TEM mode, the electron wave $\psi_i(\boldsymbol{r})$ in the image plane is given by equation 2.18, where $A_i(\boldsymbol{r})$ and $\varphi_i(\boldsymbol{r})$ are the amplitude and phase components, respectively [177].

$$\psi_i(\boldsymbol{r}) = A_i(\boldsymbol{r})e^{i\varphi_i(\boldsymbol{r})} \tag{2.18}$$

As explained in the previous section, the intensity recorded by the detector is given by the square modulus of the wave function and, in particular, by the square modulus of its amplitude, as reported in equation 2.19. Here, it is clear that the information regarding the electron phase is lost in conventional imaging.

$$I(\boldsymbol{r}) = |\psi_i(\boldsymbol{r})|^2 = |A_i(\boldsymbol{r})|^2 \tag{2.19}$$

However, in electron holography, an additional term related to the reference wave that did not pass through the specimen contributes to the recorded intensity in the image plane. Therefore, the reference beam that can be expressed by a tilted wave has to be added to the incident wave term, as in equation 2.20. Expanding the right term of the expression we obtain equation 2.21, where three separate contributions can be extracted.

$$I_{hol}(\boldsymbol{r}) = \left|\psi_i(\boldsymbol{r}) + e^{2\pi i k_c \cdot \boldsymbol{r}}\right|^2 \tag{2.20}$$

$$I_{hol}(\boldsymbol{r}) = 1 + A_i^2(\boldsymbol{r}) + 2A_i(\boldsymbol{r})\cos[2\pi k_c \boldsymbol{i} \cdot \boldsymbol{r} + \varphi_i(\boldsymbol{r})] \tag{2.21}$$

The components are: the intensity of the electron wave through the vacuum, the intensity of the electron wave transmitted through the sample and a set of interference fringes given by the cosine term. In order to extract the phase and amplitude information from the hologram, a Fourier transform should be applied to the recorded hologram. Equation 2.22 shows the different contributions present in the reciprocal space obtained when performing such Fourier transformation.

$$\begin{aligned} FT[I_{hol}(\boldsymbol{r})] = \delta(k) + FT[A_i^2(\boldsymbol{r})] + \delta(k + k_c) \times FT\left[A_i(\boldsymbol{r})e^{i\varphi_i(\boldsymbol{r})}\right] + \\ + \delta(k - k_c) \times FT\left[A_i(\boldsymbol{r})e^{-i\varphi_i(\boldsymbol{r})}\right] \end{aligned} \tag{2.22}$$

The first contribution is a peak located at the origin of the reciprocal space which corresponds to the Fourier transform of the reference image; the second peak centered at the origin represents the Fourier transform of a conventional BF-TEM image of the specimen; the third term centered at -k_c corresponds to the Fourier transform of the desired image wavefunction; the fourth term centered at +k_c represents the complex conjugate of the wavefunction. The obtained complex image is then processed in such a way that only one of the two side bands is selected and shifted to the center. Then, an inverse Fourier transform is performed, obtaining the complex wavefunction. Considering equations 2.23 and 2.24, it is possible to calculate the amplitude and the phase images from the complex image [177]. After performing the reconstruction, a reference window is selected at the vacuum close to the region of interest to set the phase value in vacuum to zero. In the present reconstruction process we used a commercially available plug-in implemented in digital micrograph [178].

$$A = \sqrt{Re^2 + Im^2} \tag{2.23}$$

$$\varphi = tan^{-1}\left(\frac{Im}{Re}\right) \tag{2.24}$$

Being the amplitude image comparable to an energy-filtered BF-TEM image [177], its contrast is affected by dynamical scattering effects and can give information about the thickness homogeneity of the sample. On the other hand, the phase image can give important information on the sample since the phase shift is sensitive to electromagnetic fields present in the specimen. In fact, the phase shift can be written as the sum of two different contributions related to the electrostatic and magnetic fields (equation 2.25).

$$\varphi(x, y) = C_E \int_{-\infty}^{\infty} V(x, y, z)dz - {}^{e}/_{\hbar} \int_{-\infty}^{\infty} B_Z(x, y, z)dz \tag{2.25}$$

$$C_E = \left(\frac{2\pi}{\lambda}\right)\left(\frac{\mathrm{E}+E_0}{E(\mathrm{E}+2E_0)}\right) \tag{2.26}$$

In this equation, C_E is a constant (equation 2.26) that depends on the microscope's accelerating voltage, V is the electrostatic potential, e is the electron charge, $\hbar$ is the Planck's constant and B_Z is the z-component of the magnetic field present in the sample. E is the nominal energy of the electron beam and E_0 is the rest mass energy of the electrons. In the case that no applied electric fields or magnetic potentials are present along the electron beam path, then the phase variation originates from the mean inner potential V_o of the sample which can be calculated from the equation 2.27, where t represents the thickness variation along the x and y directions. Some artifacts can be introduced by biprism or magnetic lenses imperfections and instabilities [177]. For this reason, a second hologram of the vacuum is taken immediately after the one acquired on the specimen, without modifying the electro-optical parameters of the microscope. Then, a subtraction between the phase images of the sample and the one of the vacuums is performed and allows correcting for such artifacts. This process will give phase shifts ideally related only to the variation of the mean inner potential. Since this project deals with III-V semiconducting NWs, we skip the analysis of the magnetic contributions to the phase shift, which are still a matter of discussion for nanomaterials.

$$\varphi_e(x, y) = C_E\, V_0\, t(x, y) \tag{2.27}$$

However, other contributions to the phase are often present which could increase the difficulty of interpretation of the obtained phase maps. These additional contributions could be stray fields in the vacuum, dopant-induced variations and dynamical diffraction effects. Other than that, it is important to define some crucial parameters and experimental conditions necessary to obtain optimal holograms. In order to do that, we will use Figure 2.7, where a scheme of a typical off-axis holography setup is depicted.

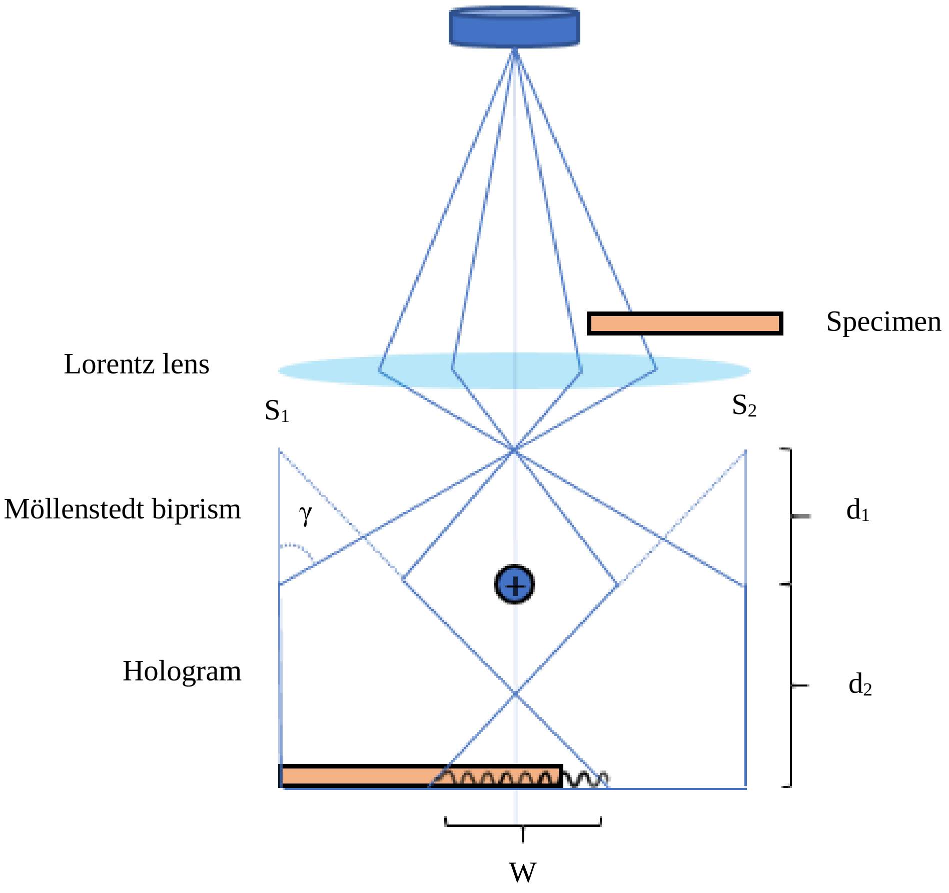

Figure 2.7 – Diagram showing the working principle of a typical off-axis holography setup in Lorentz mode. Half of the electron wave interacts with the sample while the other half is transmitted in the adjacent vacuum. A series of apertures and lenses guide the beam through a biprism which then overlaps the reference beam with the interacted beam in the image plane. This process gives rise to an interference fringe pattern from which information on the electrostatic and magnetic potentials of the sample can be extracted. Adapted from [177].

A cFEG electron source is typically preferred in order to have a highly coherent beam. The coherency is necessary to have an interference fringe pattern of sufficiently high quality within a reasonable acquisition time. Moreover, the microscope stability plays a key role in the quality of the recorded holograms, in particular for atomic-resolution holograms. There exist then three experimental parameters extremely important to obtain a high-quality reconstructed phase image. The first one is the overlap width (W) which represents the overlapping distance between the reference wave and the object wave. This value is given by the equation 2.28 where d_1 is the distance between the focal plane and the biprism, d_2 is the distance between the biprism and the image plane, R is the radius of the biprism and γ is the deflection angle imposed by the voltage of the biprism. In general, a higher voltage of the biprism induces a larger overlapping region. However, the latter can also change depending on the applied strength of the projector and objective lenses. A smaller radius of the biprism wire can also give less Fresnel fringes coming from the external parts, increasing the simplicity of the hologram interpretation.

$$W = 2\left(\frac{d_1+d_2}{d_1}\right)\left(\gamma \frac{d_1 d_2}{E(d_1+d_2)} - R\right) \tag{2.28}$$

Another crucial parameter is the interference fringe spacing s which gives the distance between two consecutive fringes and it is given by equation 2.29. As opposed to the overlap width, this value is inversely proportional to the voltage of the biprism wire. The spatial resolution in the final phase image is approximately three times the fringe spacing, and, for this reason, it is important to choose a certain value of the biprism voltage so that the dopant-induced features can be resolved. The reason for this spatial resolution limit has been demonstrated by Völkl et al. [179] and it is connected to the complex wavefunction reconstruction process. By assuming that the image wave is limited in bandwidth of spatial frequencies ranging from 0 to k_{max}, and that the autocorrelation function is centered around $k = 0$ extending as far as $2k_{max}$, the isolation of one sideband can only be achieved for those spatial frequencies which do not overlap with the autocorrelation. Since each sideband is covering a circle with radius k_{max}, then the maximum reconstructable spatial frequency is limited by $k_{lim} = k_c - 2k_{max} \leq k_{max}$ which holds only if $k_c \geq 3k_{max}$. For this reason, the mask applied in the previously mentioned reconstruction process is significantly important to determine the final spatial resolution of the reconstructed phase and amplitude images.

$$s = \lambda\left(\frac{d_1+d_2}{2\alpha d_1}\right) \tag{2.29}$$

The last parameter to take into account is the achievable visibility of the fringes (μ). This value, associated with the contrast of the image, is related to the number of electrons (N_{el}) collected per pixel and it is able to determine the lowest phase resolution (φ_{min}) by equation 2.30 and 2.31. Here, *SNR* represents the signal-to-noise ratio, and I_{max} and I_{min} are the maximum and minimum intensities of the interference fringes, respectively. However, the fringe contrast is inversely proportional to the applied voltage of the biprism and, for this reason, it is important to find a balance between achievable spatial resolution (given by fringes spacing) and the phase resolution (given by fringes contrast). A longer acquisition time will result in a larger electron count, an increase of the SNR and, thus, an improvement of the fringe visibility. It is however important to understand that longer acquisition times require very stable instruments, so that an interference pattern of sufficient quality can be recorded during which specimen and/or beam drifts must be negligible. Also, there exists the additional risk of saturating the camera.

$$\varphi_{min} = \left(\frac{\mathrm{SNR}}{\mu}\right)\sqrt{2/N_{el}} \tag{2.30}$$

$$\mu = \left(\frac{I_{max}-I_{min}}{I_{max}+I_{min}}\right) \tag{2.31}$$

2.1.4 TEM instrumentation

JEOL JEM ARM-200F This microscope is installed in the noise-free labs of the IBM-Research laboratory in Rüschlikon (ZH). These labs were developed to eliminate disturbances arising from external electromagnetic fields, mechanical and seismic vibrations, acoustic noise, and temperature and humidity fluctuations. The instrument has a cFEG electron source and is operated at 80, 120 and 200 KV acceleration voltages. It is equipped with two correctors for the spherical aberration, one for the STEM mode and one for the broad-beam transmission mode. This microscope was mainly used for imaging and EDX spectroscopy at the atomic level in STEM mode. This was performed with a convergence semiangle of 25 mrad in combination with a HAADF detector with inner and outer collection semiangles of 90 and 170 mrad, respectively. In typical operation conditions for the experiments described in this thesis, the microscope provides an estimated spatial resolution of 80 pm. Atomically resolved EDX maps were performed by using a JEOL Dry SD100GV Si drift detector with a 100-mm^2 detection area. Moreover, EELS analysis were carried out by using a Gatan Enfinium EELS spectrometer. For the EELS data acquisition, the convergence and collection semi-angles were set to 25.3 and 33 mrad, respectively. An exposure time of 0.4 s and a dispersion of 0.05 eV/channel were used in combination with a current of about 4.8 µA. For these values, the energy resolution measured at the FWHM of the zero-loss peak in vacuum was ~0.55 eV.

FEI Titan Themis This microscope is equipped with an X-FEG electron source working at 80/300 kV. This type of source provides a high total current, stability and long lifetime with a considerable increased brightness which permit maximizing the performance in each mode of operation. Quantitative EDX mapping was performed in STEM mode by using a SuperEDX system (ChemiSTEM technology) equipped with four Si drift detectors. The spectra were recorded with a beam current of 0.3 nA, 0.8 nm pixel spacing and a dwell time of 10 μs per pixel. Holography experiments were performed in conventional TEM mode. Given the dimensions of the nanostructures, the Lorentz lens was used as image forming lens instead of the objective lens (as shown in the optical scheme in Figure 2.7) in order extend the field view over the entire region of interest. The microscope is equipped with a Möllenstedt biprism covered with a gold layer whose applied potential was set between 120 and 190 V depending on the specific hologram, orientation of the NW and used magnification. The obtained fringe spacing was then in the 2-3 nm range with a resulting spatial resolution of 6-9 nm. Concerning the phase contrast, we noticed an improvement by increasing the acquisition times and consequently the number of electrons impinging on the camera. However, the longer the acquisition time, the more relevant became the microscope's instabilities, able to decrease the overall phase contrast. For this reason, acquisition periods ranging from 5 to 13 seconds were used and the recorded phase contrast was in the 30-45% range depending on the specific hologram and experimental conditions. The camera is a FEI Ceta 16M 4k x 4k CMOS-based camera with fiber optic coupled scintillator. The number and size of the pixels is 4000 and 14 μm, respectively, with a dynamic range larger than 16 bit.

2.2 Cathodoluminescence

When the amount of energy transferred to the energy levels of the atoms in the material is large enough, an electron can be promoted from the valence band (VB) to the conduction band (CB), creating a so-called electron-hole pair [131,180]. Since this state is unstable, an electron can decay from the CB to the VB, releasing a photon with a specific energy. This energy corresponds to the difference between the CB and the VB and equals the energy gap of the material $E=h\upsilon$ where h is the Planck's constant and υ is the frequency of the emitted photon. Since semiconductor materials have an energy gap around 1 eV, the frequency of the emitted photons will be in the visible light range. This is of practical importance in the study of semiconducting materials since the energy gap can be determined by measuring the frequency of the cathodoluminescence radiation [131]. Indeed, this technique was applied to semiconductor materials and in particular to determine the variations in the energy gap due to strain-induced phenomena [181]. In this project, CL was performed by means of a SEM in order to determine the effect of the doping implementation on the energy gap of III-V NWs. The CL experiment was performed with an Attolight SEM-CL microscope, operated at a temperature of 12 K. The system was equipped with a Newton CCD and an iHR320 spectrometer with a wavelength accuracy of ± 0.20 nm. An acceleration voltage of 10 kV and a current in the order of 1 nA were used. The exposure time and the pixel size were 100 ms and 2 nm, respectively. The emitted light from the NWs was captured by a dispersive spectrometer with a focal length of 32 cm and a grating of 150 l/mm and detected by a Peltier-cooled CCD camera, resulting in a spectral resolution of 1.6 nm.

2.3 Sample preparation

TEM lamellas for atomic-resolution imaging and EDX spectroscopy were prepared with an FEI Helios Nanolab 450S focused ion beam (FIB) instrument by means of the following process. In order to minimize gallium implantation by the Ga^+ ion beam, the region of interest was protected with a 100-nm-thick platinum layer deposited by electron beam induced deposition at a voltage of 5 kV and 100 pA of current. After isolating the primitive lamella with rough U-cuts and the creation of fiducials for the automated cutting process employing a voltage of 30 kV and decreasing currents (Figure 2.8a), a tungsten Omniprobe probe was used to extract the section from the substrate (Figure 2.8b). Then, the sample was attached to an Omniprobe TEM copper grid (Figure 2.8c). Finally, the lamella was thinned down to electron transparency (i.e. below 100 nm) with a voltage and current of the Ga^+ ion beam of 5 kV and 41 pA, respectively (Figure 2.8d). For the quantitative EDX, EELS and off-axis holography, the NWs were transferred to a holey carbon-coated TEM copper grid simply by rubbing it against the wires in a very gentle way. Thus, gallium contamination due to FIB sample preparation was avoided. The same process has been applied for the structures investigated by SEM-CL.

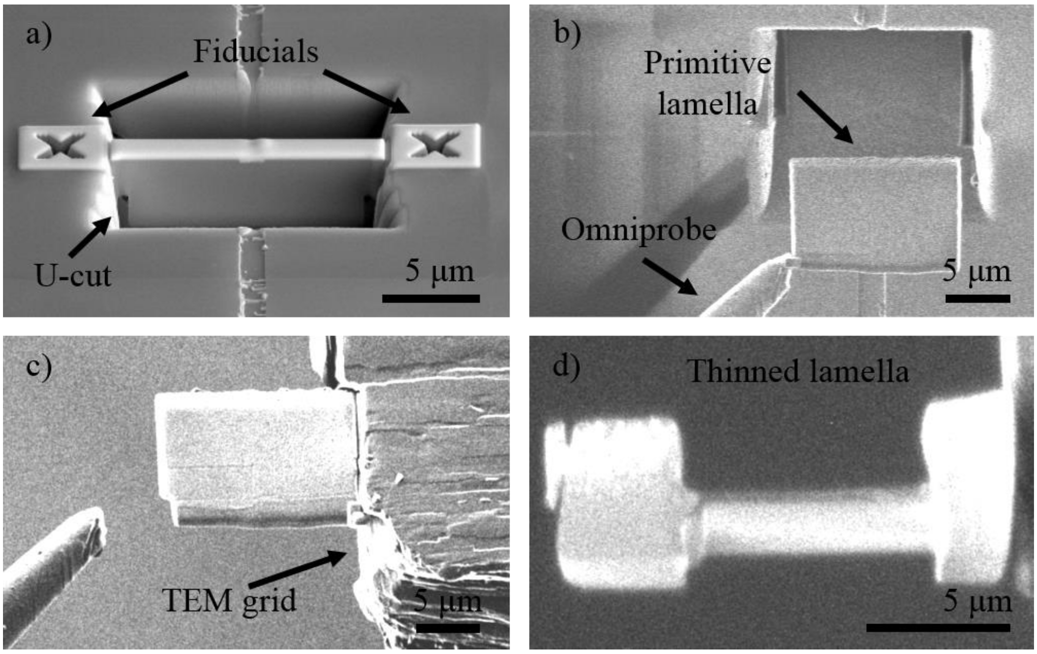

Figure 2.8 – SEM images representing the different steps in the creation of a TEM lamella by FIB. (a) First, the U-cuts are performed around the isolated area of interest. (b) Then, by means of a probe, the primitive lamella is removed from the substrate and (c) attached with Pt to a TEM copper grid. (d) Finally, a gentle Ga polishing at 5 kV and 41 pA of current is performed to thin down the lamella to electron transparency.

2.4 3D modeling and simulations

Simulations based on 3D models allow studying the influence of crystallographic defects on the physical properties and electronic structure of nanomaterials. In the last decade, they have been of fundamental importance in order to understand the behavior of materials at the nanoscale with or without a first experimental interpretation [182–184]. In this project, we have replicated the crystal structure of III-V NWs by means of a 3D modeling tool called Rhodius, developed by the University of Cadiz [185]. This software allows creating supercells of complex systems by controlling specific parameters like crystal orientation, crystal tilting and the different facets present in the material. Moreover, distortions, defects, and displacements of the lattice can be realized in the model [186]. Figure 2.9 is an example of a III-V core-shell structure built with Rhodius. These 3D models have been used as an input for the DFT simulations. DFT was introduced by Hohenberg and Kohn in 1964 [187] and it has been frequently used to make solid-state calculations [188–190]. In this theory, the properties of atoms, molecules or condensed phases, i.e. many-electron systems, can be determined by the use of functionals of the electron density. In particular, DFT is based on the Kohn-Sham formalism stating that "The total energy of a many-electron system is uniquely determined by the electron density function; the minimum of the energy functional corresponds to the correct ground state electron density for the system". This defines an effective potential of the system called Kohn-Sham potential. Two main approximations were introduced to the energy functional of the system. The first one is the local density approximation (LDA) which assumes that the energy functional in a specific point of the crystal depends solely on the value of the electron density in that specific point and it is taken to be that of a homogeneous electron gas [191]. However, this approximation fails in systems where the density undergoes a rapid change, such as in molecules. In order to address this pitfall, the generalized gradient approximation (GGA) was introduced by taking into account the entire gradient of the electron density. However, this method is well known to fail in determining accurately the bandgap of materials [184,192]. In order to improve this aspect single point calculations were performed using the hybrid functionals developed by Heyd-Scuseria-Ernzerhof (HSE06) [193]. These types of functionals are able to express the exact exchange energy among different electron density systems.

In this project, DFT calculations were performed within the Gaussian plane-wave method as implemented in the CP2K package with double-zeta valence polarized (DZVP) basis sets for the representation of the Kohn-Sham orbitals, with plane-wave cut off for the charge density of 600 Ry. An initial geometry optimization was performed using the Perdew-Burke-Ernzerhof (PBE) with GGA exchange correlation functional. Then, in order to obtain a more accurate energy gap value, single-point calculations using hybrid functionals were performed. To speed up the calculations, the auxiliary density matrix method with FIT6 auxiliary basis sets was employed. Maximally localized Wannier functions were extracted using CP2K.

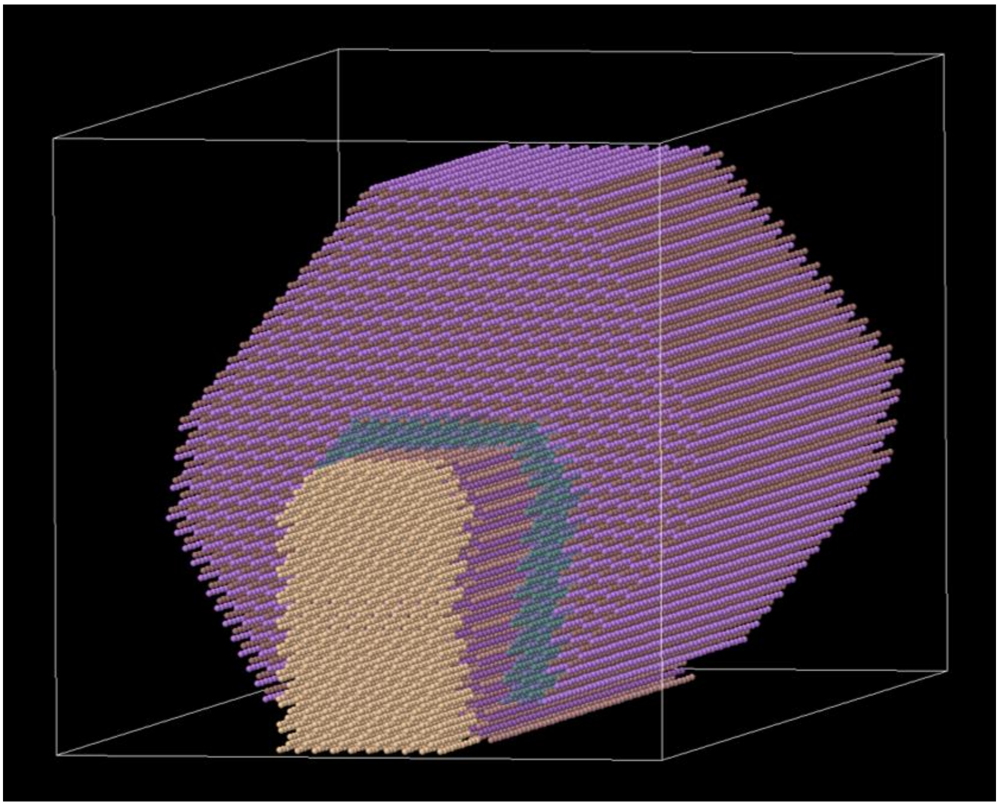

Figure 2.9 – 3D model realized with Rhodius representing a core-shell structure with an inner InAs NW core and an outer GaSb shell. The yellow atoms represent a small slice of the Si seed. The interface between the core and the shell is colored in green.

In the next chapter, the investigations performed on different sample systems are presented. Chapter 3 comprises the study performed on the monolithic integration of GaAs NWs on a Si (100) substrate for electronic application. The experiment led to the demonstration of the first defect-free structures reported in literature. Then, a particular type of defect which takes place when non-optimal growth conditions are applied, and the effect induced on the materials properties are analyzed in detail. Chapter 4 addresses the study of doped $Ga_xIn_{(1-x)}P$ and GaAs NWs integrated on Si for photovoltaic applications. The modifications induced by p-n dopants on the crystal structure, composition, and optical properties of the TASE grown NWs are here studied for the first time.

3 Integration of planar GaAs nanowires on a CMOS compatible substrate

The continuous scaling down of electronic devices has brought Si-based CMOS technology close to its limits, requiring novel materials and approaches to increase device performance, measured in terms of switching speed, and manufacturing profitability depended upon reduced cost per good device built. As previously explained, III−V NWs have evolved as promising candidates due to their superior properties and the possibility of integrating them with Si in heterostructures. Besides, they have great potential for use in active photonic devices. However, epitaxial integration of III-Vs on Si(100) remains challenging, mainly due to the formation of crystal defects, significantly reducing device performance. SAG [194,195] and epitaxial lateral overgrowth (ELO) [196–198] have both been demonstrated to reduce defects arising from lattice mismatch. The TASE method has the potential to minimize or even eliminate these structural imperfections, while entirely controlling the shape and dimension of the NWs by the template geometry. MOCVD is particularly well-suited for TASE because of the high selectivity of the deposition and the long surface diffusion length of the precursors, which facilitates filling of the template cavities. However, up to now, a high density of planar defects has been observed in TASE grown InAs and GaAs material systems [116,120] resulting in polymorphism or in the formation of charged defects when planar defects meet and merge. Therefore, the aim of this study is to gain an understanding of the III-V crystal growth in SiO_2 templates, to study the occurrence of stacking and mono-dimensional defects and their dependence on the growth conditions. In this research project, GaAs on Si is used as a model material system, with some results expected to be transferable to other III−V semiconductor material systems.

3.1 Nanowires growth

Templates were patterned by electron beam lithography at 100 keV (EBPG 5200+, Vistec) along the [110] direction on Si-on-insulator (SOI) wafers with (100) crystal orientation. First, Si fins are formed using dry etching (ICP, Oxford) (Figure 3.1a) and covered by SiO_2 using atomic layer deposition (Flexal, Oxford) and plasma enhanced chemical vapor deposition (System100, Oxford) (Figure 3.1b). The SiO_2 is removed at one end, and the Si fin within is partly back etched using tetramethylammonium hydroxide (TMAH). This results in {111}-terminated crystalline Si seed surfaces (Figure 3.1c). The detailed process is described elsewhere [120]. For this study, the templates investigated had a thickness of 40 nm (± 5 nm), width of 100 nm (if not otherwise specified), and a length of approximately 1000 nm with a spacing between parallel nanowires of 100 nm. The GaAs NW growth was performed by MOCVD using trimethylgallium (TMGa) and tertiary butylarsine (TBAs) precursors and a H_2 carrier gas at a total pressure of 8000 Pa (60 Torr). The group III partial pressure was kept constant at 29 mPa, while the group V pressure was varied to obtain nominal V/III ratios between 20 and 120. Just before growth, the substrates were immersed in diluted hydrofluoric (HF) acid (1:20 in H_2O) to remove the native oxide on the Si{111} seed surfaces inside the templates. Upon loading, the reactor was heated to 700 °C in a TBAs atmosphere and then ramped down to a growth temperature of 500−650 °C. Growth started with the introduction of a TMGa flow, with a typical growth time of 40−60 min. After growth, the substrates were cooled under a TBAs flow until reaching a temperature below 300 °C.

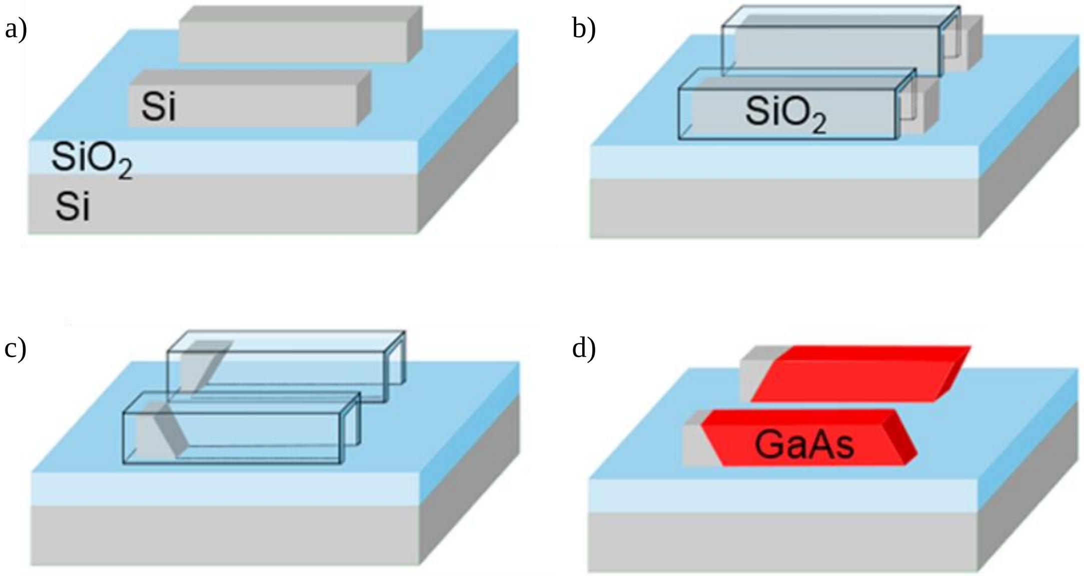

Figure 3.1 – TASE fabrication steps. (a) Si fin etching. (b) Template oxide deposition and one-sided oxide removal. (c) Si back-etching illustrated are the two possible (111) planes. (d) Epitaxy step and removal of template.

GaAs nanowires were initially characterized using a Hitachi SU8000 SEM. The SiO_2 shell surrounding the nanowires was removed using a HF solution. The GaAs structures were then closely investigated under various different angles in the SEM to determine the formed growth facets. For each growth run, a total of 60 randomly chosen nanowires were analyzed and classified into one of five types, to constitute a sufficient statistical sample. To allow for comparison of different growth runs, it was further ensured that the position of the nanowires analyzed was always in the center of the growth substrate and at the same location within the growth reactor. The length of all 60 nanowires was measured, and the average growth rate was calculated and matched with the corresponding faceting prototype. Data points presented in this study correspond to median values and the error bars to one standard deviation. The crystal quality of the single nanowires was investigated by HAADF-STEM both from the front and lateral view. The sample lamellas were prepared by FIB and inspected with a double spherical aberration-corrected JEOL JEM-ARM200F microscope operated at 200 kV.

3.2 Defect-free GaAs nanowires and tuning of their front facets

Analysis of growth facets forming during crystal growth yields valuable insights into the underlying crystal growth mechanism. Therefore, the dependence of facet formation on the growth parameters and orientation of the mask opening in ELO was studied very early on [199]. However, a detailed study on facet formation for TASE is missing so far. Here, the effect of facet formation and crystal morphology is studied by varying the growth conditions, i.e. growth temperature and nominal V/III precursor ratio. The results are statistically quantified. This leads to an improved understanding of the formation of twin defects and opens a path to reduce them. Figure 3.2 displays SEM images of GaAs nanowires, where various end facets are visible. The samples were grown at different growth temperatures and nominal V/III precursor ratios. In Figure 3.2a the wires can be identified within the partially filled SiO_2 nanotubes. Here, the GaAs appears brighter than the Si fins, which act as nucleation centers during the epitaxy process. At different growth conditions, different facet morphologies and growth rates appear. In the topmost image, an array of 20 nanowires is presented. The two SEM images in the center show facets at higher magnification and with added labels indicating the facet types. For the tilted images in Figure 3.2b, the SiO_2 oxide surrounding the nanowires was removed, allowing for a better identification of the nanowire facets. In order to analyze the growth, we have classified the end facets into five groups according to their specific geometry (Type I– V), and an additional group where growth failed (Type X). Figure 3.2c displays schematic illustrations of the three most common facet types observed in this study, labeled Type I, II, and III. The classifications are based on the following specific characteristics: Type I appears as a pointy tip when seen in the top view along [001], forming a 90° angle of two {110} facets and a 45° angle with the template walls. Accordingly, they have two large {110} facets and a small (111)B facet, suggesting that the [111]B growth rate is high, while the <110> growth rate is low. Two different versions of the same type are often observed which differ only by either pointing up- or downward as illustrated schematically in Figure 3.2c for Type I and II. The formation of these two versions depends on the geometry of the Si seed surface. The Si seed surface can consist of one large or two smaller {111} planes after TMAH etching, which means there are always two possible directions of {111} planes, as illustrated in Figure 3.1d. In addition, GaAs can nucleate on Si in (111)A or (111)B orientation, although As termination on Si is more likely to occur in the growth conditions used in this experiment. Correspondingly, (111)B facets can be formed in two directions on these Si{111} planes.

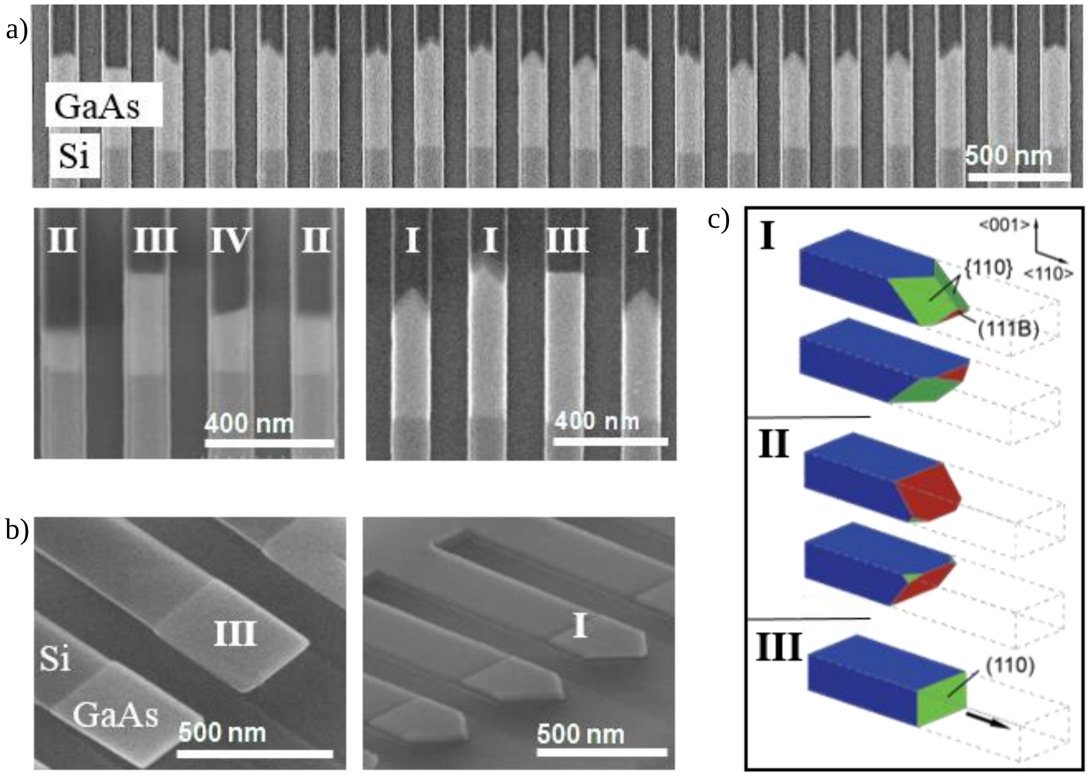

Figure 3.2 – (a) Secondary electron (SE) SEM plane view images of GaAs nanowires arrays grown in SiO_2 templates on a Si(001) SOI wafer. The nanowires grow in-plane and along the [110] template direction. (b) SEM tilted view images where the SiO_2 templates have been removed. (c) Schematic illustration of the most common facet types. The flipped facets reflect the Si seed plane geometry. Type I: dominating {110} facets, small (111)B facet; Type II: small {110} facets, dominating (111)B facet; Type III: single (110) facet, no (111)B facets. Type IV with {112} facets is not illustrated.

Type II appears as a blurry edge forming a 90° angle with the template walls when seen in top view (Figure 3.2a). They have a large (111)B and two small {110} facets as illustrated in Figure 3.2c. In this case, the <111>B growth rate is suppressed and the <110> growth rate enhanced, resulting in large (111)B facets. This behavior has been attributed to a high As surface coverage at a high V/III ratio, leading to the formation of As trimers which prevents (111)B growth [200,201]. Type III appears as a sharp edge in a top view image, forming a 90° angle with the template. It can be described by a single (110) growth facet, perpendicular to the nanowire tube oriented in the [110] direction. In a study of vertical epitaxy of InAs nanowires on Si(110) via TASE, the occurrence of a (110) facet has also been observed [116]. In addition to these three most common facet types, two less frequent types are observed. Type IV features a (112) facet, forming an 18° angle with the template wall. This facet was also noted in GaSb epitaxy via TASE [202]. Type V nanowires are characterized by forming a 32° angle between the facet and a base perpendicular to the [110] (growth) direction. STEM analysis revealed the presence of a large (111)B facet, and a crystal orientation rotated with respect to the Si lattice. Finally, we also observed instances where the nanowire failed to fill the entire template width or nucleation, was initiated on the template sidewalls rather than the Si seed. Both cases are classified as Type X in this study.

Structural characterization at the atomic scale of the GaAs samples of Type I, II, III, and V was performed using aberration-corrected STEM. For all samples investigated, no threading dislocations or antiphase boundary defects were observed. However, the presence of TWs and SFs was often abundant in Type I, II, and V. Since the nanowires are grown along the [110] direction, formation of <111> planar defects either parallel or perpendicular to the growth direction can be observed. It is, therefore, crucial to analyze both the lateral and front cross sections of the crystal in order to conclude whether it is free of planar defects. The STEM analysis of a Type I nanowire is shown in Figure 3.3.

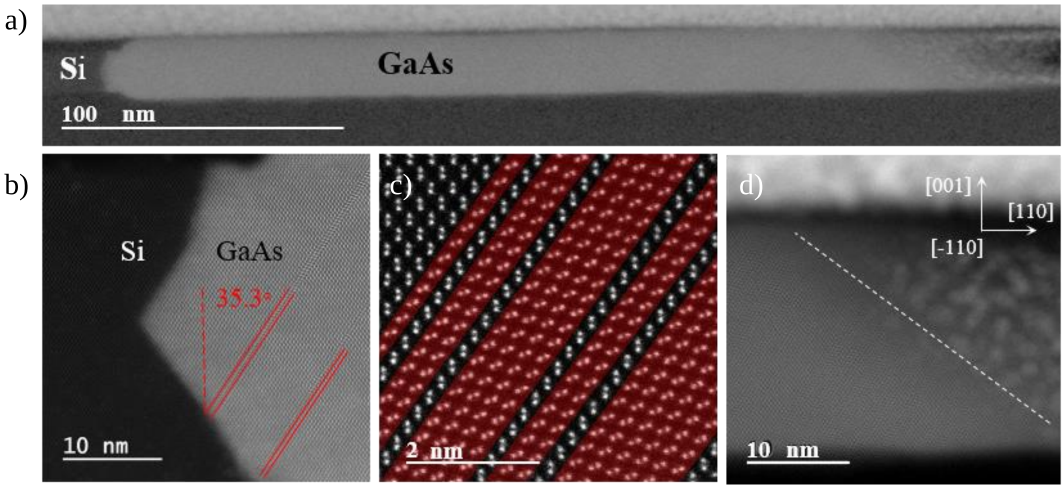

Figure 3.3 – HAADF-STEM images of a nanowire with end facet Type I. (a) Lateral overview of the nanowire. (b) Interface between GaAs and Si showing the presence of SFs (marked with red lines). The angle between the (110) and (11$\bar{1}$) planes is indicated. (c) Atomic resolution image of a highly defective region with red semitransparent sections highlighting the change in orientation of the GaAs dumbbells due to the presence of planar defects. (d) Nanowire end facet exhibiting an inclined growth front highlighted by a dashed white line.

Figure 3.3a shows a low magnification image of the entire nanowire, while panel (b) illustrates the interface between GaAs and the Si with the Si(111) seed facets resulting from the TMAH etch step described above. Different planar <111> defects can be observed at the interface region, highlighted with red solid lines. Figure 3.3c presents an atomic resolution image of a representative region of the nanowire with a high density of planar defects. The clearly resolved GaAs dumbbells switch orientation during growth by the formation of planar defects in the semitransparent red regions (both twin boundaries and intrinsic and extrinsic SFs). Here, we adopt the definition of Caroff et al. [101] where two sequential twin planes are considered to form a single wurtzite segment. This interrupts the stacking sequence, thus creating a single SF. Figure 3.3d presents the growth front of this Type I nanowire. The two coinciding {110} facets form a wedge when seen from the side along the $[\bar{1}10]$ zone axis, as indicated by the white dashed line. The (111)B facet cannot be distinguished in this cross-section due to the very reduced dimensions. In Figure 3.4, we displayed the defect density (number of twins per nanometer) along the entire nanowire shown in Figure 3.3. We observe a strong fluctuation of the number of planar defects but the overall average calculated along the entire length for multiple nanowires was circa 1.1 twins/nm and it is represented by the black solid line. Very similar results were obtained for Type II samples, also showing a similar density of planar defects along the whole structure.

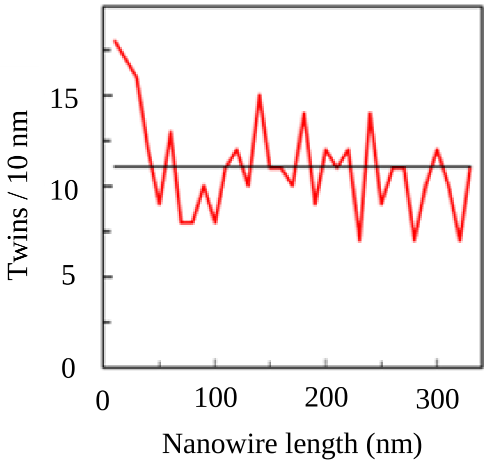

Figure 3.4 – Number of planar defects per nanometers along the length of the nanowire with an average of 1.1 twins/nm.

The structural analysis of a Type III nanowire with a (110) growth front is presented in Figure 3.5. Panels (a) and (e) show an overview of the lateral and front cross sections of the nanowire, respectively. Directly at the interface with the Si (Figure 3.5b), a total of four planar defects were detected, with the rest of the nanowire appearing entirely defect-free. Planar defects, running along the [110] direction, were observed in a previous work on InAs nanowires [115] and expected to occur here as well. Therefore, high-resolution images from both lateral and front directions were acquired as shown in Figure 3.5c and Figure 3.5f. In these micrographs, the GaAs dumbbells are clearly resolved in both viewing directions, clearly demonstrating the absence of any buried planar <111> defects within the STEM lamella. Figure 3.5d shows the nanowire (110) front facet, which appears sharp when viewed along the $[\bar{1}10]$ zone axis. The overlying brighter spots in this area are Pt residues deposited on top of the nanowire during the FIB lamella preparation. The selected STEM results presented in Figures 3.3 and 3.5 could be confirmed for a total of 10, 12, 9, and 1 nanowire with facet Type I, II, III, and V respectively. No defect analysis was performed for nanowires with {112} facets (Type IV), as their occurrence was very small. Overall, we observed that nanowires having a (111)B facet, i.e., Type I, II, and V, were highly twinned, irrespective of the (111)B facet size. Nanowires where such a facet is absent, i.e., Type III, were found defect-free.

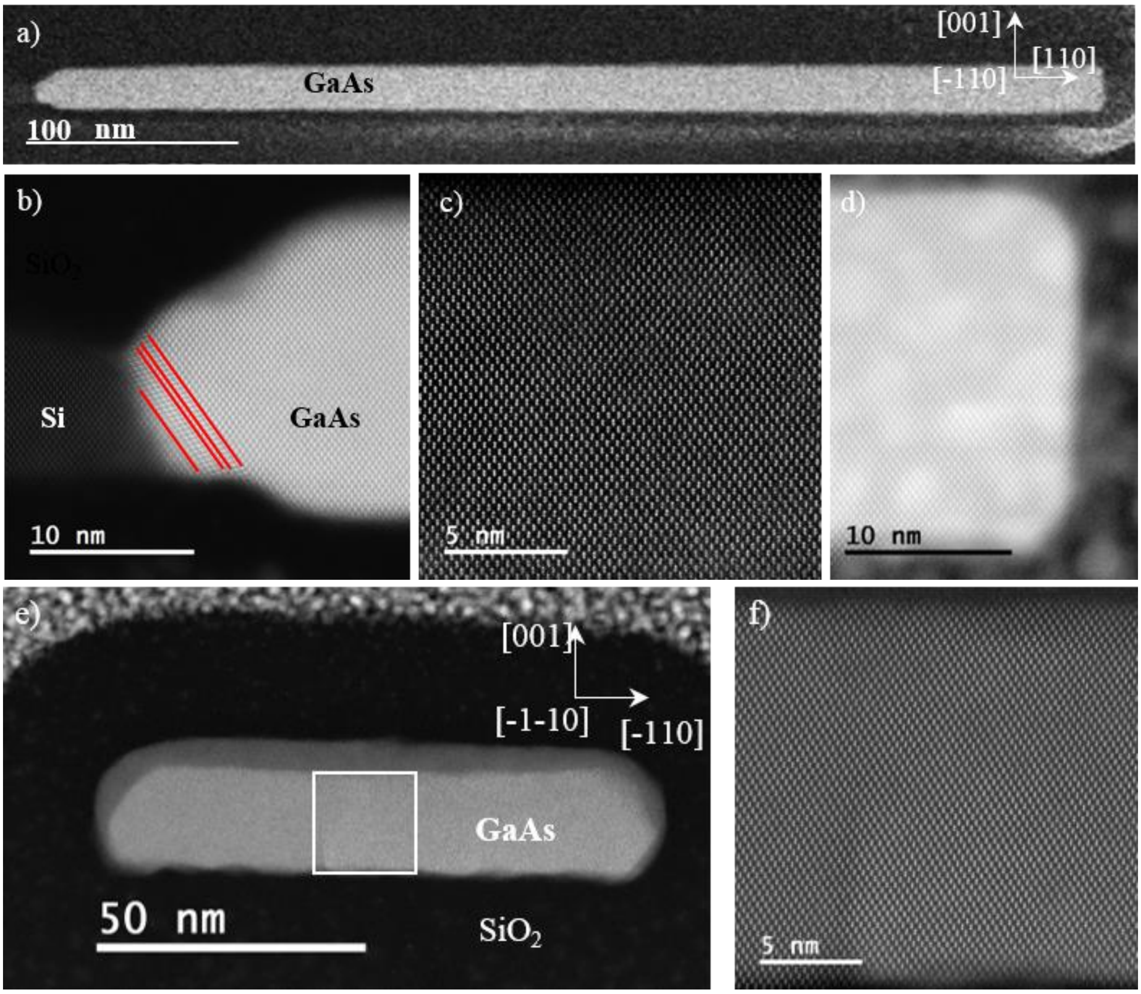

Figure 3.5 – HAADF-STEM images of nanowires with end facet Type III, grown at 550 °C and V/III ratio 120. (a) Lateral overview of the nanowire. (b) Si/GaAs interface. Four twin defects are directly located at the interface region. (c) No additional planar defects are present along the nanowire. (d) End of the nanowire with a (110) facet. (e) Front view overview of a similar nanowire grown at identical conditions. The darker shell around the GaAs nanowire is depleted in As (as identified by energy dispersive X-ray spectroscopy) caused by sample heating during optical spectroscopic experiments. (f) Enlarged view of the square indicated in panel (e). The clearly resolved GaAs dumbbells in these images are evidence of the absence of buried planar defects.

In order to quantify our findings, a statistical study on the dependence of the end facet on the growth parameters was performed. Having identified Type III as the preferred structure to result in a defect-free GaAs crystal, it is obviously desirable to find a parameter space to yield a high number of nanowires with the Type III facet. A series of epitaxy runs was accordingly designed. Most relevant in the epitaxy process are nominal V/III precursor ratio and temperature in the MOCVD chamber. Table 3.1 lists the overall growth runs performed for this study.

		Growth T (°C)						
		500	525	550	575	600	625	650
V/III	20	●	●	●	●	●	●	●
	70			●				●
	120	●	●	●	●	●	●	●

Table 3.1 – Investigated growth parameters for GaAs nanowire epitaxy by varying temperature and V/III precursor ratio.

First, the influence of the V/III ratio for two growth temperatures was investigated. The results are displayed in Figure 3.6. The occurrence of the various types in percent is plotted for three different V/III ratios at 550 °C (a) and 650 °C (b).

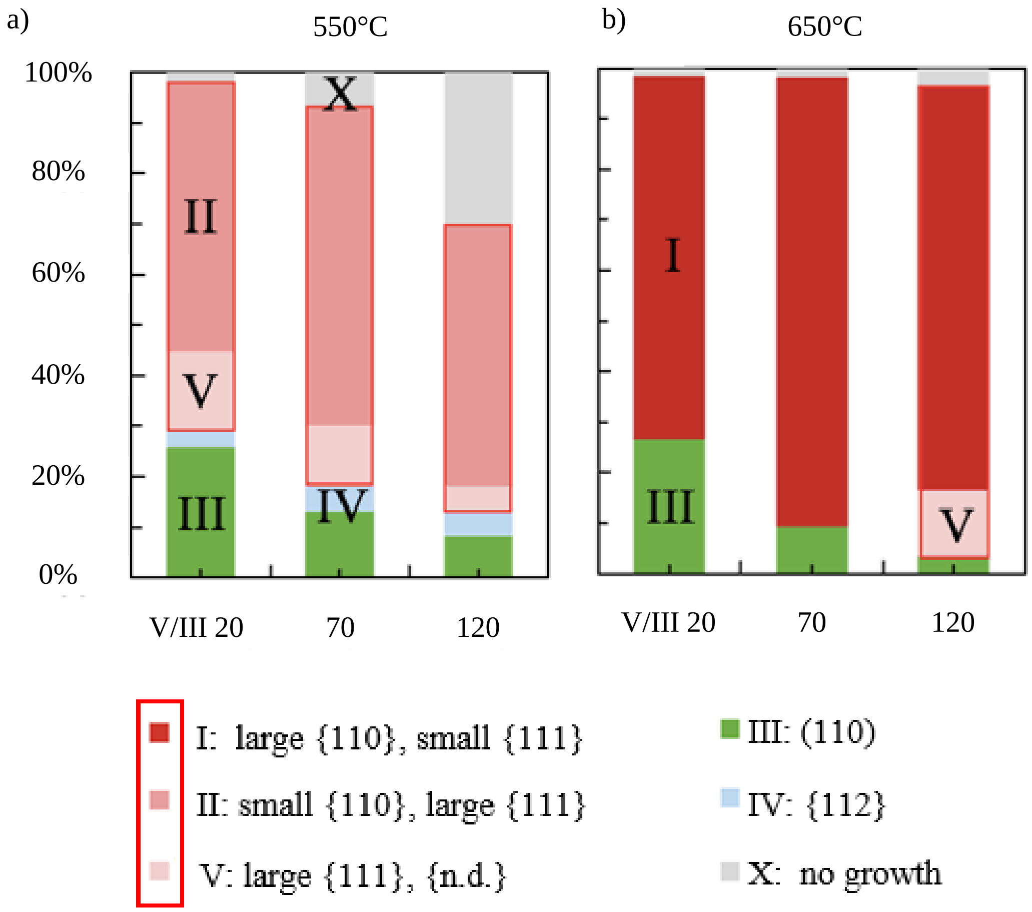

Figure 3.6 – Facet occurrence (%) as a function of V/III ratio at 550 °C (a) and 650 °C (b). Each data point represents 60 nanowires. Type I: large {110} facets, small (111)B facet; Type II: small {110} facets, large (111)B facet; Type III: single (110) facet, no (111)B facet; Type IV: {112} facets; Type V: large {111} facet, unidentified small facets; Type X: non epitaxial growth and/or not filled template.

All facet types containing (111)B facets, which were observed in STEM to be highly twinned, are displayed in different shades of red, e.g., Type I, II, and V. Nanowires with facets of Type III, observed as twin-free, are displayed in green. Overall the nanowire yield is consistently very high, as indicated by only a few nanowires denoted as Type X. However, at 550°C, the yield drops significantly with increasing V/III ratio, as nanowires fail to fill out the complete 100 nm wide template. A clear shift from Type II being prominent at 550 °C to Type I at 650 °C is observed. This indicates an abrupt change of these facet types with temperature and is more detailed in Figure 3.7 at a constant V/III ratio of 120. Here, the facet type abruptly changes from Type II to I between 600 and 625 °C. A more detailed analysis of the influence of growth temperature and V/III ratio is shown in Figure 3.8(a, b). The influence of the growth temperature from 500 to 650 °C on facet occurrence is displayed for V/III 20 and 120, respectively. At both high and low V/III ratio the change from Type I facets to Type II occurs abruptly, being shifted 50 °C higher at high V/III ratio (namely from 575 °C to 625 °C). We expect the occurrence of type I or II facets to be governed by the degree of As trimer formation on the (111)B facet of the nanowire, which prevents growth on this facet [200,201].

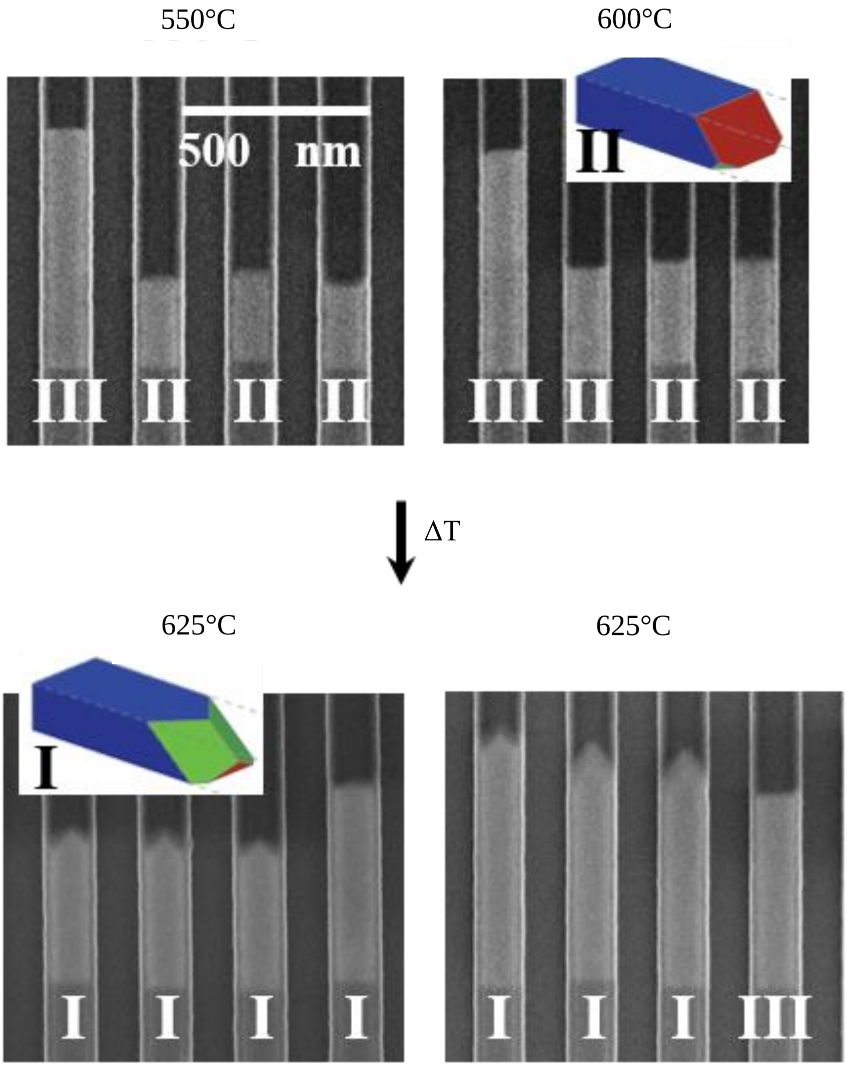

Figure 3.7 – SEM plane view images illustrating the transition from nanowire facet Type II to Type I with increasing growth temperature. Facet types are indicated. An increase of 25 °C (namely from 575 °C to 625 °C) leads to a well-defined transition from Type II to Type I. The V/III ratio, in this case, was 120 with 60 min growth time.

The desorption of As from the (111)B facet is an activation energy driven process with an exponential dependence on the growth temperature. The sudden change from facet type II to I with increased temperature thus reflects the onset of significant As trimer desorption from the (111)B facet. A higher V/III ratio shifts this onset to higher temperatures, where As desorption outweighs the higher As pressure. From this, we can conclude that a shift from V/III ratio 20 to 120 roughly corresponds to the effect of a temperature change of roughly 50 °C at the nanowire growth front. The overall yield of nanowire growth drops with decreasing growth temperatures. This effect, as shown in Figure 3.8b, is more pronounced at a high V/III ratio, occurring at higher growth temperatures. Yield for twin-free nanowires (Type III) is highest at a low growth temperature and low V/III ratio, where the (110) facet nanowires become the prevailing facet type with approximately 40% yield. However, we cannot deduce a simple trend of Type III formation with growth conditions. In Figure 3.8(c, d), the corresponding growth rates for nanowire Types I + II and Type III are presented. The growth rate of nanowires with a {111} facet (Type I + II) increases with higher temperature; for nanowires with a single (110) facet (Type III) it decreases. This is similar at both high and low V/III ratio; however, growth rates for Type I + II are slightly increased at low V/III. This effect is attributed to the increasing As-trimer formation on As-terminated (111)B facets at lower temperatures and higher V/ III ratios, as described above. For {110} facets, both Ga- and As-terminated, the opposite effect occurs, and growth rates are enhanced for a high As coverage. It should be noted that nanowire growth rates are significantly more inhomogeneous at a low V/III ratio, resulting in larger error bars, as reported in Figure 3.8c. Overall, the highest growth rates for nanowires with Type III facets are obtained at low growth temperatures. As such, it is favorable to grow Type III at a low growth temperature and a low V/III ratio.

In early discussions on defect formation in planar epitaxial growth [203], and in more recent works [204,205], it was shown that impurities located on the (hetero-) epitaxial interface can trigger bonding errors and SFs in {111} planes. The considered impurities can be extrinsic, e.g., carbon contamination, or intrinsic from a group III overdose, e.g., Ga cluster. Therefore, rigorous surface cleaning and adjusted growth conditions were found to be critical to achieve defect-free epitaxy [204,205]. In ELO the crystal grows laterally over a SiO_2 stripe and thus follows a SiO_2-III−V interface, which could also trigger SFs. For InP ELO on InP no SFs were observed in the overgrown layers, while in the heteroepitaxial case on a Si(001) substrate, rare occurrence of SFs was noticed [206] and is suggested to stem from residual stress of the Si-InP heterojunction area. Similarly, for GaSb ELO on (001) substrates no SFs for homoepitaxy as well as for heteroepitaxy on GaAs substrates were observed [207]. In TASE, SF-free growth of GaSb and InP was shown [115,202]. These observations indicate that impurities located on the SiO_2 surface are less critical as compared to impurities on semiconducting growth substrates. The absence of available chemical bonds on the oxide surface, as compared to the growth surface, might reduce the susceptibility for perturbing nucleation or distorted bond formation.

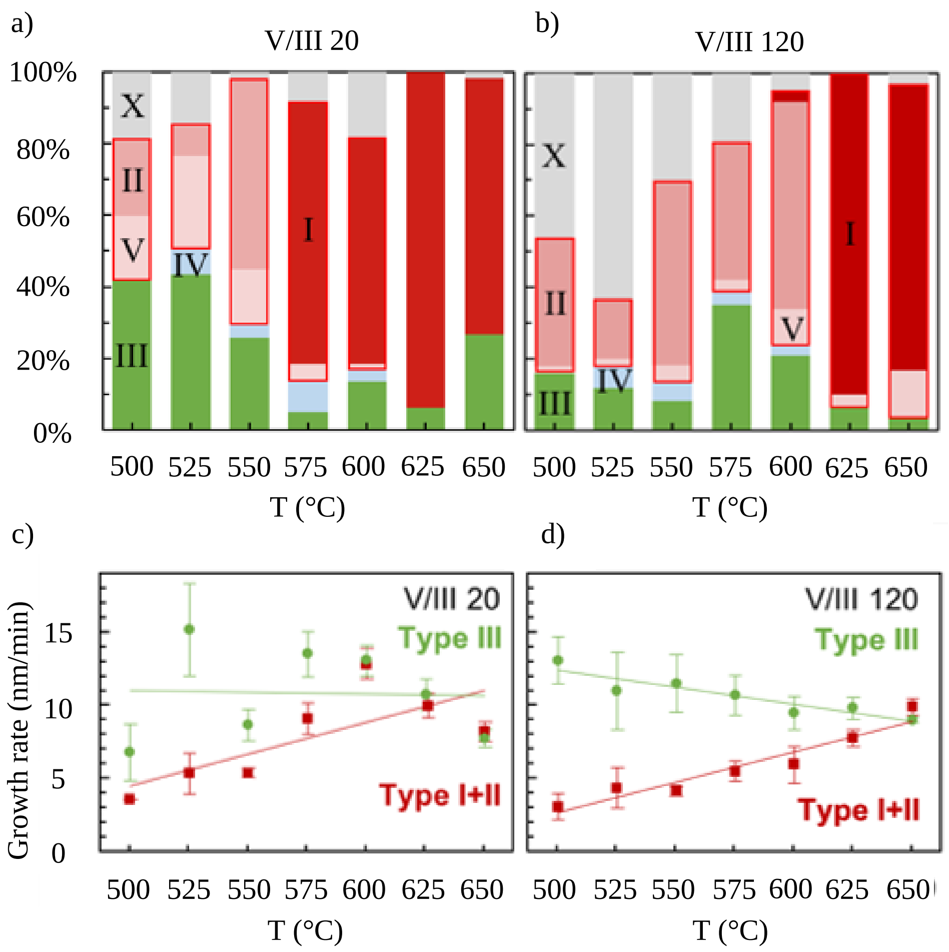

Figure 3.8 – Facet types and average growth rates as a function of growth temperature at V/III ratio 20 (a) and 120 (b). Each data point represents 60 nanowires, with each error bar corresponding to one standard deviation. Definition facets same as in Figure 3.6. Temperature-dependent growth rates of Type I, -II, and -III at V/III = 20 (c) and V/III = 120 (d).

In a mixed ELO/SAG approach of InGaAs on Si(111) [208], a shift from highly twinned to a twin-free InGaAs layer was observed by increasing the Ga flux during growth. The examples above have in common that the structure (growth plane) was ≥1 µm long and appears less affected by twin defects than smaller ones, likely because large and off-cut surfaces facilitate step-flow growth, which suppresses planar defect formation. The demonstration of a twin-free InGaAs layer on <111> oriented InGaAs was ascribed to the transition from a layer-by-layer to an island-like growth at high Ga flux [208]. Nanowire structures were not reported using ELO, but for SAG typically employing <111> oriented substrates. Under the assumption that the SiO_2 interface is not dominating twin formation, results from SAG experiments can provide valuable information on the occurrence of twinning in nanostructures. The origin of twin formation in SAG GaAs nanowires was investigated and attributed to growth parameter dependent surface reconstructions on the (111)B surface [209] and critical size of the nucleus [210]. While twin-free nanowires were

not achieved, a transition to twin-free material for larger structures and for higher growth temperatures was predicted. A more general approach to suppress twins is modifying the material composition, as was shown by adding Sb to InAs which suppressed twin-defect formation in InAsSb nanowires [211]. However, while effective, this approach is not always desirable.
For our nanowire structures studied here, we observe a strong correlation of twin defects with growth conditions that form (111)B growth facets. The twinning energy of the small GaAs (111)B surface is apparently not high enough to lead to twin-free nanowires. We find that a (110) growth facet results in defect-free nanowires since twins are not formed on this plane. The facet-dependent material defectivity further indicates that formation of twins is unlikely to derive from strain effects due thermal expansion mismatch, SiO_2 (template wall)−GaAs interactions or surface impurities. As the formation of nanowires with (111)B planes could not be completely suppressed under the conditions investigated in this work, further studies could explore the diameter dependence and/or surface preparation strategies for efficient formation of nuclei with a single (110) plane toward a high yield of twin-free nanowires.

In conclusion, we conducted a comprehensive study on in-plane GaAs nanowire growth on Si(001) substrates along the [110] direction via TASE. Growth parameters (V/III ratio and temperature) were correlated with crystal growth facets and structural analysis. The resulting nanowires were classified into five groups based on the shape of the end facets. STEM analysis revealed that nanowires containing a (111)B facet are always highly twinned, while exclusively those with a Type III single (110) facet were found to be defect-free. Yield for Type III nanowires was highest (40%) at low growth temperature and V/III ratio. However, a simple correlation of Type III facets with the growth parameters explored could not be established. Overall, these observations strongly indicate that twin formation does not derive from strain effects, SiO_2−GaAs interactions, or surface impurities, but are solely the result of the underlying growth mechanism, more specifically to the high susceptibility of the (111)B surface to twinning.

This section is adapted with permission from M. Knoedler et al. Observation of Twin-free GaAs Nanowire Growth Using Template-Assisted Selective Epitaxy. Cryst. Growth Des., 2017, 17 (12), pp 6297–6302. Copyright (2017) American Chemical Society.

3.3 Study of dislocation cores as mono-dimensional potential channels

As explained in the previous sections, III-V NWs might exhibit superior properties with respect to the thin films counterparts. Thus, their implementation with Si in heterostructures could lead to improved electronic and optoelectronic devices. However, the presence of crystallographic defects (i.e. partial dislocations, stacking faults, etc.) might play a decisive role on the device performance. In order to implement III-V nanowires in state-of-the-art devices, it is crucial to analyze and control the occurrence of all lattice imperfections as they can lead to the formation of electrically active states within the band gap with the consequent reduction of carrier mobility [212,213]. For example, a particular class of steps in twin boundaries has been demonstrated, via DFT, to be nonradiative recombination centers, inducing deleterious effects in GaAsP nanowires [214]. On the other hand, it has been proven that crystallographic defects can also have a beneficial effect on the device properties. DFT calculations performed on II-VI CdTe thin films for solar cells reported the presence of electrically inactive states in defective regions. In particular, a charge transfer between two nearby 90° partial dislocation cores was observed, increasing the separation of the carriers by band bending. This phenomenon should theoretically improve the cell efficiency [215,216]. A first step in evaluating the impact of a particular defect on the device performance is to investigate its exact atomic configuration. For this purpose, TEM provides the optimal lateral spatial resolution to study the structure of nanodevices at the atomic level and has been successfully used over the last decades in the study of semiconducting materials. A correlation with the electronic properties of the defect is achieved by the aid of theoretical modeling and ab initio methods.

In this work, we used aberration-corrected STEM and EDX spectroscopy to characterize two stair-rod dislocation cores formed at the intersection of three intrinsic stacking faults in a GaAs nanowire. Based on the experimental observations, a 3D atomic model was developed and used to perform DFT calculations. Our simulations reveal the presence of quasi-sp^2 hybrid orbitals at the two defect cores and the presence of highly localized projected density of states (PDOS) shifting along the stacking fault from the valence band in the gallium core to the conduction band in the arsenic core. This confirms the antithetical nature of these two types of defects, suggesting for this particular case the creation of parallel localized potential paths along the nanowire.

Figure 3.9a shows a low-magnification HAADF-STEM micrograph of a GaAs nanowire front section projected along the [110] zone axis. This front section exhibits an average width and height of 100 and 38 nm, respectively. Unless otherwise specified, the same orientation and zone axis of the nanowire is maintained for all subsequent micrographs and models. An atomically resolved image of the inset marked with a white square in Figure 3.9a is displayed in Figure 3.9b.

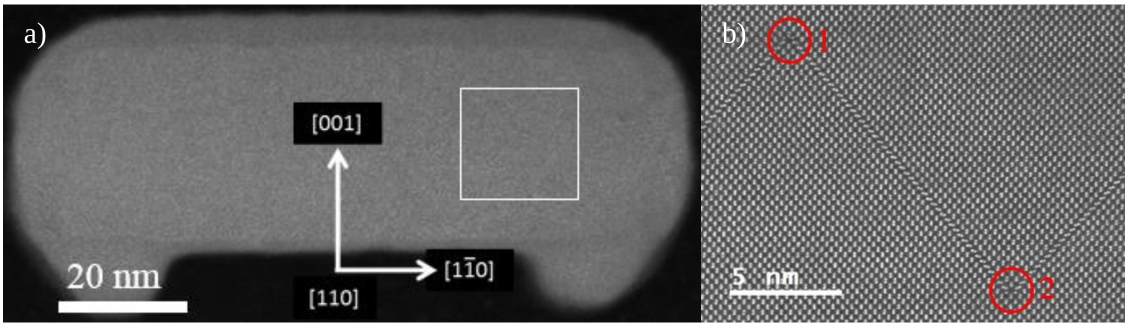

Figure 3.9 – HAADF-STEM micrographs, recorded along the [110] zone axis, showing (a) the front section of the nanowire and (b) an enlarged view of the white square indicated in panel (a). The intrinsic stacking faults intersecting at 70.5° are visible as v-shaped planar defects. The stair-rod dislocations at the vertexes are highlighted with red circles. The two cores are ∼15nm apart.

Three intrinsic stacking faults on different {111} glide planes intersect at an acute angle of 70.5° and create the dislocation cores highlighted with two red circles, labeled as 1 and 2. These two cores, connected via an intrinsic stacking fault, are about 15 nm apart and are expected to propagate along the whole length of the nanowire. The dumbbell atomic columns in the intrinsic stacking faults exhibit the typical change in orientation due to the removal of one close-packed plane from the perfect zinc-blende crystal structure. The Burgers circuits performed on both cores were used to determine the Burgers vectors of the dislocations. The identification of the Burgers vectors of a stair-rod dislocation is obtained by subtracting the vectors of two circuits; the first circuit runs around one stacking fault and the second one around both the second stacking fault and the stair-rod dislocation, considering the crystal unfaulted at the position of the first stacking fault. A detailed analysis of the Burgers vectors performed on both dislocation cores is shown in Figure 3.10(a, b).

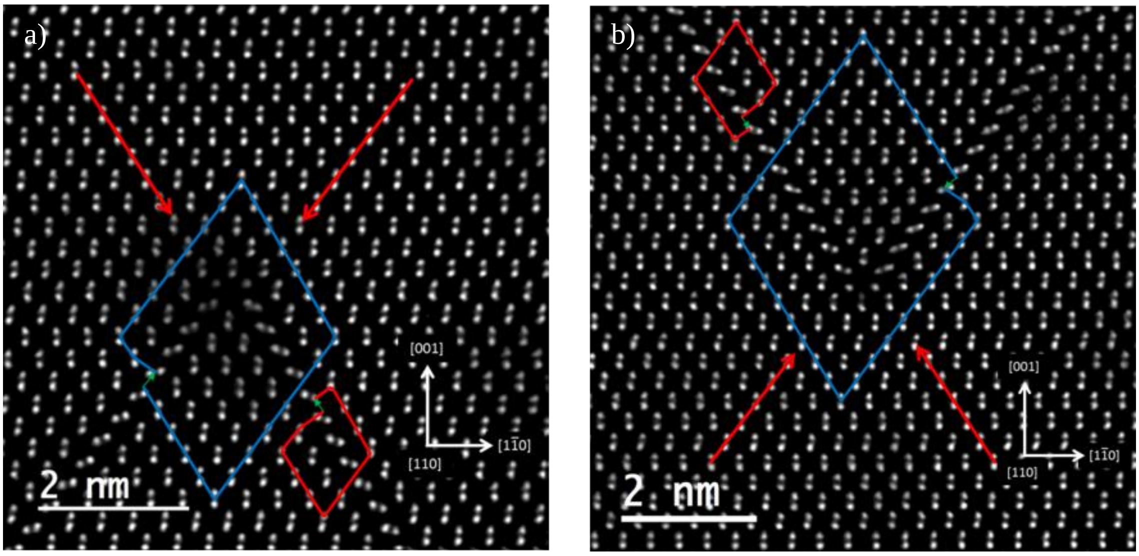

Figure 3.10 – Finish-to-start clockwise Burgers circuits of the two stair-rod dislocations formed by the intersection of intrinsic stacking faults at 70.5° forming v-shaped defects. Both cores are obtained by the interaction of two 30° Shockley partial dislocations with the half-planes indicated by the red arrows. In the first case (a), the Burgers vectors are $\vec{b}$=1/6[211] and $\vec{b}$=1/6 [$\overline{121}$] (highlighted with the green arrows). The total Burgers vector is equal to $\vec{b}$=1/6[1$\bar{1}$0]. In the second case (b), the partial dislocations have Burgers vectors equal to $\vec{b}$ =1/6[$\overline{21}$1] and $\vec{b}$=1/6[12$\bar{1}$]. The total Burgers vector is $\vec{b}$=1/6[$\bar{1}$10]. In both cases an energy reduction ($a^2/3 > a^2/6$) takes place.

In this case, the cores are formed by the interaction of 30° Shockley partial dislocations annihilating each other in two different stair-rod dislocations. Their interaction results in an energy reduction. This particular type of stair-rod dislocation was previously reported in nanostructured metals and semiconductors [217,218] and is commonly observed in the GaAs nanowires grown in the planar SiO_2 templates investigated here. Stair-rod dislocations are characterized by the presence of single unpaired atomic columns [218], clearly visible in Figure 3.11(a, b), where the two dislocation cores, marked as 1 and 2 in Figure 3.9b, are illustrated at higher magnification. The mirrored symmetry between the two structures with the unpaired atomic columns (marked with white circles) located on different lattice sites is distinctly visible. Due to the small atomic number difference between Ga (Z = 31) and As (Z = 33), the Z^2 contrast intensity difference, usually used to recognize atomic species in HAADF micrographs, was not significant enough to safely determine the nature of the single elements. For this reason, atomic-scale EDX chemical maps were recorded in the red dashed area of the two cores. As illustrated in Figure 3.11c, the first core exhibits Ga single-atomic columns, while Figure 3.11d shows As single-atomic columns for the second core, where gallium and arsenic atoms are colored in blue and green, respectively.

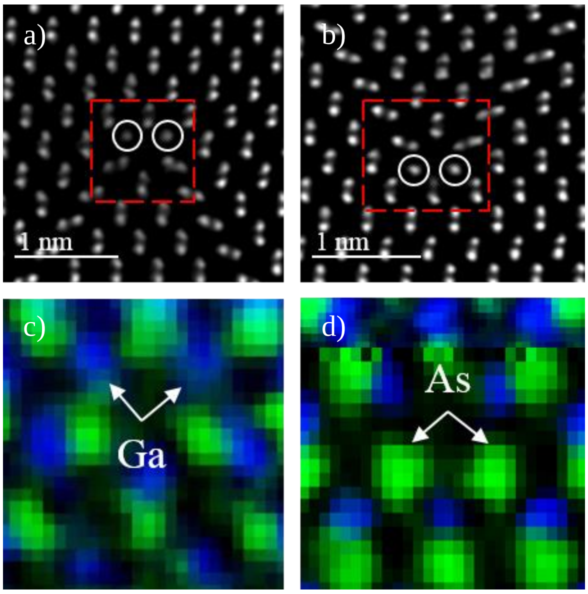

Figure 3.11 – HAADF-STEM atomically resolved images of the first (a) and second (b) dislocation cores. (c, d) Atomic-scale EDX chemical maps corresponding to the red dashed area in panels (a) and (b), respectively. The nature of the unpaired single-atomic columns, i.e., gallium (blue) for core 1 and arsenic (green) for core 2, is distinctly revealed.

Subsequently, 3D atomic models of the dislocation cores were created with the RHODIUS software and used as input for the DFT calculations in order to study the effect they might induce on the band gap and on its electronic structure. DFT calculations were performed within the Gaussian plane-wave method as implemented in the CP2K package with DZVP basis sets for the representation of Kohn-Sham orbitals, with plane-wave cutoff for the charge density of 600 Ry. An initial geometry optimization was performed using the PBE-GGA exchange-correlation functional. This, as it is well known, fails, however, to determine the band gap accurately [184,192]; therefore, single-point calculations were performed using the hybrid functional developed by HSE06, with the exchange screening parameter ω set to 0.11 as recommended in literature [193]. To speed up the calculations, the auxiliary density matrix method with FIT6 auxiliary basis sets was employed. Maximally localized Wannier functions were extracted using CP2K. In order to investigate the effect of the stair-rod defects on the electronic properties of GaAs, DFT calculations were performed on two different models. A 6 × 6 × 6 supercell (corresponding to 16.96 Å in each direction) with 1728 atoms was adopted for the bulk structure, while the defective area was incorporated in a supercell with 924 atoms consisting of 12 × 12 × 2 unit cells. After properly relaxing the structure, the models were imported in STEM_CELL and used to simulate HAADF images. Strain mapping was performed by the use of GPA within the FRWR plugin in order to verify the validity of the model (Figure 3.13(b, c)). Subsequently, the GPA maps of the modeled structure were compared with the experimental ones (Figure 3.12(b, c)). Concordantly, both experimental and simulated data show quantitatively comparable strain and rotational maps at the intrinsic stacking faults with no long-range strain field contributions stemming from the dislocation cores. This confirms the structural validity of the adopted DFT model.

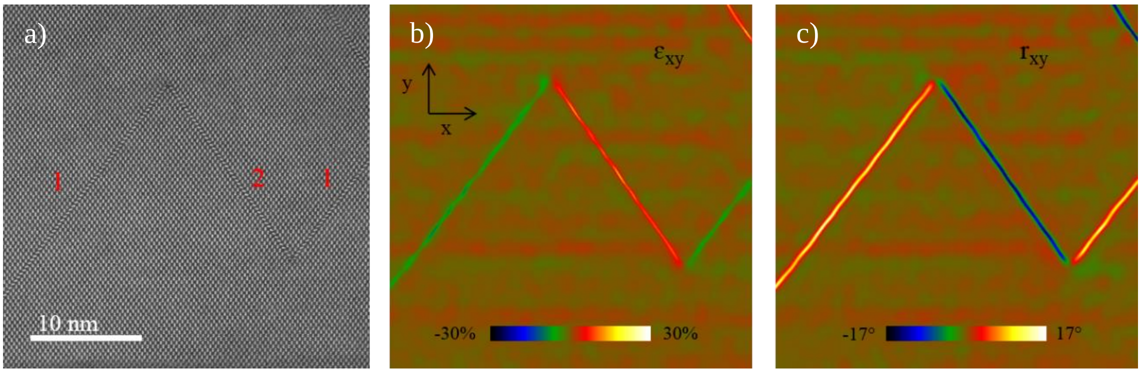

Figure 3.12 – (a) HAADF-STEM micrograph showing the three different intrinsic stacking faults, labeled with 1 and 2 depending on the glide plane, merging together to form two distinct stair-rod dislocations. Panels (b) and (c) illustrate the ε_{xy} strain and the rotational r_{xy} maps, respectively. The lattice deformation was determined relative to an internal reference lattice selected at an area close to the upper stair-rod dislocation. While the detected strains and rotations are attributable to the intrinsic stacking faults, no long-range strain fields are detected at the vicinity of the dislocation cores.

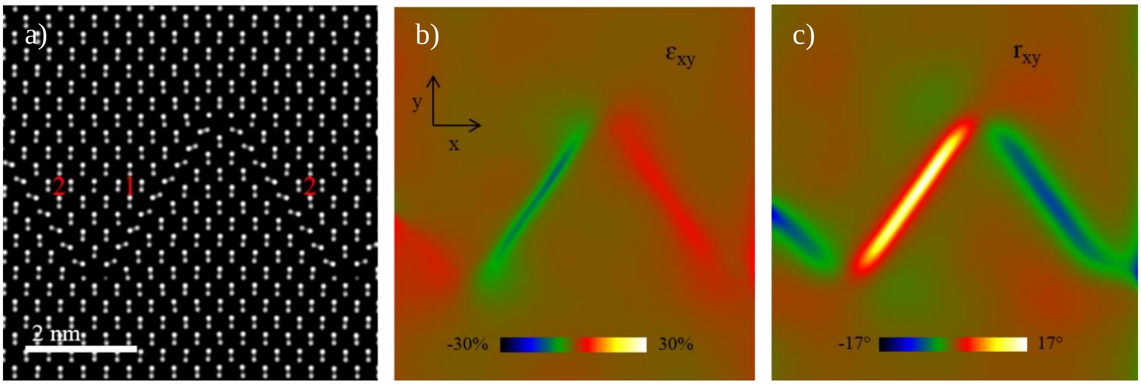

Figure 3.13 – (a) HAADF-STEM simulated micrograph obtained from the relaxed model. As in the previous case, the intrinsic stacking faults creating the dislocation cores are labeled with 1 and 2 depending on the glide plane. (b, c) GPA maps (obtained using the same parameters used for the experimental data) of the modeled structure reproducing the ε_{xy} strain and rotational r_{xy} magnitude. Also in this case, no strain fields are detected in the proximity of the dislocation cores; only the planar defects contribute to the strains and rotations. The similarity of these results with the experimental ones of Figure 3.12, confirm the structural validity of the model employed to perform the DFT calculations.

Figures 3.14(a, b) show the bulk and defective supercells simulated with DFT to investigate the effect induced by the defects on the GaAs electronic properties. Both structures were relaxed using the PBE functional until the force acting on each atom was less than 0.01 eV/Å. The PBE band gap of the bulk GaAs was 0.53 eV, highly underestimated with respect to the 1.43 eV experimentally reported in the literature [219] with a difference of 63%. A single-point calculation with hybrid functional HSE06 was then performed to correct the error, and a band gap of∼1.14 eV with a difference of 21% was obtained. This is still underestimated but the value is now closer to the literature. The PDOS for the bulk structure is shown in Figure 3.14c. Here and in the other PDOS plots the energy zero is set to the Fermi level, and the projections are normalized to the number of atoms involved. The majority of valence states are equally contributed by both Ga and As atoms, with a signature of empty antibonding states rising at +1.14 eV. This is visible in the inset in Figure 3.14c. Note here that the lowest unoccupied molecular orbital (LUMO) peak appears isolated from the conduction band, which is in contrast with calculations conducted with a large number of k points (corresponding to a much larger supercell in our real-space representation). However, the presence of such an undesired feature at the bottom of the conduction band can be due to the finite system-size effects [220]. A similar effect has also been reported for GaN in a study by Meng et al. [221]. Figure 3.14c, supporting this explanation, shows the increase in the density of states (with unchanged band gap) near the conduction band for bulk GaAs with two different supercell sizes. We also verified that the character of the first unoccupied states remains unchanged by increasing the system size. The majority of the unoccupied states contribute above +2.0 eV with a slightly higher intensity from the Ga atoms.

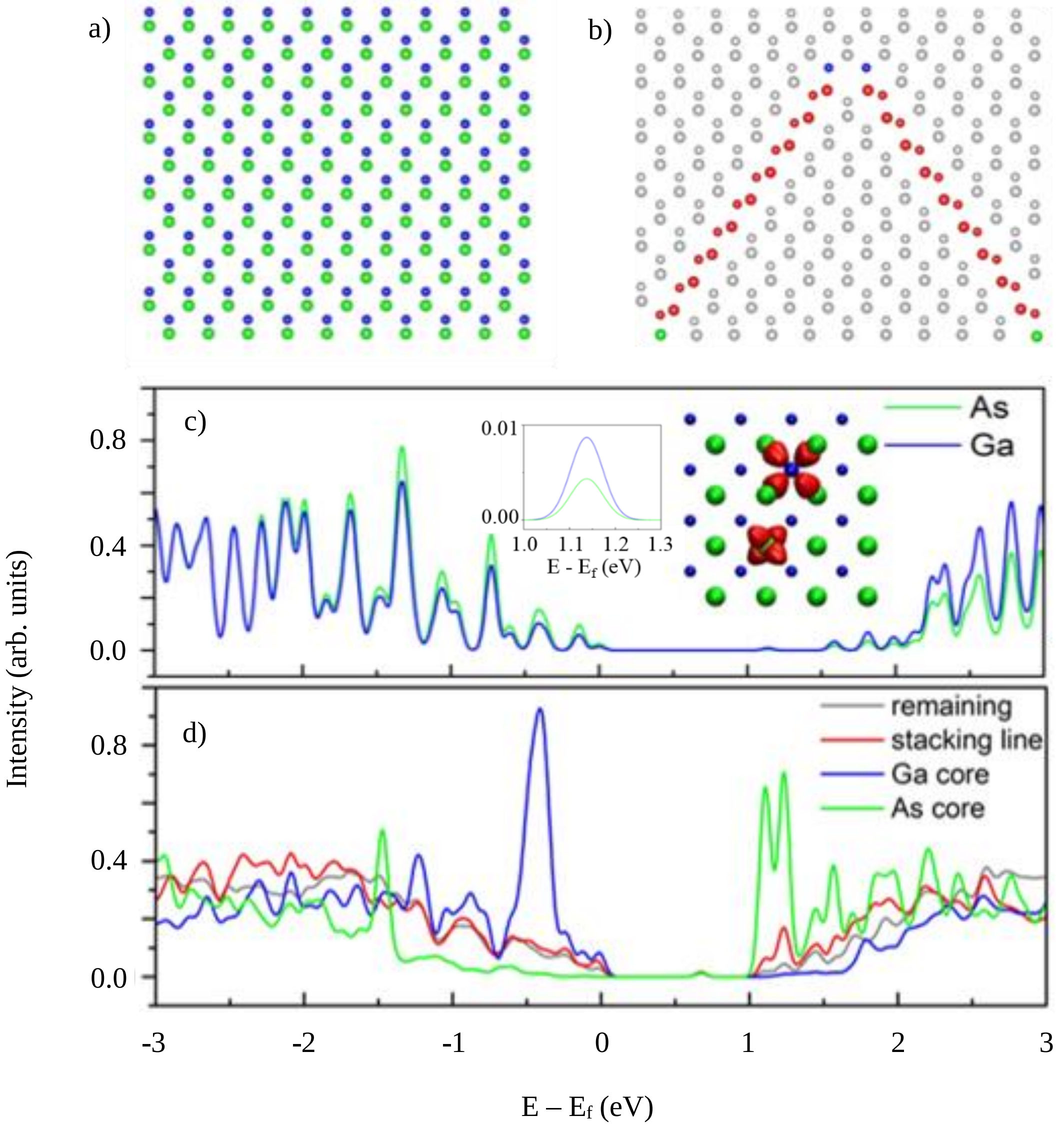

Figure 3.14 – (a) Bulk structure model of GaAs and (c) associated PDOS plot. Gallium (blue) and arsenic (green) states equally contribute along the whole energy range with a slight difference for the unoccupied states above 2.0 eV only. The first localized state is observed at ∼1.14 eV and it is shown in detail in the inset with an energy range between 1.0 and 1.3 eV. The orbital simulation represented in panel (c) illustrates, along a different zone axis, the Wannier sp^3 orbitals present around the Ga and As atoms. (b) Model used to investigate the DOS projected on the Ga core (blue), As core (green), entire stacking fault (red), and remaining crystal (gray) atoms. The associated PDOS plot (d) shows, with the same color codes, the reduction in energy gap and the presence of valence and conduction band states. All plots are normalized to the involved number of atoms in the projection.

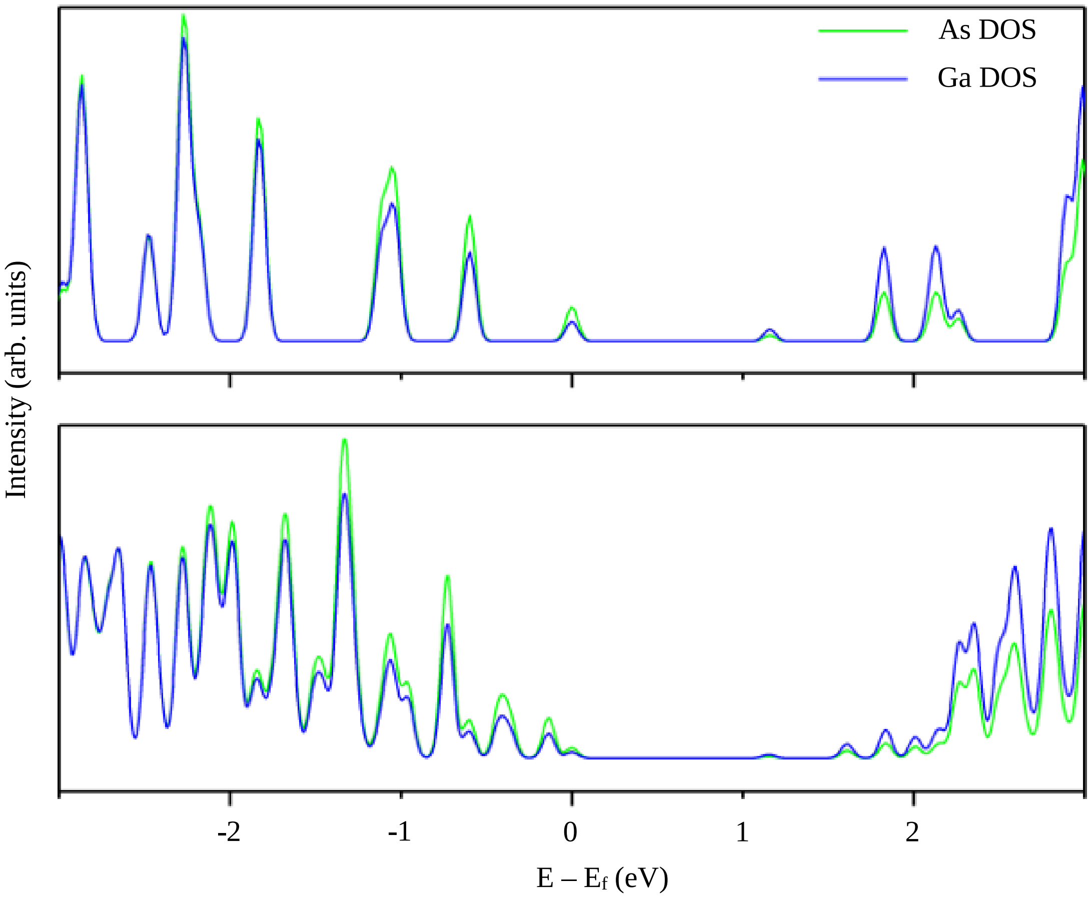

Figure 3.15 – Projected density of states (PDOS) for bulk GaAs using the HSE06 functional for different supercell sizes: top (16.96 Å, 16.96 Å, 16.96 Å) and bottom (33.92 Å, 33.92 Å, 33.92 Å). Green and blue represent the projection on As and Ga atoms, respectively.

The bonding hybridization simulation (Wannier localization) for the defect-free bulk is shown in the inset of Figure 3.14c. The model is here oriented along the [100] zone axis to better exhibit the Wannier orbitals geometry. As expected, four different sp^3 hybrid orbitals connecting the Ga atom to the neighboring As atoms and separated by 109.5° are obtained. The same hybridization is also visible for the As atom connected with the four Ga atoms.

The defects revealed by the experiment are then inserted in the structure. The distance between the two dislocations in the modeled defective structure is not equal to the experimental observations due to the complexity to perform the calculations on such big crystal. For this reason, the distance in the simulated model is around 1/3 of the experimental one. Figure 3.14b illustrates how the defect model is divided with different colors into four parts; they correspond to the As core (green), Ga core (blue), intrinsic stacking faults (red), and the remaining atoms in the bulk (gray). The HSE06 calculated band gap, previously observed at +1.14 eV for the bulk structure, decreases to + 0.54 eV, as illustrated in Figure 3.14d. The peaks, present in all the areas taken into consideration in the structure, suggests an overall influence by the dislocation cores on the electron cloud of the entire modeled crystal. A comparison of the PDOS contributions coming from the Ga and As dislocation core atoms is also presented in Figure 3.14d. Ga core atoms (blue line) show a major contribution in the upper part of the valence band (above −0.7 eV) while the projection on the As core atoms (green line) has a predominant distribution in the bottom of the conduction band states with multiple peaks appearing between 0.54 and 1.25 eV. Major contributions in this interval are due to the As core atoms followed by the contributions from the atoms on the intrinsic stacking faults (red) and then from the remaining atoms (gray line). For the Ga core atoms, the effective contribution to the empty states starts only after +1.7eV. We interpret the two peaks at the edges of the valence and conduction bands (blue and green lines in Figure 3.14d) as signatures of a band localized along the defect channels (see Figure 3.17, explained below). Our supercell representation allows us to sample the band only at the gamma point. As in the defect-free bulk model, the bonding orbitals were simulated in correspondence of the two dislocation cores. The results are illustrated in Figures 3.16(a, b) for the Ga and As single atoms, respectively. The dislocation cores develop a configuration in between *sp*^{3} and *sp*^{2} where three hybrid orbitals separated by 120° are obtained. The presence of an unpaired orbital generates a distortion in the three orbitals geometry not allowing the standard *sp*^{2} planar configuration. This can be connected to the difference in PDOS on the valence and conduction band present in the single Ga and As atoms.

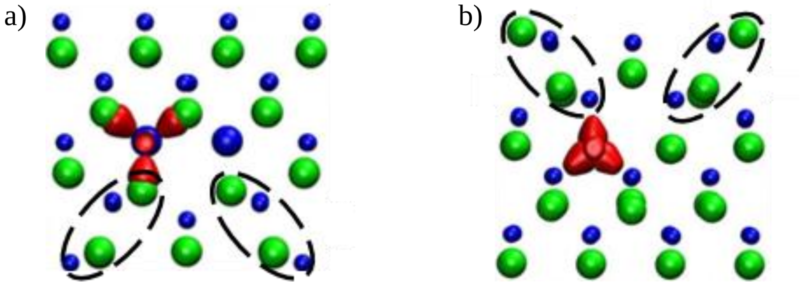

Figure 3.16 – The Wannier orbitals (in red) showing the quasi-*sp*^{2} geometry are illustrated in panels (a) and (b) for the Ga and As dislocation core, respectively. The black dashed ellipses highlight the position of the stacking faults.

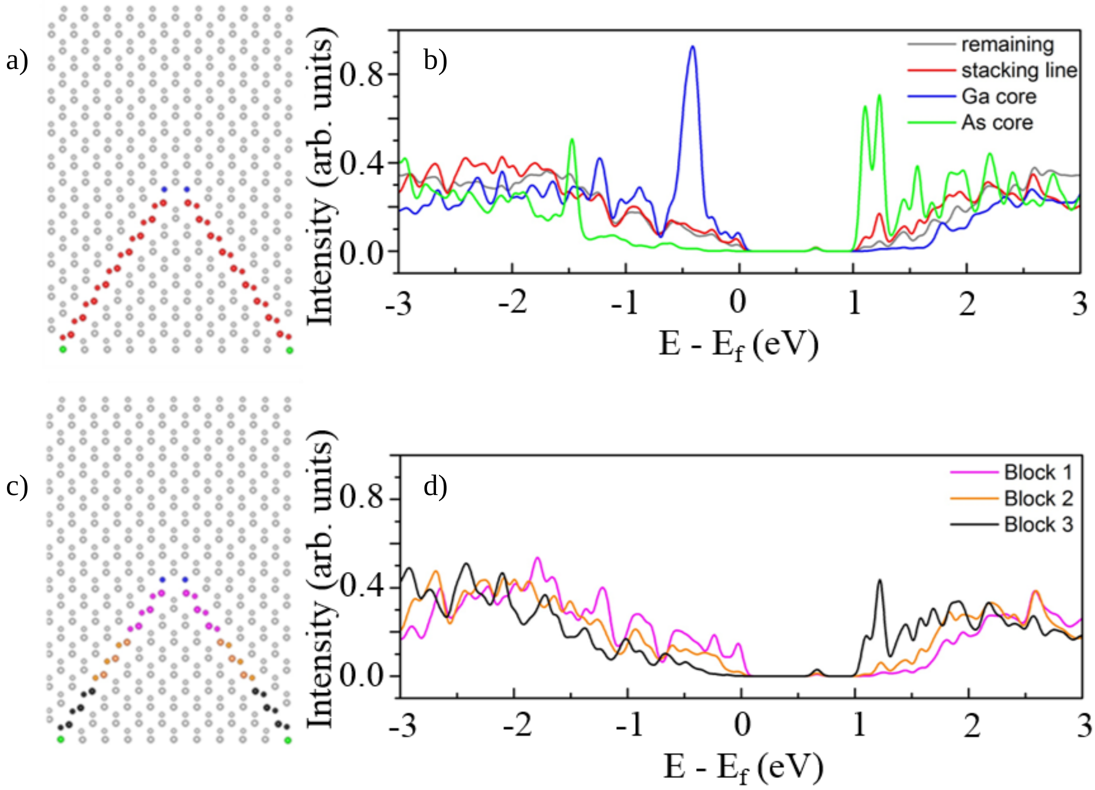

Figure 3.17 – (a) Model of the defective structure built with a 12 × 12 × 2 supercell and used to investigate (b) the DOS projected on the Ga core (blue), As core (green), entire stacking fault (red), and remaining crystal (gray) atoms. (c), (d) The analysis is also performed by further dividing the intrinsic stacking faults in three distinct segments. The segments and the associated PDOS are shown with the same color codes.

Similarly, in Figures 3.17(c, d), the analysis is performed by further dividing the intrinsic stacking fault into three parts: Ga core proximity (pink block 1), intermediate stacking faults (orange block 2), and As core proximity (black block 3). As done previously, the single-point calculation with HSE06 functional was performed for the defective structure. The PDOS distribution of block 1 (pink line) is very similar to that of the Ga core atoms where there is a minimum contribution in the conduction band after +1.7 eV and a significant increase in the states below the Fermi level. Similarly, block 3 (black line) follows the trend of the As core atoms where the majority of unoccupied states are concentrated at +1.0 eV and almost zero states in the valence band. Atoms in block 2 (orange line) have a distribution in between the As and Ga core PDOS plots. In fact, both conduction and valence band states are visible with a lower intensity with respect to both block 1 and 3. This effect is probably emphasized as a consequence of the shorter distance with respect to the experimental structure, but the same qualitative behavior is expected.

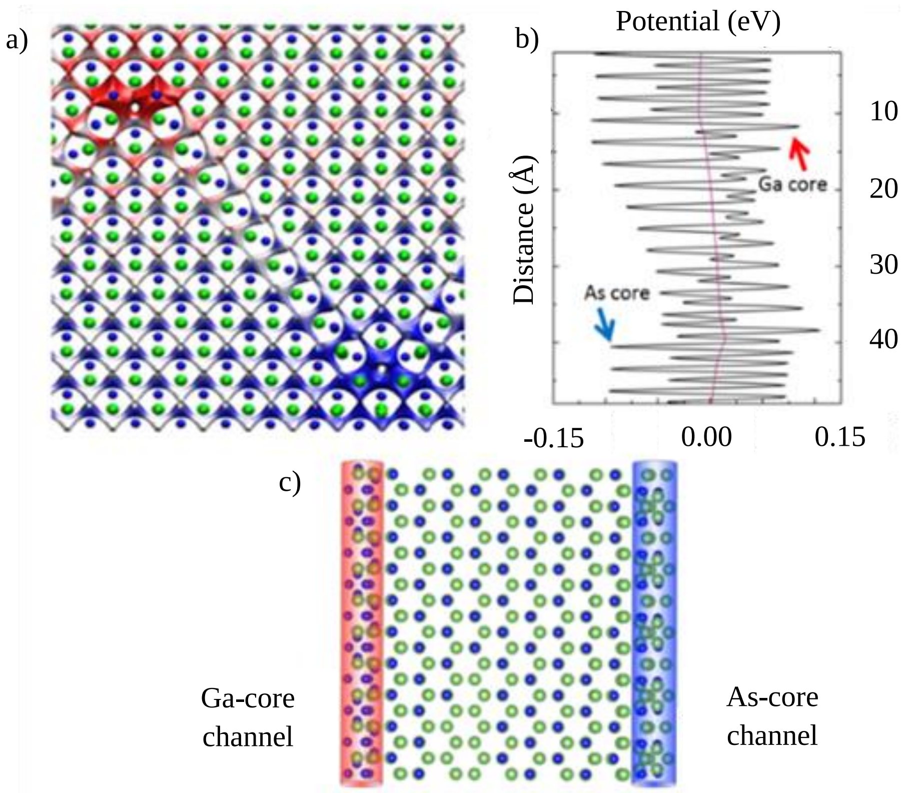

Figure 3.18 – (a) Electron density map with an isosurface value of 4.1 × 10−3 e/ Å and potential color-gradient scale in red (max) 3 and blue (min) along the [110] zone axis. (b) Distribution of the electrostatic potential in the [001] direction along the stacking fault with average potential energy represented with a magenta line. (c) Graphical representation, along the [$1\bar{1}1$] zone axis perpendicular to the intrinsic stacking fault showing the charge nanochannels generated by the two dislocations.

Furthermore, an analysis of the electrostatic potential is performed in Figure 3.18a where the electron density map of the two dislocation cores with potential color scale is shown. Figure 3.18b represents the electrostatic energy along the stacking fault line with the As core showing the highest potential energy acting as LUMO and the Ga core with the lowest potential energy acting as highest occupied molecular orbital (HOMO). This investigation clearly shows the formation of an electric field between the Ga core and As core confirming the role of the stair-rod dislocation cores as charge wires. This could lead to an improved carrier separation upon doping and a reduction in detrimental recombination. Since the dislocation cores in both cases are assumed to propagate along the whole length of the nanowire, the highly localized nature of the density of states can induce the formation of charge nanochannels, as shown in Figure 3.18c and 3.19, where we plot the integrated charge (hole) density around the PDOS peaks at the top (bottom) end of the valence (conduction) band (up to the Fermi level in both cases). This suggests the possibility of facilitated the transport of electrons and holes for the Ga and As core, respectively. In this case, since the localized channel states do not close the band gap, doping of the material would be necessary in order to accommodate free carriers in the channels. This phenomenon (but with the defect band developing within the gap) was recently studied for a different class of materials; i.e. a transition-metal dichalcogenide [222]. Even though the electronic states in [219] are considerably different to those in GaAs, the simulated physical behaviors are comparable. This could be further analyzed and exploited in the future for the realization of innovative devices where the combination of different growth conditions and materials (including doping) can lead to the formation of preferential paths for improved mono-dimensional carrier transport.

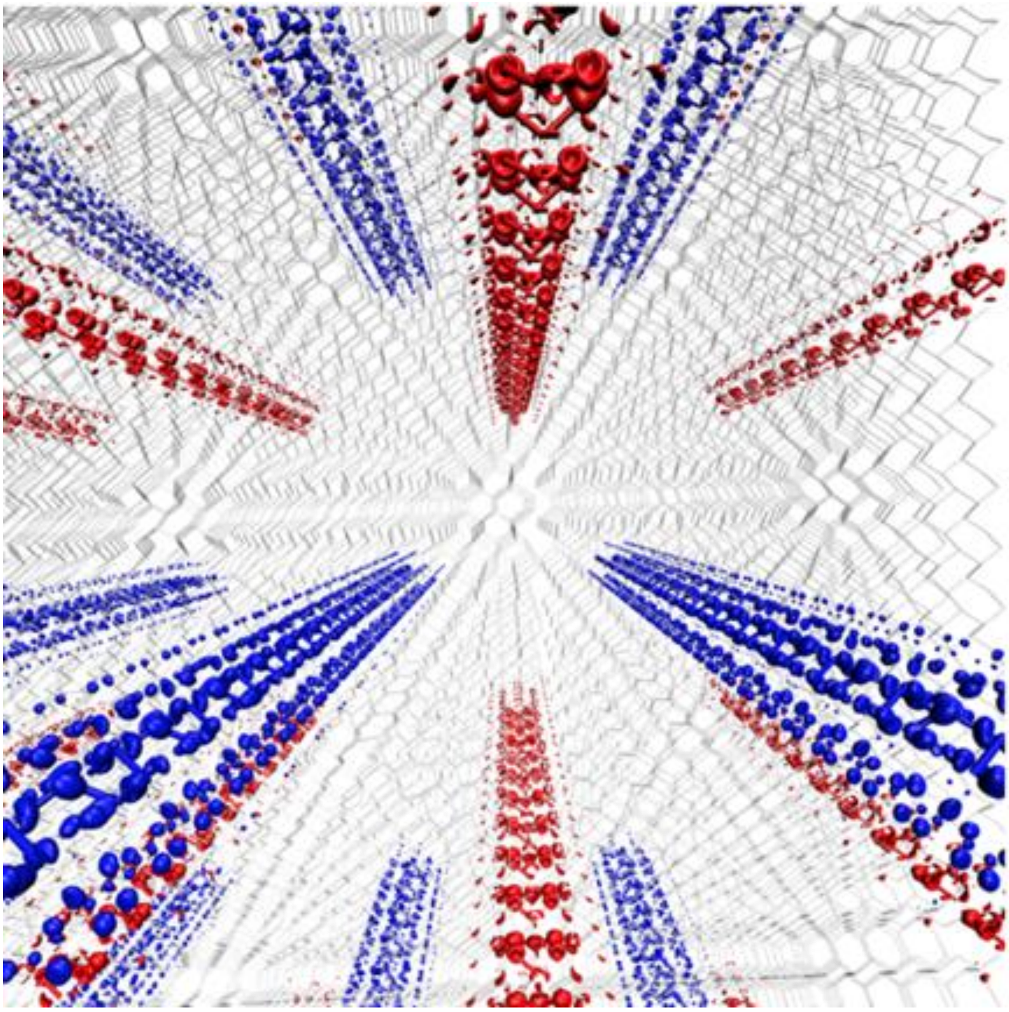

Figure 3.19 – Isosurface (0.012 a.u.) of the integrated charge in the energy interval corresponding to the localized peaks for electrons (red) and holes (blue) in the density of states (“Ga core” and “As core” in Figure 3.14d), forming the one-dimensional charge channels.

In conclusion, aberration-corrected STEM has been used to assess the atomic structure of two stair-rod dislocations obtained by merging multiple stacking faults in v-shaped defects. Elemental EDX mapping has been employed to unambiguously identify the nature of the single-atomic columns at the dislocation cores, revealing that they consist of either entirely gallium or arsenic. Their effect on the electronic properties has been investigated by means of DFT calculations showing a reduced energy gap with respect to the bulk material. Furthermore, the development of charge channels along the defect channels, with a corresponding strong electric field between the channels, is probably attributable to the unpaired *p* orbitals in the quasi-sp^2 bonding configuration of the single-atomic columns. These results suggest the possibility to obtain strongly localized potential paths within the nanowire which might host free carriers upon appropriate doping and improve the carrier separation along the two dislocation cores.

This section is adapted with permission from N. Bologna et al. Stair-rod dislocation cores acting as one-dimensional charge channels in GaAs nanowires. Phys. Rev. Materials 2, 014603 (2018). Copyright (2018) American Physical Society.

4 Doping investigation of vertical nanowires for PV applications

Today, Si is the most used material in photovoltaics, with the maximum conversion efficiency getting very close to the Shockley–Queisser limit for single-junction devices. Integrating Si with higher band-gap ternary III-V absorbers is the path to increase the conversion efficiency. Here, we report on the first monolithic integration of $Ga_xIn_{(1-x)}P$ vertical nanowires, and the associated p-n junctions, on Si by the Au-free TASE method. We demonstrate that TASE allows for a high chemical homogeneity of ternary alloys through the nanowires. We then show the influence of doping on the chemical composition and crystal phase, the latter previously attributed to the role of the contact angle in the liquid phase in the vapor-liquid-solid technique. Finally, the emission of the p-n junction is investigated, revealing a shift in the energy of the intraband levels due to the incorporation of dopants. These results clarify some open questions on the effects of doping on ternary III-V nanowire growth and provide the path toward their integration on the Si platform in order to apply them in next-generation of photovoltaic and optoelectronic devices.

4.1 Nanowires growth

The nanostructures were grown in nanotube templates by metal–organic chemical vapor deposition on Si (111) wafers at a temperature of 550 °C. The vertical templates were fabricated with the following procedure. A sacrificial amorphous α-Si layer was sputtered on the wafer's surface. The thickness of the α-Si layer determines the height of the templates, while the diameter (~150 nm) and position of the templates are defined by patterning hydrogen silsesquioxane dots by electron beam lithography. Inductively coupled plasma reactive-ion etching using HBr/O_2 was employed to etch out vertical Si NWs. SiO_2 was then subsequently deposited on the Si NWs by plasma-enhanced chemical vapor deposition at 400 °C. To empty the nanotube templates and to obtain a pristine (111)-terminated crystalline Si surface at the bottom, a patterned resist mask was deposited to protect the substrate, and a 25% tetramethylammonium hydroxide solution was used to selectively etch away the Si sacrificial NWs. The growth of the $Ga_xIn_{(1-x)}P$ NWs was carried out using trimethylindium (TMIn),trimethylgallium (TMGa), and tertiarybutylphosphine with a V/III ratio of 310. A group III molar flux ratio of TMGa/(TMGa + TMIn) of 0.6−0.25 was used. The doped NWs were grown with the same conditions but with a V/III ratio of 42. The n-type doping, induced in the first half of the NWs, was obtained by using disilane (Si_2H_6) with a molar flux ratio Si/(TMIn + TMGa) of 0.0023, while for the p-type doping, induced in the second half of the NWs, diethylzinc (DEZn) was employed with a ratio DEZn/(TMIn + TMGa) of 3 resulting in doping concentrations above 1.0×10^{18} cm^{-3} for both sections [223]. In general, the observed growth rate was about 10 nm/min for the undoped and doped samples.

Concerning the samples used for the off-axis holography, the GaAs NWs were grown in the SiO_2 templates on Si(111) using TMGa and TBAs. Different combinations of dopant were used (n-p, i-n-i) and their growth procedures are the followings. The p-n NW was obtained by introducing as in the previous experiment Zn and Si as dopants, at a V/III ratio of 40 and 600 °C. The growth was performed for 10 minutes in the p-segment and 30 minutes in the n segment. The expected depletion region should be around 60-70 nm. The i-n-i NW was grown, as it will be explained in section 4.3, by a double growth method, i.e. TASE and SAG. The first TASE section, which included the doping atoms, was grown at 600 °C with a V/III ratio of 40. Then, Zn atoms were introduced for 10 minutes, before switching the growth to SAG for another 20 minutes with no dopants.

4.2 Dopant-induced modifications of $Ga_xIn_{(1-x)}P$ p-n junctions monolithically integrated on Si (111)

To the best of our knowledge, catalyst-free and high-quality growth of doped $Ga_xIn_{(1-x)}P$ NWs on (111)-oriented Si substrates has not been achieved, mainly due to the compositional inhomogeneities occurring during dopant incorporation [224–228]. In addition, it is widely reported that the use of dopants during NW growth, apart from modifying the chemical composition, can also affect in some cases the morphology (i.e. NW diameter) and the crystal structure (e.g. crystal polytypism). For example, Zn doping modifies the wetting angle of the metallic seed particle during NW growth favoring the zinc-blende crystal structure in InP and $Ga_xIn_{(1-x)}P$ NWs [229,230]. On the contrary, the addition of Zn and Sn dopants in GaAs NWs causes either an increase in the wurtzite proportion or no effect at all [231–233]. Moreover, as previously explained, the use of Au nanoparticles as catalyst in the VLS growth might compromise the Si PV cell performance. First attempts to grow $Ga_xIn_{(1-x)}P$ NWs without the use of any catalyst particle were realized by SAG with good control of the NW morphology and composition [60,234], but this work relied on the use of InP substrates. As explained in chapter 1, the TASE technique allows for the growth of shape- and size-controlled nanostructures by means of a Si oxide nanotube template offering a wide growth parameter window (as compared to SAG) and well-defined growth direction. These characteristics render the TASE technique attractive to obtain NW structures on Si for solar cell applications. In the present work, we demonstrate the first successful monolithic integration of $Ga_xIn_{(1-x)}P$ NWs on (111)-oriented Si substrates using TASE. Furthermore, we present a comparative study between intrinsic and doped $Ga_xIn_{(1-x)}P$ NWs including p-n junctions using aberration-corrected HAADF-STEM in combination with EDX spectroscopy and EELS. Thus, the effect of doping on the microstructure and composition of the NWs is revealed. Finally, the optical properties of individual doped NWs are probed by CL spectroscopy.

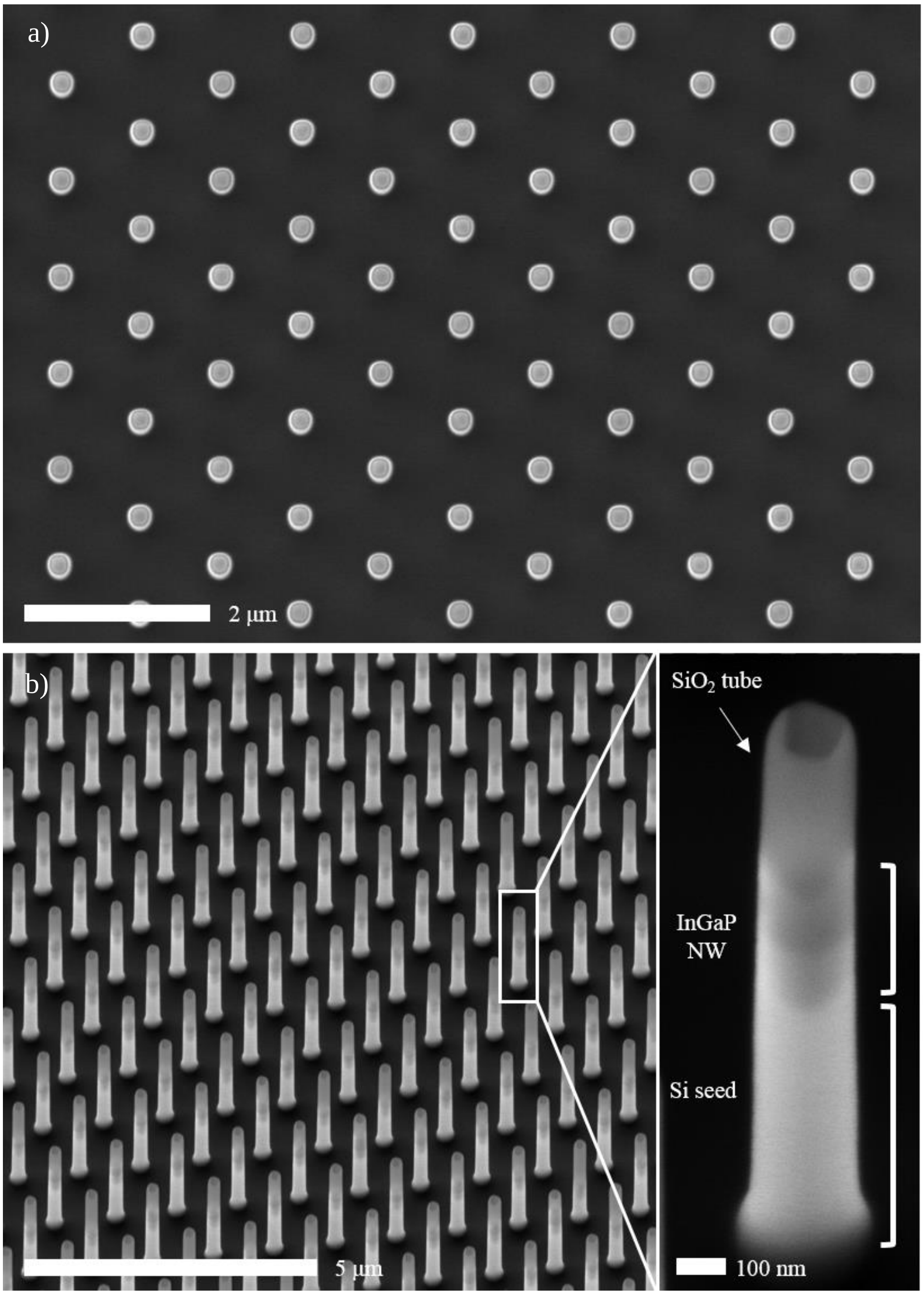

Figure 4.1 – Top (a) and tilted (b) view SEM micrograph of a highly ordered $Ga_xIn_{(1-x)}P$ NW array grown on a Si(111) substrate. A magnified view of a single NW is shown in the right panel. The SiO_2 nanotube template (partially empty), the Si seed, and the $Ga_xIn_{(1-x)}P$ NW are indicated.

Overview SEM images of an array of TASE-grown vertical $Ga_xIn_{(1-x)}P$ NWs on a Si(111) substrate acquired from the top and with an angle are displayed in Figure 4.1(a, b), respectively. The right panel shows a magnified image of a single $Ga_xIn_{(1-x)}P$ NW grown onto the Si seed crystal into the predefined SiO_2 nanotube template. Site-specific TEM lamellae for STEM characterization were prepared by using a FIB instrument. The lift-off process is described in chapter 2.3. A typical undoped NW is shown along the $[\bar{1}10]$ zone axis in the STEM micrograph of Figure 4.2a. On average, these NWs possess a diameter of about 150 nm with a flat front facet and a sharp interface with the Si substrate. Concerning the crystal structure, the zinc-blende type dominates the entire length of the NW with a high density of planar defects (stacking faults and twins) lying on the $(\bar{1}\bar{1}\bar{1})$ plane. This is clearly visible in the atomic-resolution images of Figure 4.2(b, c) obtained at the top (red window in Figure 4.2a) and at the bottom (blue window in Figure 4.2a) of the NW. No difference in the type of planar defects has been observed between the two regions.

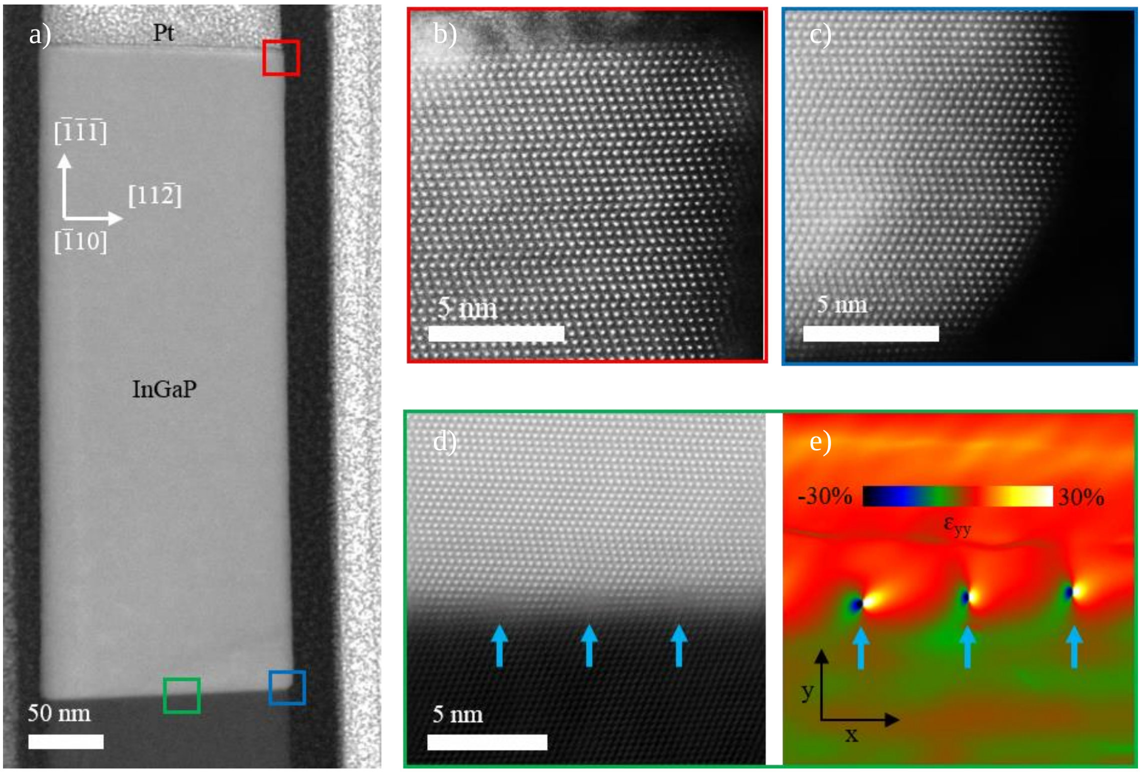

Figure 4.2 – HAADF-STEM overview image showing a typical undoped $Ga_xIn_{(1-x)}P$ NW. Atomic-resolution HAADF-STEM detail of the crystal structure at the top (b, red) and at the bottom (c, blue) of the NW. Both areas exhibit a zinc-blende crystal structure with a high density of planar defects. (d) Magnified image of a region at the $Ga_xIn_{(1-x)}P$/Si interface corresponding to the green square. Three misfit dislocations are marked with blue arrows and appear in panel (e) as butterfly-like features in the out-of-plane (ε_{yy}) strain map obtained by GPA.

A detailed analysis of the interface with the Si seed was performed by GPA in order to detect possible defect formation due to the lattice mismatch. Figure 4.2d shows a magnified view of the green squared region highlighted in Figure 4.2a. The corresponding ε_{yy} strain map along the out-of-plane direction is displayed in Figure 4.2e. Here, the $Ga_xIn_{(1-x)}P$ NW appears to have a positive deformation (red color) as the lattice parameter is larger than the Si used as reference, which is a_{Si} = 5.431 Å. The value for the strain measured at the $Ga_xIn_{(1-x)}P$ area is (6.5 ± 0.3)%, resulting in a lattice constant of (5.78 ± 0.1) Å. Three blue arrows in the HAADF image indicate the regions of the interface exhibiting a lower contrast due to an interruption of the atomic stacking continuity. In the strain map of Figure 4.2e, these regions are clearly recognizable by the three compressive-tensile butterfly-like strain features separated by an average distance of about 4.5 nm. They are interfacial misfit dislocations that, as explained in chapter 1.3, form to release the mismatch strain between both systems. The compositional homogeneity of the undoped NWs was then investigated by STEM-EDX. For this analysis, the NWs were transferred to a holey carbon-coated TEM copper grid by gently rubbing it against the NW array. Thus, gallium contamination due to the FIB sample preparation was avoided. An HAADF-STEM image of a typical undoped NW and the corresponding elemental maps calculated from a EDX spectrum image using the P Kα1, In Lα1, and Ga Kα1 lines are shown in Figure 4.3(a-d). As revealed in Figure 4.3c, d, the composition of the undoped NWs shows some local variations up to 5%. However, the overall composition performed within the same growth run was reasonably homogeneous with very small deviations (< 0.5%) in both the longitudinal and radial directions with In, Ga, and P nearly constant across the entire structures. The compositional line profiles obtained by averaging the integrated intensities over the whole diameter of the NW are given in Figure 4.3e. While small oscillations are perceptible in the indium and gallium line profiles (most likely due to variations in the growth rates of {111}- and {110}-type facets during the growth process), an average $Ga_xIn_{(1-x)}P$ composition with x = 0.25 ± 0.03 can be obtained for the undoped NWs. This corresponds to a lattice constant of (5.77 ± 0.02) Å, leading to a lattice mismatch of (6.1 ± 0.4)% with Si. Similarly, p-n homojunction NWs were also characterized by employing HAADF-STEM and STEM-EDX.

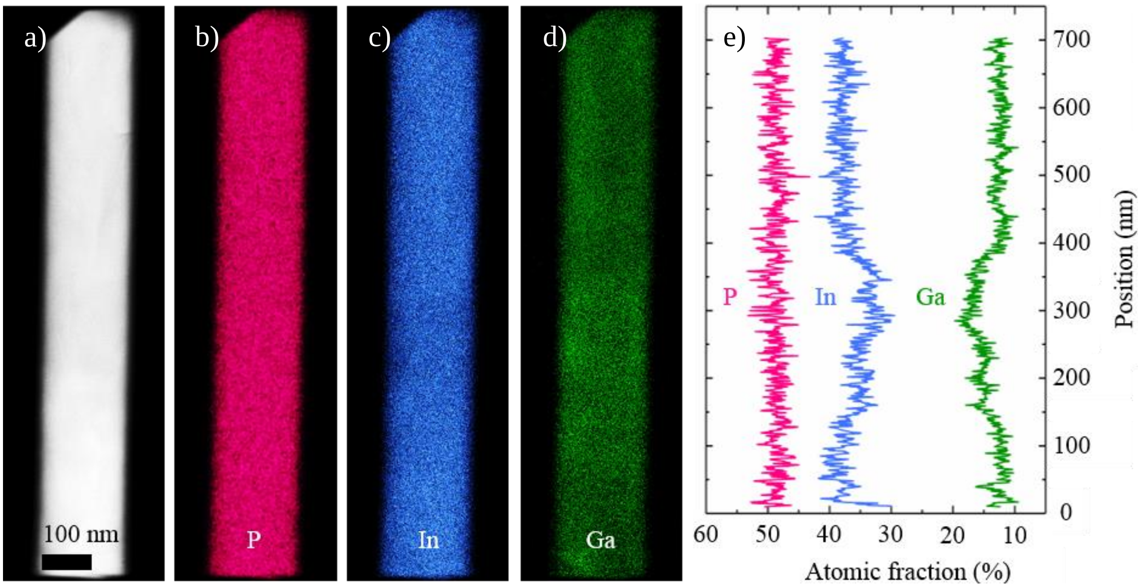

Figure 4.3 – (a) HAADF-STEM image of an undoped NW and the corresponding elemental maps of (b) phosphorous, (c) indium, and (d) gallium obtained from an EDX spectrum image. (e) Compositional line profiles of P, In, and Ga obtained by averaging the integrated intensities over the whole diameter of the NW.

Figure 4.4a shows an overview image of a representative doped NW exhibiting a sharp interface with the Si substrate, comparable to the undoped structures. For this particular NW, the front facet is not regular, probably due to the milling process during the FIB preparation, and therefore no particular faceting can be recognized. For the doped NWs, two features are readily observed: the first one, indicated with a yellow arrow in Figure 4.4a, is a sharp change of contrast along the growth direction arising at about 260 nm from the Si interface, which can be associated with the switch from the n- to the p-region of the NW combined with a change in composition as it will be discussed below. The second feature is highlighted with two white arrows in the upper left area of Figure 4.4a. Two dark stripes propagate from the top of the NW to the left sidewall. The atomically resolved HAADF-STEM image of Figure 4.4c (obtained from the blue squared region in Figure 4.4a) unveils a zinc-blende structure with a high density of twins (about 1twin/nm) lying on the$(\overline{111})$ plane, similar to the undoped structure. This morphology is observed from the interface with the Si until the previously mentioned change in contrast at 260 nm. Then, the upper half of the NW presents also a zincblende structure, but with a much lower density of planar defects (five twins in the entire upper segment) lying on parallel $(1\overline{1}1)$ planes. These twins are visible as darker stripes in the overview image of Figure 4.4a (white arrows) and are highlighted with red dashed lines in the atomically resolved HAADF-STEM image of Figure 4.4b, which corresponds to the red area in panel (a). This change in crystal structure from the bottom to the top of the NW is related to the transition from the n-doped (Si) to the p-doped (Zn) segment. A preferential growth of the zinc-blende crystal structure was previously attributed to a variation in the wetting angle of the gold seed particle caused by the introduction of Zn dopant atoms in NWs grown by VLS [229]. Likewise, changes in the NW diameter were attributed to the seed particle wetting angle. However, our results demonstrate that a change in the crystal structure also occurs when no metal catalyst particle is used for the NW growth. Additionally, as the TASE method employs nanotube templates for the growth of the NWs, the diameter of neither doped nor undoped structures is altered by the introduction of dopants, maintaining the original aspect ratio necessary for high-performance solar cells. Additionally, our observations unveil that the addition of dopant atoms in the NWs affects the density of misfit dislocations at the $Ga_xIn_{(1-x)}P$/Si interface. In the HAADF-STEM image and the corresponding ε_{yy} strain map of Figure 4.4(d,e), respectively, it can be seen that the distance between misfit dislocations is here increased to about 5.5 nm, while the experimentally measured strain difference between the NW and the Si substrate is only ~ (4.5 ± 0.3)%. This value corresponds to a lattice constant of (5.68 ± 0.1) Å, which is smaller than in the undoped structure.

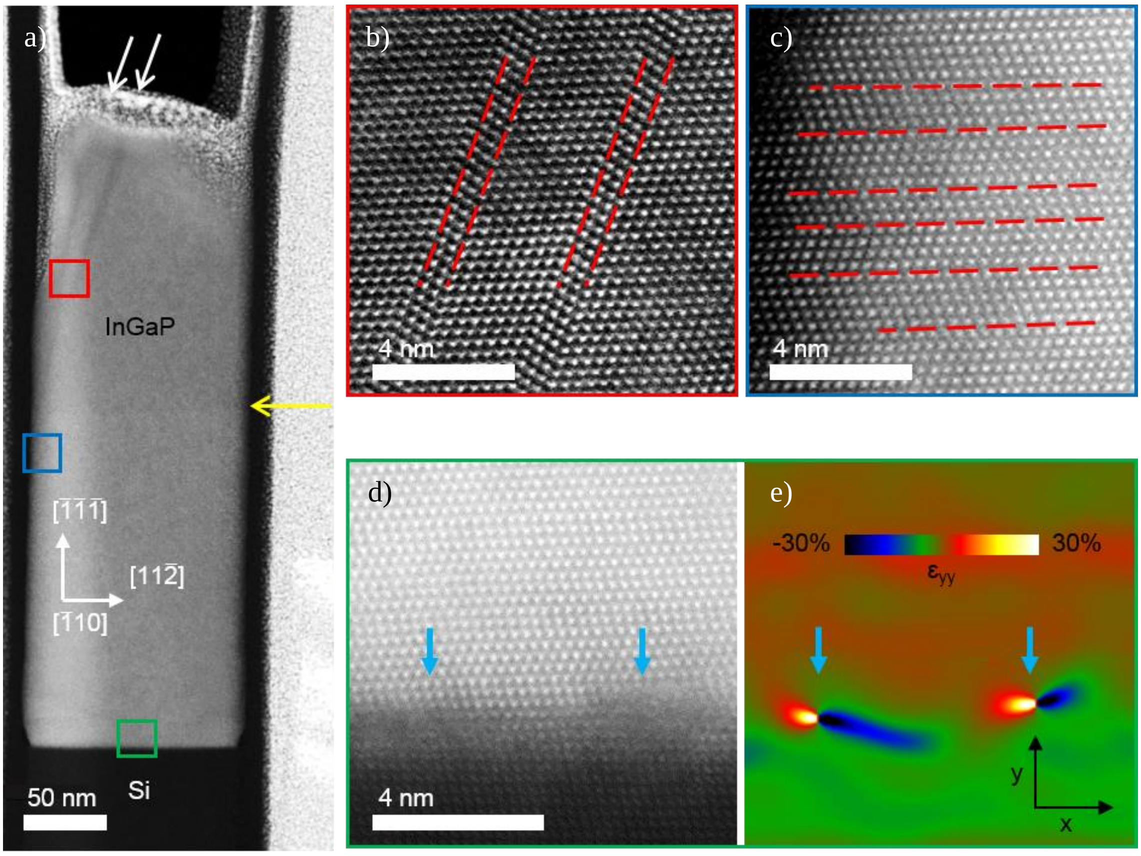

Figure 4.4 – (a) HAADF-STEM overview image showing a representative p–n-doped $Ga_xIn_{(1-x)}P$ NW. Atomic-resolution HAADF-STEM detail of the crystal structure of the top (b, red) and at the bottom segment (c, blue) of the NW. A yellow arrow indicates the transition from the top p doped (Zn) segment and the bottom n-doped (Si) section exhibiting a high density of planar defects (highlighted by red dashed lines). (d) Magnified image of a region at the $Ga_xIn_{(1-x)}P$/Si interface corresponding to the green square. Two misfit dislocations are marked with blue arrows and appear in panel (e) as butterfly-like features in the out-of-plane (ε_{yy}) strain map obtained by GPA.

To confirm these results and to unveil the origin of the sharp contrast change observed at the middle of the doped NWs, we acquired EDX spectrum images of several wires. Similar to the undoped NWs, the sample for EDX analysis was prepared by gently rubbing the TEM grid against the chip's surface. A representative doped NW is shown in Figure 4.5a, while the elemental maps calculated from the EDX spectrum image (P Kα1, In Lα1, and Ga Kα1 lines) are presented in Figure 4.5(b-d). It is evident that the bottom part of the NW contains a higher amount of indium, while the top segment is gallium rich. This effect was further studied on six different doped NWs by recording the amount of indium, gallium, and phosphorus in three different positions along the structures, that is, at 50, 150, and 500 nm from the Si seed. The obtained results are shown in Figure 4.5e, where each data point corresponds to the average value of six wires, and the error bars are given by the calculated standard deviation (±1σ). While the phosphorus is constant along the whole length of all six NWs, the indium and gallium profiles show a drastic change from the bottom to the top of the NW. The region close to the Si seed has an average $Ga_xIn_{(1-x)}P$ composition with $x = 0.33 \pm 0.05$, that is, a lattice constant of (5.73 ± 0.03) Å. This experimental value is, as expected, smaller than the one observed for the undoped NW (5.85 Å), explaining the larger dislocation spacing. Instead, at the upper segment, the trend is reversed, and we find a maximum Ga content with an average $x = 0.55 \pm 0.03$, corresponding to a lattice constant of (5.64 ± 0.01) Å. The change in composition takes place within ∼40 nm at the p-n interface (Figure 4.5f) and results in a lattice mismatch of -1.6%. However, no structural defects are detected at any of the investigated p-n junctions. Finally, although the change from n to p doping is typically observed at about 150 nm from the Si interface (coinciding with a similar concentration of Ga and In), p-n junctions are occasionally detected at a longer distance from the Si interface (as in the NW displayed in Figure 4.4a) due to different growth rates of the n-segments. Our observations concerning the influence of doping on the chemical composition of p-doped $Ga_xIn_{(1-x)}P$ NWs are in agreement with previous works stating that DEZn increases the incorporation of Ga due to the enhanced pyrolysis of the trimethylgallium TMGa-related species [229,235]. Furthermore, our results provide the first experimental evidence that Si doping also boosts the incorporation of Ga in the n-doped section, as compared to the undoped structure, while a high density of stacking faults perpendicular to the growth direction is still present.

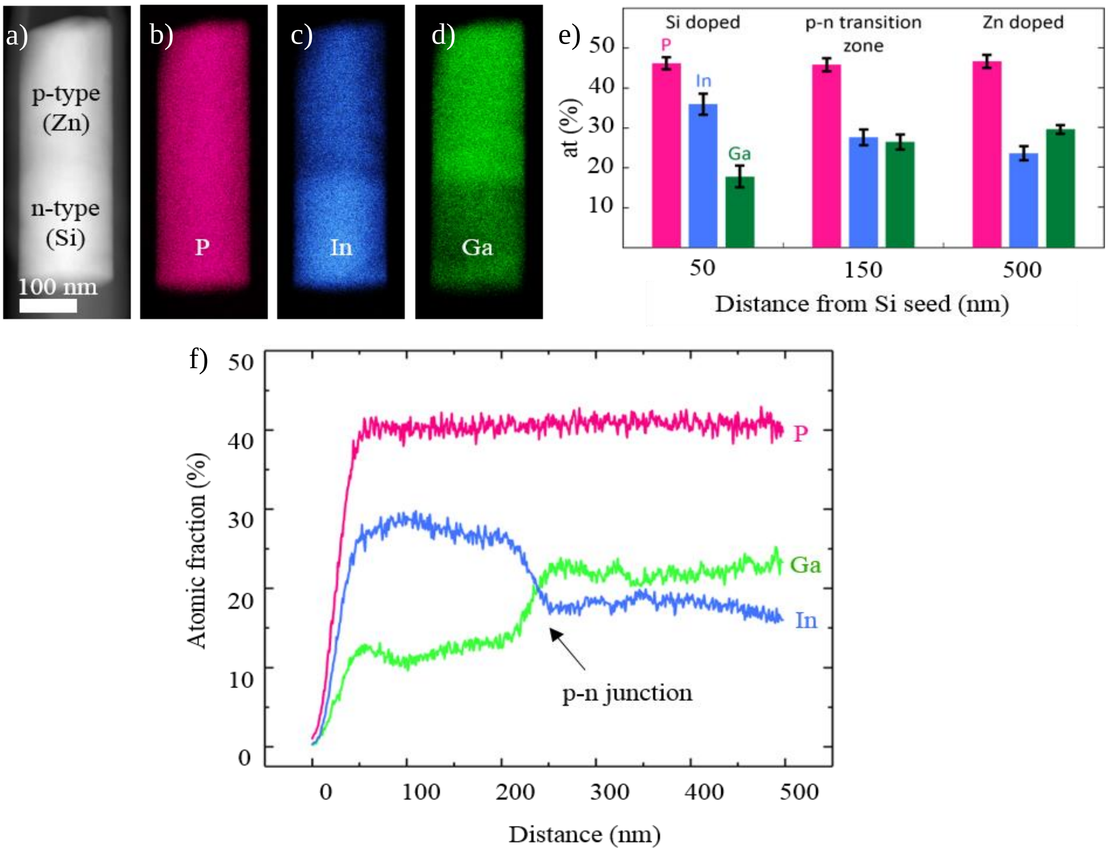

Figure 4.5 – (a) HAADF-STEM image of a p–n-doped $Ga_xIn_{(1-x)}P$ NW and the corresponding elemental maps of (b) phosphorus, (c) indium, and (d) gallium obtained from an EDX spectrum image. (e) Bar chart showing the In, Ga, and P contents at three different positions (50, 150, and 500 nm from the Si seed) averaged for six different NWs. The P content (pink) is constant in all NWs, while the In (light blue) and Ga (green) profiles display a reverse trend with a comparable composition at about 150 nm. (f) Averaged line profiles of the EDX elemental maps shown in panels b-d showing the variation in the atomic fraction of In, Ga, and P along the doped nanowire. Note that the In and Ga content are reversed at the p-n junction within 40 nm.

The incorporation of dopants is expected to also modify the overall electron density in the doped NWs since the resulting number of valence electrons is different from that of the undoped material. Here, EELS was applied to determine changes of the valence electron density across the NWs. In particular, in the low-loss region of the EELS spectrum, the most prominent feature corresponds to plasmon losses. Plasmon losses are collective oscillations of the valence electrons, and their energy is related to the density of the valence electrons. Therefore, changes in the valence electron density will be reflected by changes in the plasmon energy peak [155]. The doped NW displayed in Figure 4.6a is the same as the one investigated by EDX in Figure 4.5a. The green rectangle indicates the area in which the EELS spectrum was acquired. After aligning the spectrum image by using the zero-loss peak, the spectra were background subtracted by fitting a decaying power-law function to an energy window just in front of the plasmon peaks. Thus, two distinct plasmon peaks were obtained for the n- and p-doped sections of the NW at plasmon energies $E_{p,n}$ = 15.0 eV and $E_{p,p}$ = 15.6 eV, respectively (see Figure 4.6c). The same analysis performed on six different NWs gave average plasmon energy values of (15.0± 0.09) and (15.51 ± 0.07) eV for the n- and p-doped sections, respectively. Figure 4.6b shows the plasmon energy map obtained by performing a nonlinear least-square fitting to the acquired spectrum image and corresponding to the region in the green rectangle in Figure 4.6a. The difference in bulk plasmon energy at the bottom and at the top of the NW is evident, demonstrating that the distinct doping incorporation affects both the chemical and electronic properties of the material. However, from the EDX results obtained previously, we infer that this energy shift is mainly caused by a change in the Ga/In ratio across the NW rather than merely by the presence of dopant atoms. For this reason, as the bulk plasmon energy E_p varies linearly with composition [236], we used the two extreme compositions (InP and GaP) as standards to check the validity of our measurements. The reference spectra (acquired using the same experimental conditions) from bulk InP and GaP exhibit bulk plasmon peaks at E_p = 14.37 eV and 16.55 eV, respectively. By performing a linear regression, we obtained the following equation for the plasmon energy in electron volts:

$$E_p\ (\text{eV}) = 0.0218x + 14.37 \tag{4.1}$$

where x is the gallium percentage. Thus, by using the E_p values extracted from the plasmon map, an average composition of x = 0.29 ± 0.04 and 0.52 ± 0.03 is obtained, corresponding to a lattice constant equal to (5.74 ± 0.02) and (5.64 ± 0.01) Å for the n- and the p-doped segment, respectively. These values are in excellent agreement with the data derived from the EDX measurements. No remarkable changes in the width of the plasmon peak (~3.0 eV) were detected between the top and the bottom of the NW. The $Ga_xIn_{(1-x)}P$ lattice parameters obtained by GPA, STEM-EDX and STEM-EELS from the undoped and doped NWs are summarized in Table 4.1.

	$Ga_xIn_{(1-x)}P$ lattice parameter (Å)		
	undoped	n-segment	p-segment
GPA	5.78 ± 0.10	5.68 ± 0.10	-
EDX	5.77 ± 0.02	5.73 ± 0.03	5.64 ± 0.01
EELS	-	5.74 ± 0.02	5.64 ± 0.01

Table 4.1 – $Ga_xIn_{(1-x)}P$ lattice parameters of undoped and doped NWs obtained by GPA, STEM-EDX, and STEM-EELS.

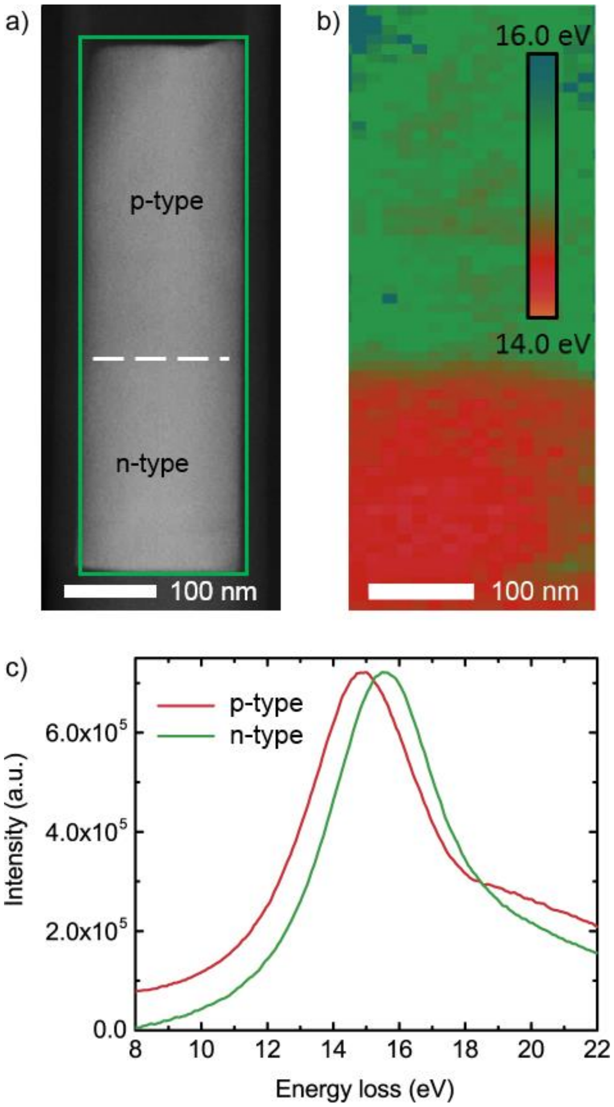

Figure 4.6 – HAADF-STEM micrograph of a p-n-doped NW with overlaid green rectangle corresponding to the area used for EELS spectrum image acquisition. (b) Bulk plasmon map extracted from the EELS spectrum image evidencing the presence of two distinct regions with different plasmon energies. (c) Bulk plasmon peaks extracted from the spectrum image at the n-doped (green) and p-doped (red) sections.

CL measurements were carried out in order to access the optical characteristics of the p-n junction and to link them to the compositional characterization previously presented. In Figure 4.7, red corresponds to the emission centered at 1.73 eV, green to1.93 eV, and blue to 1.98 eV. This color coding identifies three different regions of emission along the NW long axis, which overlap with the positions of the n- and p-doped sides of the junction as well as with the transition region between these two. Figure 4.7c shows CL spectra representative of the three distinct areas observed in Figure 4.7b. The CL data in both Figure 4.7(b, c) shows that the emission energy from the n-doped segment is lower (1.73 eV) than from the p-doped one (1.93 eV). The emission-energy difference between the p- and n-type regions can be mainly explained by the different alloy compositions observed by EDX and EELS [237]. Yet, the experimental emission energy is lower than the expected band gap; in particular, in the p-doped segment, the emission is a few tens of milli-electron volts lower than the low-temperature band-gap values reported in the literature [237,238]. The exciton binding energy of bulk GaInP is too small to justify this redshift [239]. On the contrary, in both the p- and n- regions, we estimate high concentrations of dopants (exceeding 10^{18} cm^{-3}), which can cause a narrowing of the optical band gap and account for the observed redshift. It is also interesting to notice that the redshift is less pronounced in the n-type NW segment. Since Si is used as a dopant in this segment, this is probably a consequence of the compensation that affects the Si doping [240]. At the interface, both peaks are visible and show a blueshift with respect to those observed farther from the interface. Such a blueshift is more pronounced in the case of the emission-related with the p-type segment (1.98 eV) than the one related with the n-type segment (1.74 eV). Here, the CL beam mainly probes the depletion region of the p-n junction. As a result, the emission energy blueshifts and approaches the electronic band-gap energy (2.04 eV for the p-type $Ga_{0.55}In_{0.45}As$ segment and 1.74 eV for the n-type $Ga_{0.33}In_{0.67}As$ segment [237]). Other phenomena may also contribute to the shift of the emission energy in CL. For instance, the high-power density of the electron beam can blueshift the emission by band-gap filling [241], and alloy reordering is reported to redshift the GaInP emission by 100 meV [242]. However, the fact that the CL signal blueshifts at the p-n interface and redshifts elsewhere with respect to the intrinsic band gap supports the role of the dopant levels as a mediator of the observed luminescence.

In conclusion, we have demonstrated the first monolithic integration of $Ga_xIn_{(1-x)}P$ vertical NWs on (111)-oriented Si substrates by using TASE. By employing a combination of aberration-corrected HAADF-STEM imaging and spectroscopy techniques, we have measured the structural and compositional properties of intrinsic and doped $Ga_xIn_{(1-x)}P$ NWs. We show that, in the absence of dopants, TASE allows growing highly homogeneous NWs with a zinc-blende structure and a high density of planar defects. Next, our observations show that the addition of Zn atoms as p-dopants results in a clear reduction of the number of stacking faults with a subsequent increase of the Ga incorporation, proving that the preferential growth of the zinc-blende phase is not uniquely associated with a modification of the wettability of the metal nano-catalyst, as previously reported [229,243]. Finally, by performing CL measurements, we provide experimental evidence that donor and acceptor energy levels are introduced in the energy gap by the dopant atoms. The results presented here provide new insights into the integration and doping of ternary III-V NWs on the Si platform for the next generation of photovoltaic and optoelectronic devices.

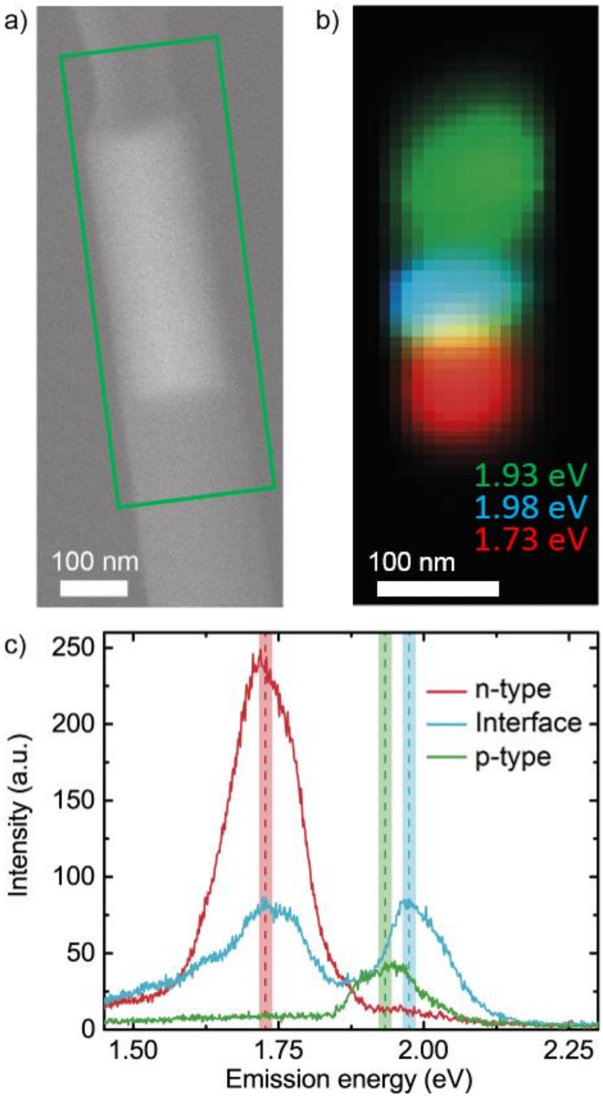

Figure 4.7 – SEM image of the doped NW investigated by CL. (b) False-colored CL map corresponding to the green window in panel (a) extracted from the CL spectrum image evidencing the presence of three distinct regions with different emission energies. (c) Emission bands extracted from the spectrum image at the bottom n-doped (green) segment, top p-doped (red) segment, and the interface (blue). The dashed lines highlight the emission peaks 1.73 eV (red),1.93 eV (green), and 1.98 eV (light blue) used for the CL map.

This section is adapted with permission from N. Bologna et al. Dopant-Induced Modifications of $Ga_xIn_{(1-x)}P$ Nanowire-Based p–n Junctions Monolithically Integrated on Si(111). ACS Appl. Mater. Interfaces, 2018, 10 (38), pp 32588–32596. Copyright (2018) American Chemical Society.

4.3 Investigation of electrostatic potential in doped GaAs nanowires by off-axis holography

The off-axis holography investigations were performed on GaAs NWs instead of the previous $Ga_xIn_{(1-x)}P$ samples. In fact, the ternary compounds showed compositional inhomogeneities able to affect the phase variations. Such compositionally induced variations of the MIP are of the order of 0.08 V (calculated using the equations given in [244,245]) - i.e. smaller than the expected variation for the built-in potential due to p-n doping implementation. Nevertheless, we still decided to perform the holography measurements on the binary samples to avoid having to deal with compositional variations within the same NW and between different NWs. Holography experiments were performed on GaAs NWs with different dopants and concentrations. The first investigation was performed on p-n junctions with Zn and Si as p- and n-dopants, respectively. The nominal concentrations were the same as those reported in the previous section of this chapter, i.e. above 1.0×10^{18} cm^{-3}. The microscope was set with a spot size 3 and average electron beam current density equal to 0.45 nA nm^{-2}, and the applied biprism voltage was chosen in the 120-190 V range, corresponding to 6-9 nm in spatial resolution. In order to avoid saturating the camera, exposure times were set in the 5-13 second range depending on the applied voltage and selected magnification. Figure 4.8a shows the electron hologram of a 1112 nm long NW. The extraction of the amplitude and phase components from the acquired holograms was carried out by the procedure explained in detail in section 2.1.3. Panels (b) and (c) display the amplitude and phase images extracted from the hologram, and the corresponding line profiles averaged over 17 pixels obtained along the white dashed lines are shown in panels (d) and (e), respectively. The line profile of the amplitude image does not show large variations in intensity revealing that the diameter of the nanowire does not change significantly from the p- to the n-section, although a slight decrease in thickness is perceptible. In general, the amplitude modulation can be induced by different factors that could influence at the same time the phase image, adding more difficulty to the data interpretation. For example, inelastic interaction and thickness distribution can modify the amplitude image. Furthermore, interference effects in the crystal, like dynamic and Fresnel diffraction effects could affect the overall interpretability [246]. In fact, the dark contrast regions present in all the following amplitude images, especially at the edges of the NWs, can be connected to these effects rather than crystallographic imperfections of the NWs. In fact, HAADF-STEM imaging has been performed on each sample dismissing any correlation between the dark contrast and the local crystal structure. In the particular NW of Figure 4.8, at around 900 nm from the beginning of the NW, a sudden decrease in the intensity of the profile in Figure 4.8d related to the presence of the Lacey carbon support is visible.

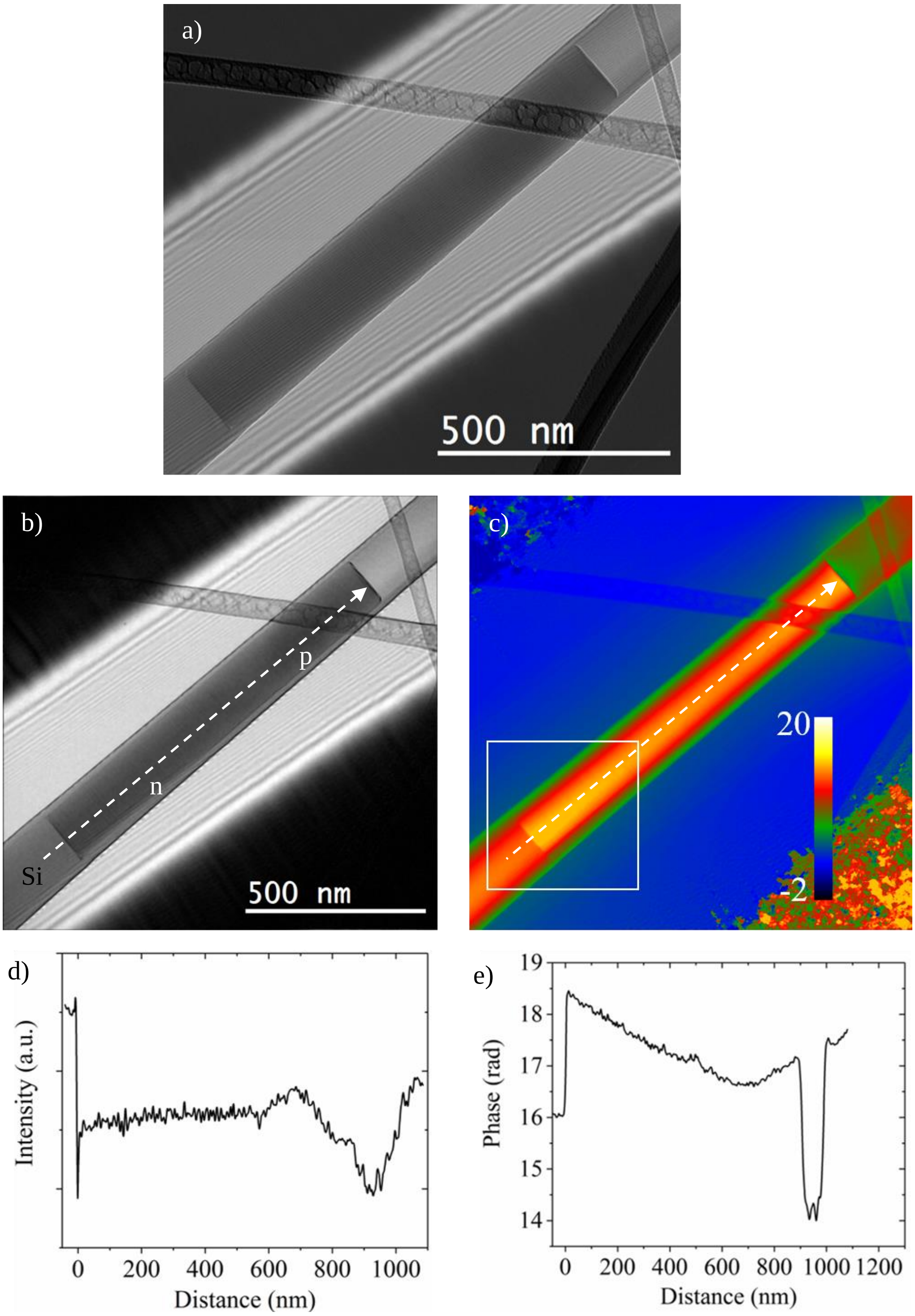

Figure 4.8 – (a) Hologram of a GaAs NW exhibiting a not well-defined p-n junction. (b) Amplitude and (c) phase images reconstructed based on the hologram shown in panel (a). (d, e) Corresponding line profiles averaged over 17 pixels obtained along the white dashed lines indicated in panels (b, c), respectively. The color bar indicates the phase in radians.

On the other hand, a continuous decrease in the phase line profile in Figure 4.8e is visible from the beginning of the nanowire to about 750 nm, where the phase undergoes a rise until the top end of the nanostructure. Moreover, the carbon support contributes to the profile with a strong phase decrease in a limited region of the sample from 900 to 1000 nm. Surprisingly, the line profile extracted from the phase image (Figure 4.8e) does not reveal any sharp p-n transition in the nanowire, as shown in other published experiments [247]. For this type of composition and doping amount, the built-in potential should be around 1.53 V, corresponding to a phase variation of circa 1 rad. However, this is not detectable in our phase profile. This could be attributed to the diffusion of Zn dopants from the p- to the n-segment, caused by a too high growth temperature or too long growth time. However, a careful inspection of the line profile reveals a possible depletion region at around 650-750 nm from the Si-NW interface.

A magnified image of the white square in Figure 4.8c is shown in Figure 4.9a. At this higher magnification, it is possible to uncover the contribution of structural planar defects on the phase component. In fact, in the corresponding line profile of Figure 4.9b, overlaid with the gradual phase decrease, three small peaks are perceptible at 140 nm, 220 nm and 310 nm from the interface with the Si seed. They are twin boundaries and stacking faults and are highlighted with three arrows. Each planar defect contributes to the phase profile with a reduction of ~0.2 rad. The variation in phase due to the presence of planar defects has already been studied on similar systems [248–250]. In fact, it has been demonstrated that potential fluctuations might be present at the interface between planar defects due to a variation of the stacking sequence and segregation phenomena. The observation of these phase variations due to planar defects confirms that the experimental parameters used in the holography measurements allows for a spatial resolution of 6-9 nm. Such spatial resolution would allow us to localize the depletion region whose lateral extension is expected to be in the range of 60-70 nm.

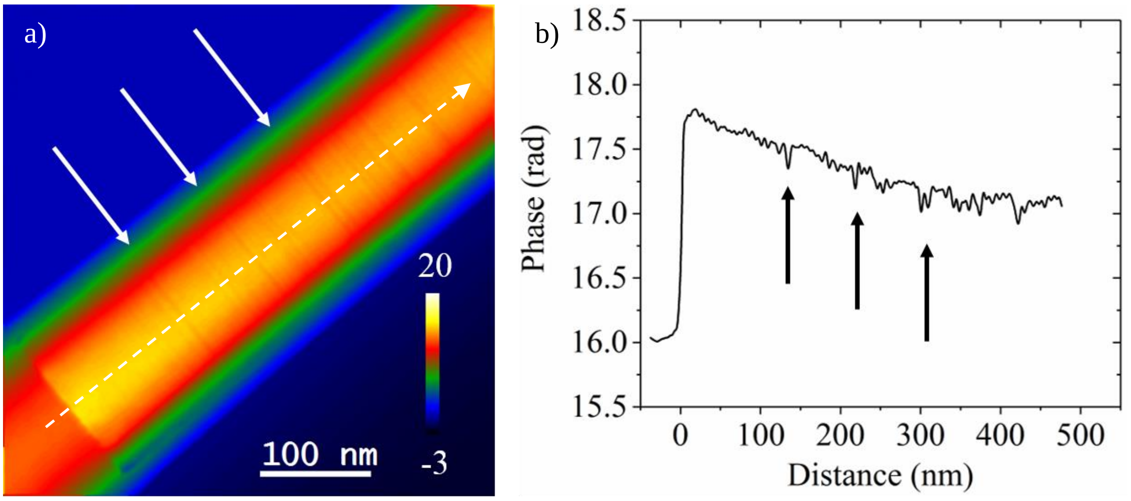

Figure 4.9 – (a) Magnified phase image of the white square in Figure 4.8c showing a high density of planar defects present in the NW. (b) Line profile acquired along the dashed line in panel (a) highlighting the contribution of the planar defects on the phase information. The location of three

major planar defects is indicated with arrows in both panels although many other planar defects are also visible. The color bar indicates the phase in radians.

As the thickness (and geometry) of the NW can have a significant effect on the phase shift, and in order to differentiate it from the one induced by the doping atoms, a simulation of the phase changes through a cylindrical NW with same experimental dimensions was performed. As explained in chapter 2.1.3, the phase shift in the vacuum surrounding the NW is zero. Thus, we applied a threshold value to the phase image in order to extract the variations in the NW diameter. In particular, we first applied a rotation to the phase image in order to vertically align the NW. Then, for each horizontal row of pixels in the image, we extracted the NW diameter and derived the corresponding thickness profiles by using the coversine function assuming a cylindrical symmetry for the NW. By merging all the thickness profiles a two-dimensional thickness map $t(x,y)$ was obtained and used for the calculation of the phase map. For this particular NW, we simulated the SiO_2 template as well since it also contributes to the reconstructed phase. Actually, our simulation comprises both a cylindrical core representing the GaAs and an outer hollow cylinder corresponding to the template. The Si seed was neglected for the present analysis. In order to simulate the phase variation of this core-shell nanostructure, equation 2.27 was applied with the following values: $C_E = 6.5414 \times 10^6$ rad V^{-1} m^{-1} (calculated based on the microscope's parameters), $V_{GaAs} = 14.1$ V and $V_{SiO_2} = 10$ V, which are standard values for this type of materials [244,251], and the calculated $t(x,y)$. Therefore, the simulated phase map shall only reflect the phase variations due to changes in thickness and geometry of the NW as no dopant atoms are considered in the calculations (the same is true for the successive phase maps). The resulting simulated phase map is shown in Figure 4.10b together with the experimental one in panel (a). The line profiles in Figures 4.10 (c) and 4.10(d) extracted along the black dashed transversal lines show the good agreement between the simulated and experimental data. In both graphs the silicon oxide shell is clearly visible from the saddle points of the line profiles.

More interesting, however, are the phase variations along the NW longitudinal direction as they shall provide information about the incorporation of dopants in the structure. This is shown in Figure 4.10e, where the blue and green profiles were extracted from the longitudinal dashed lines indicated in the experimental and simulated maps, respectively. Note that both profiles display a similar behavior with a continuous decrease of the overall phase from the Si-GaAs interface to the region right before the carbon strip. This effect can be reasonably associated to a thickness variation from the bottom to the top of the NWs. However, the difference between the two profiles is not constant and is particularly larger at the bottom part of the NW. At this position the discrepancy is about 1.4 rad and might be connected to the doping levels in the material which would further raise the phase magnitude at the n-segment with respect to the p-segment. However, no conclusive statement about the presence of a p-n junction in this NW can be made from the present data.

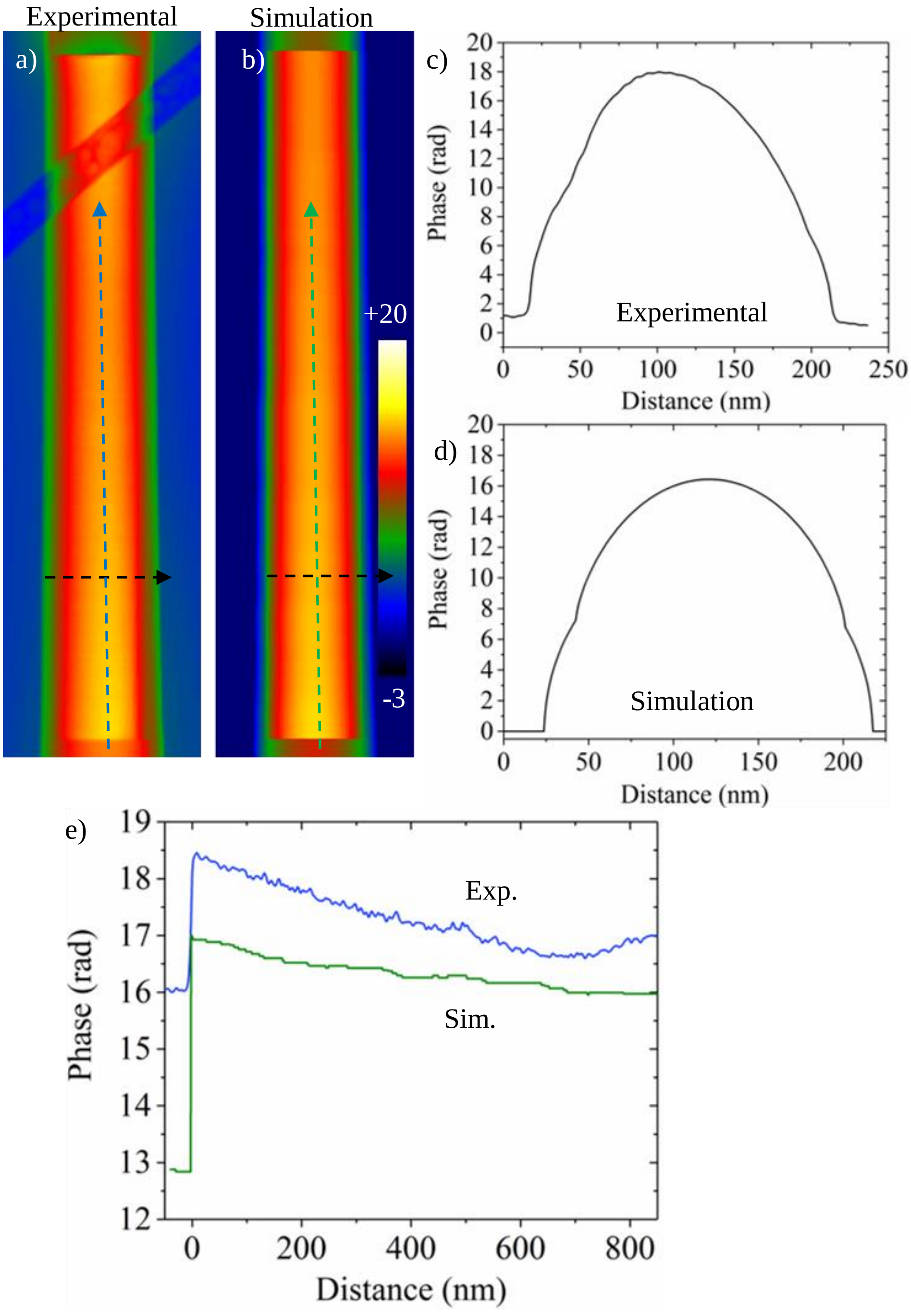

Figure 4.10 – (a) Experimental and (b) simulated phase maps of the NW in Figure 4.8. The color bar indicates the phase in radians. (c) Experimental and (d) simulated line profiles obtained along the transversal black dashed lines indicated in panels (a) and (b), respectively. (e) Comparison between the longitudinal line profiles obtained along the blue and green dashed lines indicated in the experimental and simulated phases of panels (a) and (b).

Given the small length of the NWs (~1000 nm), it was very challenging to transfer them on the carbon grid by gently rubbing it against the chip's surface. This procedure resulted in a very low success rate. Moreover, only very few of the transferred structures were suitable to be investigated by off-axis holography as it is required the presence of vacuum regions close to the area of interest, so that the reference wave (propagating in vacuum) could be overlapped with the object wave, as explained in section 2.1.3. Finally, we also had to disregard those NWs whose initial part (where the p-n junction was expected) was lying on top of a strip of Lacey carbon because, as seen in Figure 4.8, carbon induces a strong phase change. Therefore, a new strategy to obtain longer NWs without increasing too much the growth time was adopted. It consisted in growing an additional GaAs SAG segment on top of the TASE grown NW. This strategy allowed transferring many more NWs from the Si substrate to the carbon grid, increasing the probability to find suitable structures for the holography experiments.

The TASE/SAG grown hybrid nanostructures are shown in the SEM images of Figure 4.11. Panel (a) is an overview image of the sample showing the obtained vertical NWs, while in panel (b) a magnified image of a single NW exhibits the sections grown with the two different methods: the first part (consisting of Si and GaAs) is grown with TASE and the second part (GaAs) is grown with the SAG process. Then, Figure 4.11c reveals the hexagonal faceting of the SAG section highlighting the six equivalent {112} facets (not present when the NWs are grown with the TASE growth technique).

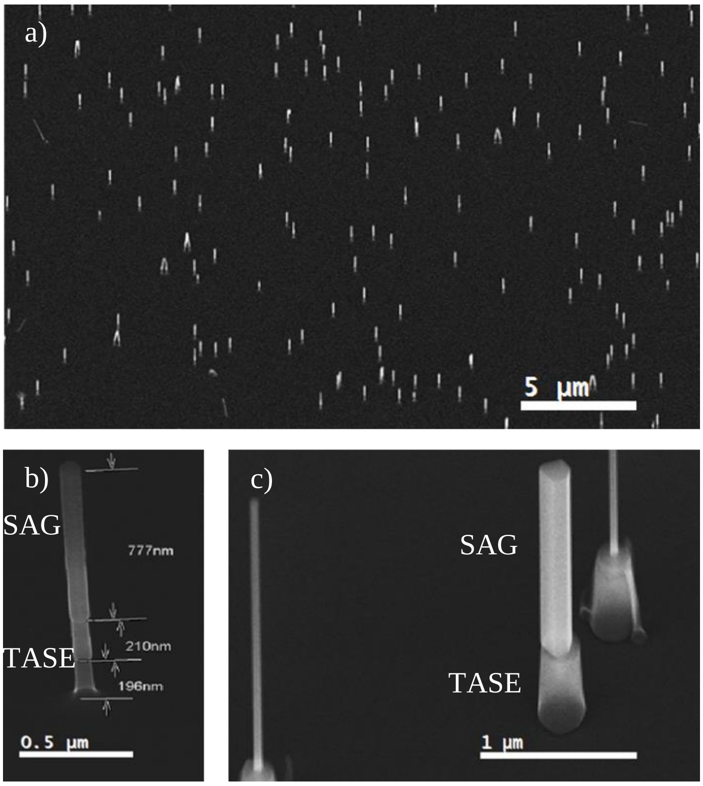

Figure 4.11 – (a) SEM overview image of the GaAs NWs grown with the TASE/SAG hybrid growth. (b) High magnification image of a single NW showing the TASE and SAG sections.

(c) Detail of a hybrid NW, whose SAG grown section clearly exhibits hexagonal faceting with six equivalent {112} facets.

The GaAs NWs grown in this fashion consisted of a n-doped section (with Si) between two intrinsic/undoped regions. A typical NW investigated by holography is shown in Figure 4.12. Both the amplitude and phase images are shown in panels (b) and (c), respectively, and were extracted from the electron hologram of panel (a). The line profiles acquired along the white dashed lines of the phase and amplitude images are given in panels (d) and (e). From the amplitude image in Figure 4.12b, the NW appears very homogeneous without any detectable difference between the TASE and SAG sections. Only a slight increase in the diameter is visible in the amplitude image and perceptible in the corresponding line profile at ~425 nm, as highlighted by the black arrows. However, different segments are visible in the phase image of Figure 4.12c and clear phase variations are revealed in the line profile of Figure 4.12e. Thus, three distinct regions can be identified: a first region with a constant phase decrease; then a second region with a plateau from 275 to 400 nm; and finally, a third region exhibiting a sharp increase of the phase before stabilizing at ~7.5 rad. Similarly to the NW shown in Figure 4.8, a phase gradient is present in the TASE section, which might be associated to a variation in the NW diameter. However, the second and third parts of the phase map deserve a more insightful discussion on the possible causes inducing such variations. First of all, the plateau defining the second region might correspond to the n-doped segment of the NW, which is found, as expected, in the last region of the TASE grown segment. However, the i-n-i doping incorporation should induce an enhanced phase shift for the n-doped region with respect to the intrinsic ones. Additionally, it is highly unlikely that the sharp phase jump observed at 400 nm is caused by a n-i transition. Finally, a bump can be identified within the plateau region, which could potentially be related to an i-n transition. However, from these preliminary data, it was difficult to advance more concrete conclusions.

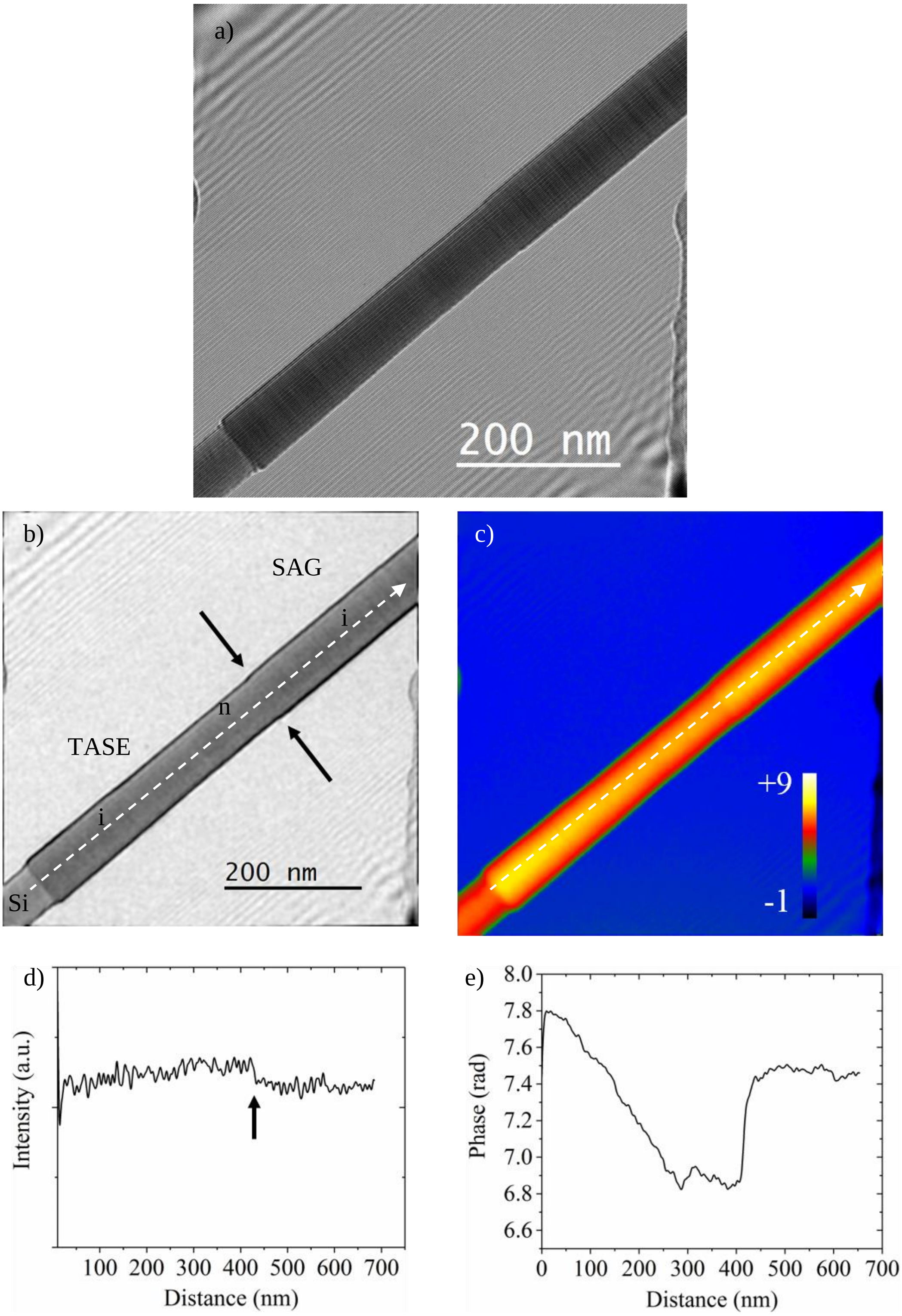

Figure 4.12 – (a) Electron hologram acquired from a GaAs NW exhibiting i-n-i junctions. (b) Amplitude and (c) phase images reconstructed from the hologram shown in panel (a). (d, e) Corresponding line profiles obtained along the white dashed lines indicated in panels (b, c), respectively. The color bar indicates the phase in radians.

In order to clarify the charge-doping-induced phase variations present in this NW, a simulation study similar to the one performed for the NW in Figure 4.8, was here conducted applying the same procedure. However, the current NW presented a very different geometry. As explained above, the first TASE segment grown with TASE has a cylindrical shape, while the second section grown with the SAG approach presents a hexagonal geometry. For this reason, the implementation of the coversine function was suitable only for the first section. For the second part, it was necessary to first understand the orientation of the {112} facets with respect to the incident electron beam, i.e. whether the hexagonal nanowire was lying on a facet or on an edge of the hexagon. A transversal line profile of the phase map across the SAG segment is shown with the blue color in Figure 4.13c and it clearly demonstrates that the nanowire sits on an edge. Once the orientation of the hexagon is known, the simulated phase map shown in Figure 4.13b can be built by adding together the cylindrical and hexagonal segments. In order to highlight the two different geometries, present along the NW, two different pairs of line profiles were acquired in two different regions and compared in panels (c) and (d). Panel (d) shows the simulated and experimental phase profiles in the first region of the NW, i.e. the cylindrical region at the bottom grown by TASE. The agreement between the two profiles is very good (note here that the SiO_2 template is not present in this NW). Panel (c) displays a similar comparison for the SAG NW section with hexagonal geometry. Also in this case, an excellent agreement is achieved throughout the entire section without any particular discrepancy between the blue and the green lines. Here, smoothing functions for the edges of the simulated hexagon were necessary to improve the overlapping of the profiles.

Then, we compared the phase profiles obtained along the longitudinal direction of the NWs in order to differentiate the phase variations due to changes in geometry/thickness from those induced by the doping elements. The comparison is shown in Figure 4.13e. The overall trend of the two profiles is fairly similar but a few differences can be noted. As earlier suggested in the discussion of Figure 4.12, the sharp phase jump observed at 400 nm is here confirmed to be unconnected to any effect induced by the dopant atoms. In fact, the same abrupt phase change is visible across the simulated profile between the cylindrical and hexagonal sections of the NW, where only the electrostatic potential of GaAs was used. This result suggests that this phase jump is purely due to a change in the geometry/thickness of the NW as it transitions from a cylindrical to a distorted hexagonal geometry. Another difference is observed in the middle “plateau” region. The simulation shows, as expected, a completely flat profile because in this area both the geometry and thickness of the NW are constant. However, as previously discussed, the experimental profile shows a small bump in the phase magnitude which might be related to the presence of n-dopants in this specific region.

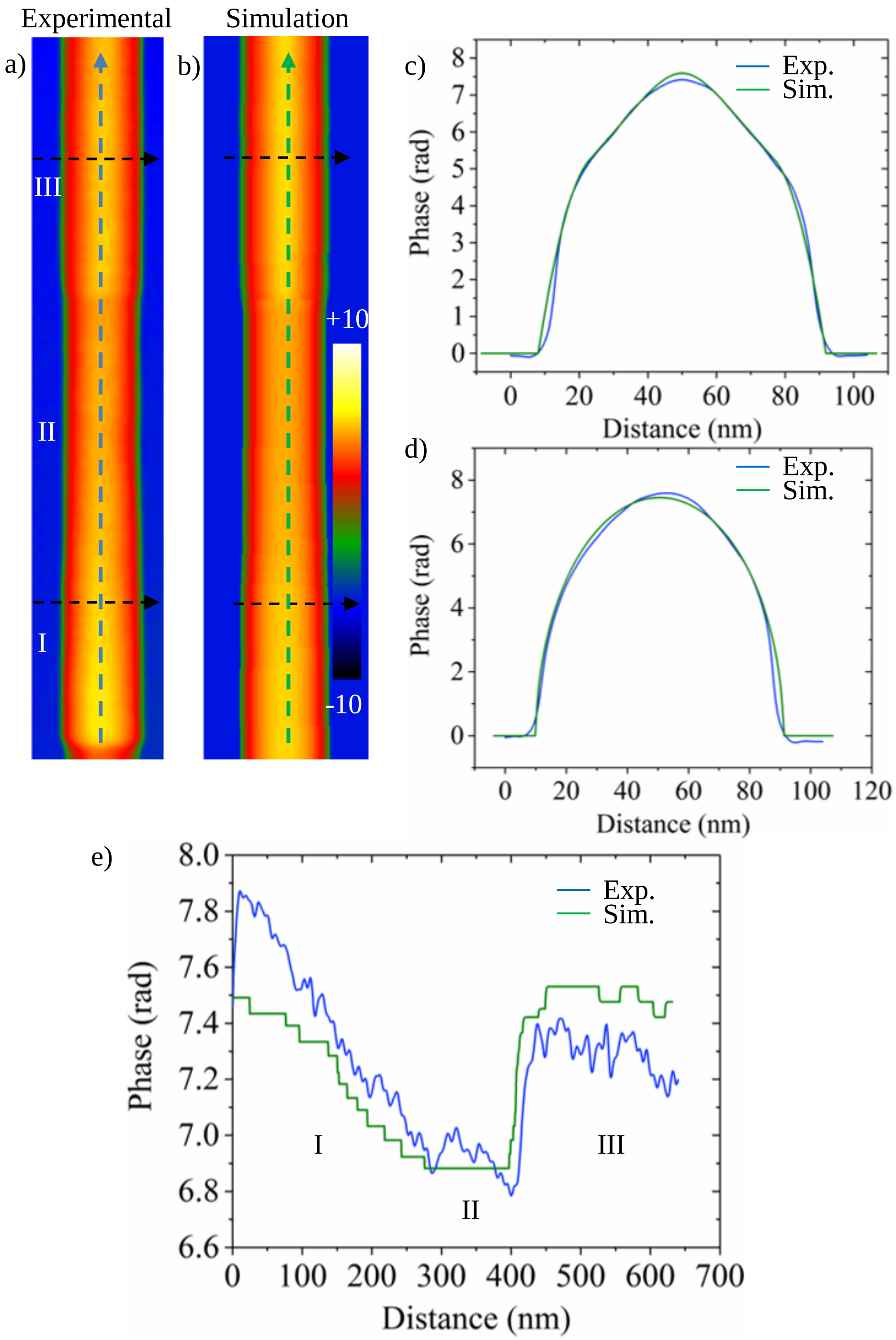

Figure 4.13 – (a) Experimental and (b) simulated phase maps of the NW in Figure 4.12. The TASE (SAG) section is located at the bottom (top). The color bar indicates the phase in radians. Comparison of the transversal experimental and simulated line profiles in the TASE (d) and SAG (c) regions. (e) Comparison between the longitudinal experimental and simulated line profiles acquired along the blue and green dashed lines of panels (a) and (b), respectively. The same color code applies to all graphs.

Another NW with the same doping profile (i-n-i) and geometrical characteristics, i.e. grown using the TASE/SAG hybrid approach, was analyzed in order to confirm the observations advanced for Figure 4.13. The acquired hologram is shown in Figure 4.14a where the Si seed is visible in the lower left corner. The reconstructed amplitude and phase images are presented in panels (b, c). Even though the amplitude contribution looks less homogeneous than the previous case due to the presence of planar defects, the overall trend is constant with a slight increase of the intensity from left to right due to a reduction in thickness. However, a local minimum is visible in the line profile of panel (d) at around 500 nm and it is also visible in the amplitude image as a short dark segment. This might be induced by a very high concentration of planar defects located in that very small region or due to a local thickness/geometrical variation. The phase image of the NW can be separated in three different regions from left to right: (I) a constant phase region in the TASE segment; (II) a plateau with a lower phase value in the TASE segment; (III) a flat region displaying a larger phase shift in the SAG segment. This becomes clearly visible in the corresponding phase line profile shown in panel (e). However, some discrepancies with respect to the NW analyzed in Figure 4.12 are observed and are here addressed. First, the initial TASE segment does not exhibit a gradual phase decrease as observed in the two previous NWs; instead it shows a roughly flat phase of about 8 rads. Second, the plateau region in this particular NW is much more visible than in the previous NW and it spans from 350 from 500 nm. Then, at 500 nm, the TASE to SAG transition takes place as observed by the abrupt phase jump.

The region II with its pronounced bump, visible in the NWs of both Figs. 4.12 and 4.14, is presumably caused by the presence of dopant atoms. However, at this stage it is not clear why two minimums are observed at the I-II and II-III interfaces.

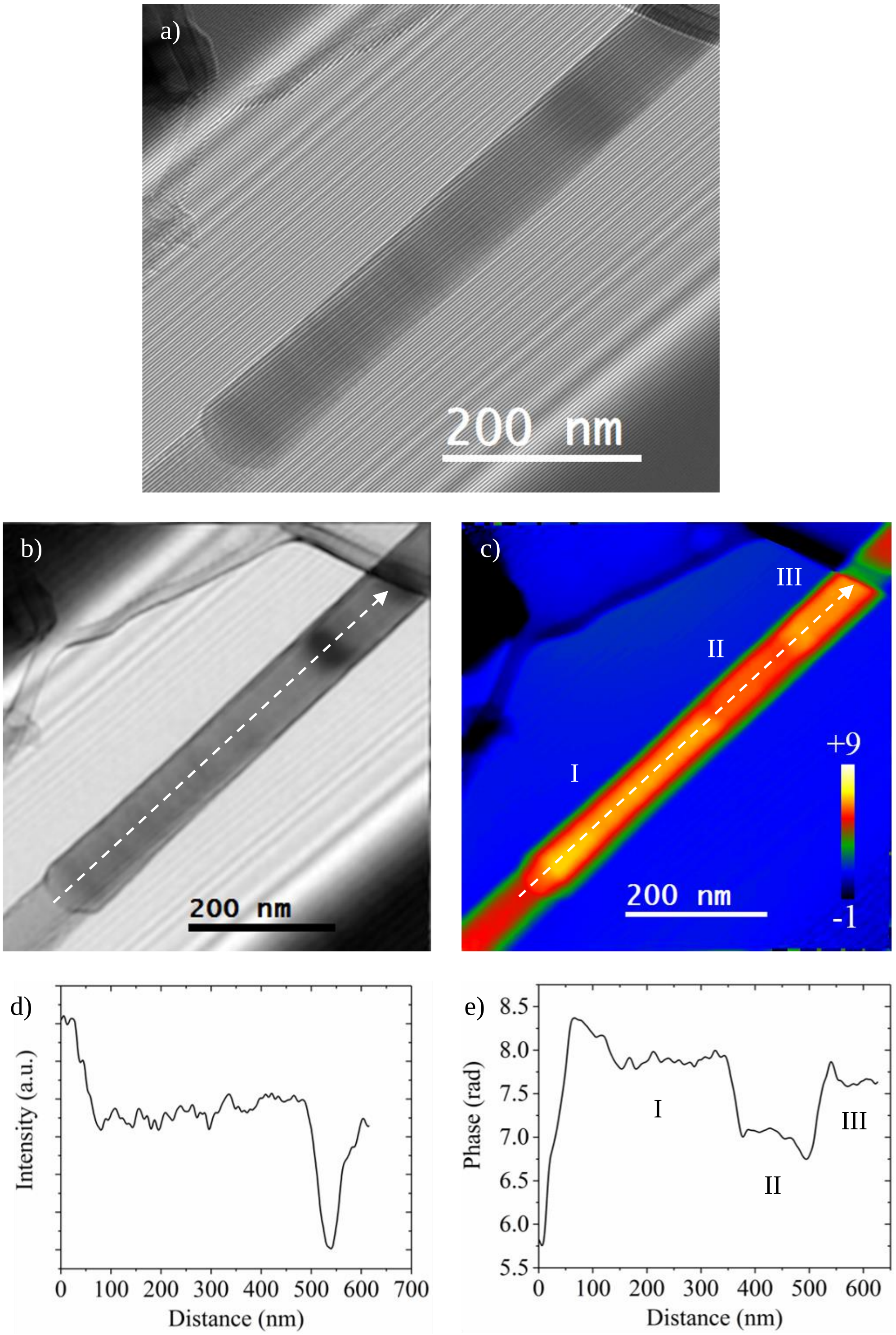

Figure 4.14 – (a) Electron hologram of a second GaAs NW exhibiting the same characteristics (i-n-i junctions and TASE/SAG segments) as in the previous NW. (b) Amplitude and (c) phase images reconstructed from the hologram shown in panel (a). The color bar indicates the phase in radians. (d, e) Amplitude and phase profiles extracted along the white dashed lines indicated in panels (b, c), respectively.

Again, for this NW we attempted to interpret the observed phase variations by simulating the phase map by taking into account the shape of the NW and the built-in potential of GaAs only, and by comparing it with the experimental one. In order to replicate the same geometry, we verified, through the acquisition of transversal line profiles, the shape of each NW section. The transversal lines are visible as black dashed arrows in the experimental phase image of Figure 4.15a and the corresponding extracted profiles are displayed in blue in Figure 4.15(c) and 4.15(d). Here, it is evident that the segment II of the NW, as well as the third one, has a hexagonal geometry, while section I is cylindrical. Moreover, the orientation of the hexagon is different with respect to the one in the previous NW. In fact, here the {112} facet, and not the edge, is oriented upwards. This geometry was taken into consideration for simulating the phase image of the NW and is presented in Figure 4.15b. The experimental and simulated line profiles in panels (c) and (d) show a very good agreement along both transversal sections obtained in segments I and II. In Figure 4.15e a comparison between the longitudinal experimental (blue) and simulated (green) profiles is shown. Several conclusions can be extracted from comparing these data:

1. At ~350 nm, the observed abrupt phase shift separating regions I and II is mainly due to a change in the NW geometry from cylindrical to hexagonal. Thus, this jump appears to be unconnected to any effect induced by the dopant atoms. However, as opposed to the results obtained for the previous NW in Figure 4.13, here the change in geometry induces an increase in the phase shift. This might be attributed to the different orientation of the hexagon with respect to the incident electron beam.
2. At 500 nm, the observed net phase shift separating regions II and III cannot be related to changes in the geometry and the thickness of the NW as they are here constant. Thus, we suspect that the n-dopant species were incorporated in this particular NW in the SAG segment instead than in the TASE segment.
3. Finally, as mentioned above, a i-n-i type junction should display an increase in the phase shift for the n-doped segment relative to the intrinsic segments. However, in all the NWs examined in the present study we observe the opposite behavior. Here, it is also important to recall that depending on their concentration, Si dopants can act either as n- and p-dopants. In fact, for high doping concentrations (higher than 10^{18}) the Si dopants are incorporated as acceptors on the As lattice sites [240]. As the Si concentration in our NWs is ~ 10^{18}, we cannot rule out that the Si dopants are incorporated as acceptors leading to p-type conductivity.

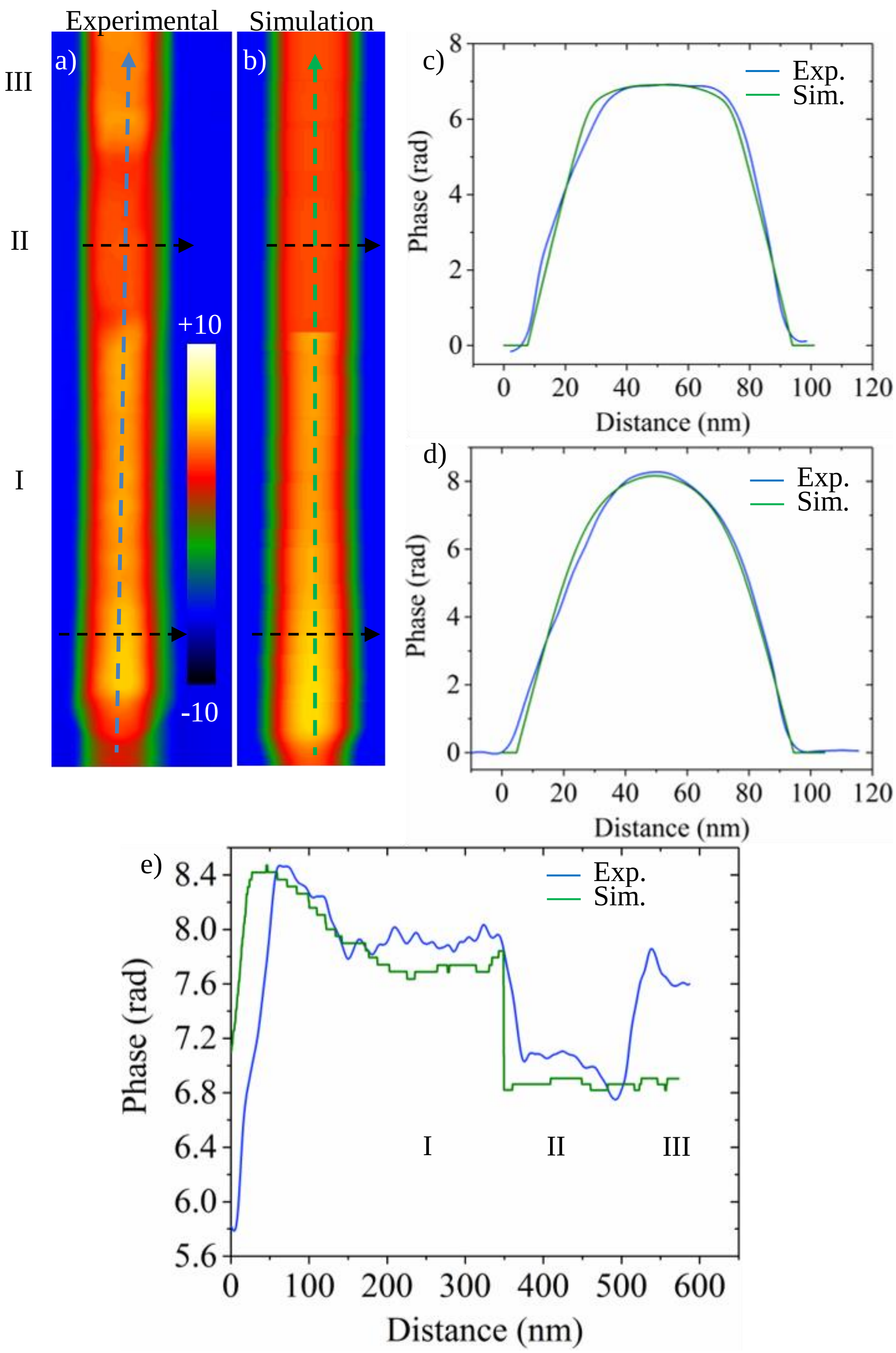

Figure 4.15 – a) Experimental and (b) simulated phase maps of the NW in Figure 4.14. The TASE (SAG) section is located at the bottom (top). The color bar indicates the phase in radians. Line profiles extracted from the experimental and simulated phase maps along two different transversal directions in the TASE and SAG segments (indicated with black dashed lines) are presented and compared in panels (d) and (c), respectively. (e) Comparison between the experimental and simulated profiles along the longitudinal direction. Blue and green lines correspond to experimental and simulated profiles, respectively.

In conclusion, a couple of additional aspects on the holography experiments here performed must be discussed. For example, the use of EELS to estimate the thickness distribution along the NW could help to discriminate the thickness contribution to the MIP with respect to the one induced by the active dopants present in the NWs [153]. Alternatively, a calibration of the amplitude image can be performed. In fact, it is known that in holograms where vacuum is used as a reference, the amplitude image can be normalized to yield unity in the vacuum. In absence of strong dynamical diffraction effects, the normalized amplitude is an exponentially decreasing function with the specimen thickness [252,253]. In this way, being the inelastic mean free path and the theoretical MIP of the semiconducting material constituting the NW known, the phase contribution of the nominal undoped sample can be subtracted from the experimental phase to isolate the contribution due to the active doping. These approaches are alternative methods to the geometrical reconstructions applied during our simulations. However, it must be taken into account that our samples present strong diffraction effects which might hinder the use of the alternative approaches. Moreover, the application of reverse biasing at the NWs directly in the microscope by in-situ experiments could increase the built-in potential at the p-n junction. This last approach, which was already studied in literature [254,255], would certainly reduce the difficulties in mapping active dopant regions in our III-V NWs.

Finally, it is important to consider that, given the high surface-to-volume ratio of our nanostructures, inactive layer thickness and surface charging could play a key role in making the interpretation of the phase profiles extremely complicated. In fact, the surface states and inactive layer thickness effects have already been demonstrated experimentally and with simulations and their effect is to reduce the overall phase variation and consequently the detectable potential of the sample [256–261]. Moreover, in the first nanowire investigated in this work by off-axis holography, the SiO_2 template nanotube is still present and could represent an additional source of surface charging [259]. Lastly, the presence of defects at the NW-SiO_2 interface could also impact the detected phase. Even though dopant profiling has been measured by off-axis holography in similar samples with comparable dopant concentrations [247], our NWs could be more affected by surface states and superficial defects due to the SiO_2-NW interface. Methods to overcome these issues have been demonstrated during the last few years, where the use of high dopant concentrations and the thermal annealing might reduce these detrimental effects [260,262]. These approaches might improve the quality of the NWs and, consequently, the interpretation of the phase maps also in our samples. In conclusion, I would like to mention the issue of the sample preparation. For the present experiments, the NWs were directly transferred to a TEM carbon grid by scratching the chip’s surface. For this reason, intrinsic geometrical effects arise while observing the entire nanostructure, i.e. different cross-sectional geometries and changes in the projected thicknesses. By preparing a cross-section TEM specimen by FIB allows to reduce these effects. Indeed, several studies show that the use of the FIB might reduce the effects induced by an inhomogeneous thickness of the sample [170,255]. On the other hand, damage induced by FIB preparation, especially on the surface of the specimen, could increase the detrimental effects associated with surface state and, consequently, reduce the detected variation in phase. However, it is not excluded that surface charging and inactive layers are still present in our samples and that might be one of the reasons why the interpretability of the phase maps is so challenging for our experiments. One last remark is that we cannot exclude band bending phenomena at the wire surface which could add an additional level of complexity to the interpretation of the reconstructed phase maps [259,262]. For all these reasons, the measurements performed in this section concerning off-axis holography, especially the one reported in Figure 4.14, must be considered as preliminary results which require further investigations by optimizing the sample growth and its characterization.

5 Conclusion & Outlook

In this thesis, we have employed various TEM techniques to characterize III-V NWs grown by TASE. More specifically, we have focused on the analysis of structural defects and on the local electronic properties of different binary and ternary alloy NW systems grown on several differently oriented Si substrates. To this end, this thesis shall play a key role in the III-V NW integration in electronic and optoelectronic devices by using this novel epitaxy technique.

In the first part of the thesis, we have shown that the wide growth parameter window tolerated by TASE allows obtaining planar defect-free GaAs NWs on a CMOS compatible substrate. In particular, varying temperatures and V/III ratios were applied in order to find the proper combination to achieve defect-free NWs. Moreover, as the NWs are grown in lateral hollow SiO_2 templates, the morphology of the nanostructure remains unaffected regardless of the parameters used. This advantageous situation is not given in conventional growth methods like VLS and SAG, where both substrate and growth parameters might influence the final NW shape. Further, our findings strongly indicate that the formation of planar defects does not derive from strain effects, SiO_2-GaAs interactions, or surface impurities, but are solely consequence of the high susceptibility of the (111)B facet to twining. The realization of the first defect-free GaAs NW on a CMOS compatible substrate without the use of any metal catalyst represents an important step towards the integration of III-V NWs in commercial nanodevices such as MOSFETs or TFETs. These observations are expected to be transferable to other III-V semiconductor material systems, like InGaAs or InAs, for the development of industry-oriented devices. In fact, present efforts at IBM-Research are placed to integrate ternary compounds like InGaAs in template oxides with shapes different from the classic cylindrical ones. The idea is to demonstrate InGaAs FinFETs integrated on Si by means of a novel template shape, i.e. planar oxide cavity. In theory, the continuous flow of precursors would allow to fill the entire oxide template and, by optimization of the various growth parameters, reduce the number of planar defects present in the device. Large improvements concerning the I_{ON} current and the SS are foreseen. Moreover, III-V semiconductors grown on CMOS compatible substrates in SiO_2 template ring cavities are planned in order to demonstrate optically active devices. In fact, defect-free GaAs and InGaAs nanostructures could be easily grown in such geometries creating micro-cavity lasers. These are only two among the possible innovative applications that TASE might bring to the present technology.

In this thesis, a particular type of defect formed at the intersection of stacking faults, namely stair-rod dislocations, occurring in planar GaAs NWs under certain growth parameters was also investigated. Stair-rod dislocations are characterized by the presence of single unpaired atomic columns which were identified as either Ga or As single-atomic columns by means of atomically-resolved EDX. Their effect on the electronic properties was investigated by means of DFT simulations. *Ab initio* calculations revealed an overall reduction in the energy gap with respect to the bulk material and the development of charge channels along the line defects, with a corresponding strong electric field between the channels. Thus, our results suggest the possibility to obtain strongly localized potential paths within the NWs which might host free carriers upon appropriate doping and help improve the carrier separation along the different dislocation cores. The next step shall be to intentionally generate NWs with this type of line defects and to experimentally verify, through the use of bias spectroscopy and field-effect measurements, the validity of the simulated results. This could result in devices displaying strongly localized potential channels with improved conductivity in the one-dimension. Recent studies have been performed in our group on InAs NWs integrated on CMOS compatible substrate, demonstrating ballistic mono-dimensional transport [263]. However, a stronger focus on the possible relationship with respect to the intrinsic atomic structure of such material could reveal a connection with the studies presented in this thesis.

The second part of this research project dealt with the investigation of doping incorporation in different III-V NWs systems. To start with, we investigated the effects induced by p- and n-dopants on the composition, structure and properties of p-n $Ga_xIn_{(1-x)}P$ NWs by comparing undoped and doped samples. We observed a reduction in planar defect density due to the incorporation of Zn atoms in the p segment. Although this effect was previously reported to be connected to a variation in the wettability angle of the metal seed particle, our results demonstrate that this effect is also observed for catalyst-free grown NWs, suggesting that other phenomena might be responsible for the stacking sequence. Moreover, we observed a larger incorporation of Ga and In atoms in the p and n segments, respectively. Thus, should be taken into account when targeting a specific composition for a certain device. Finally, CL measurements carried out on these NWs revealed a variation in the band gap along the p-n junction, providing the first experimental evidence for the presence of dopant-induced energy levels in these nanostructures. Our results about the influence of doping on the chemical composition of the $Ga_xIn_{(1-x)}P$ NWs is of paramount importance to improve the TASE synthesis and growth processes, and to optimize the performance of the solar cells made therefrom.

The feasibility of off-axis electron holography for quantitative electrostatic potential mapping of GaAs NWs with different doping profiles was evaluated towards the end of thesis. Our preliminary holography results suggest that many of the observed phase shifts arise from thickness and geometry changes occurring along the NWs grown with a hybrid TASE/SAG approach. Thus, the analysis of the experimental holography data required the construction of simulation models to help single out the phase shifts induced by the incorporated dopants. However, due to the complexity and inhomogeneity of the analyzed NWs, there remain still many open questions and challenges to address. These could be addressed with more homogeneous GaAs nanowires with controlled shape and dopant incorporation and by verifying the holography results with other experimental techniques, such as Raman spectroscopy and CL-TEM. Moreover, the possibility to perform in-situ electrical measurements in the TEM can open new possibilities to study doping incorporation in TASE grown GaAs NWs.

In summary, this research project has addressed thoroughly two main topics, namely the growth of defect-free NWs and the effect of dopant incorporation by TASE and has brought up several key results for the future integration of NWs in electronic and photovoltaic devices. This has been possible by means of several TEM techniques, as TEM provides the spatial resolution to study the structure and properties of materials at the atomic level. We consider these results to play a key role in the advancement of III-V nanowires integration in electronic and optoelectronic devices and anticipate that TASE will open new paths for novel device architectures, although further research efforts are certainly needed to further optimize the quality and homogeneity of the NWs.

Bibliography

[1] Y. Taur and H. T. Ning, Fundamentals of Modern VLSI Devices (Cambridge University Press, 2009).

[2] W. Schockley, M. Sparks, and G. K. Teal, Phys. Rev. **83**, 151 (1951).

[3] W. Shockley, Bell Syst. Tech. J. **28**, 435 (1949).

[4] U. Mishra and J. Singh, Semiconductor Device Physics and Design (Springer US, 2008).

[5] G. E. Moore, Electronics **38**, 1 (1965).

[6] S. E. Thompson and S. Parthasarathy, Mater. Today **9**, 20 (2006).

[7] C. A. Mack, IEEE Trans. Semicond. Manuf. **24**, 202 (2011).

[8] D. Bishop, Bell Labs Tech. J. **10**, 23 (2005).

[9] H. N. Khan, D. A. Hounshell, and E. R. H. Fuchs, Nat. Electron. **1**, (2018).

[10] M. Schulz, Nature **399**, 729 (1999).

[11] M. T. Bohr, R. S. Chau, T. Ghani, and K. Mistry, IEEE Spectr. **44**, 29 (2007).

[12] N. S. Kim, T. Austin, D. Baauw, T. Mudge, K. Flautner, J. S. Hu, M. J. Irwin, M. Kandemir, and V. Narayanan, Computer (Long. Beach. Calif). **36**, 68 (2003).

[13] D. A. Muller, T. Sorsch, S. Moccio, F. H. Baumann, K. Evans-Lutterodt, and G. Timp, Nature **399**, 758 (1999).

[14] J. D. Meindl, Comput. Sci. Eng. **5**, 20 (2003).

[15] S. Krishnan, S V Garimella, G. M. Chrysler, and R V Mahajan, IEEE Trans. Adv. Packag. **30**, 462 (2007).

[16] P. S. Peercy, Nature **406**, 1023 (2014).

[17] I. L. Markov, Nature **512**, 147 (2014).

[18] S. Borkar, IEEE Micro **19**, 23 (1999).

[19] M. Mayberry, Enabling Breakthroughs In Technology (2011).

[20] M. Rozer and H. Ritchie, OurWorldInData.Org (2018).

[21] H. Riel, L.-E. Wernersson, M. Hong, and J. a. del Alamo, MRS Bull. **39**, 668 (2014).

[22] A. C. Seabaugh and Q. Zhang, Proc. IEEE **98**, 2095 (2010).

[23] A. M. Ionescu and H. Riel, Nature **479**, 329 (2011).

[24] J. A. del Alamo, Nature **479**, 317 (2011).

[25] R. W. Keyes, Reports Prog. Phys. **68**, 2701 (2005).

[26] K. P. Cheung, in Proc. 2010 Int. Symp. VLSI Technol. Syst. Appl. (2010), pp. 72–73.

[27] W. Y. Choi, B. Park, J. D. Lee, and T. K. Liu, IEEE Electron Device Lett. **28**, 743 (2007).

[28] J. Singh, K. Ramakrishnan, S. Mookerjea, S. Datta, N. Vijaykrishnan, and D. Pradhan, IEEE 181 (2010).

[29] J. E. Cohen, World Population in 2050: Assessing the Projections (2002).

[30] C. Frei, R. Whitney, H.-W. Schiffer, K. Rose, D. A. Rieser, A. Al-Qahtani, and P. Thomas, World Energy Scenarios: Composing Energy Futures to 2050 (2013).

[31] P. M. Cox, R. A. Betts, C. D. Jones, and S. A. Spall, Nature **408**, 184 (2000).

[32] U. Shahzad, Durreesamin J. **1**, 1 (2015).

[33] T. L. Root, J. T. Price, K. R. Hall, and S. H. Schneider, Nature **421**, 57 (2003).

[34] N. R. Golledge, D. E. Kowalewski, T. R. Naish, R. H. Levy, C. J. Fogwill, and E. G. W. Gasson, Nature **526**, 421 (2015).

[35] L. Capuano, International Energy Outlook 2018 (IEO2018) (2018).

[36] S. Zeng, Y. Liu, C. Liu, and X. Nan, Renew. Sustain. Energy Rev. **74**, 860 (2017).

[37] T. D. Lee and A. U. Ebong, Renew. Sustain. Energy Rev. **70**, 1286 (2017).

[38] L. Perdigo, P. Caprioglio, and D. Neher, Energy Environ. Sci. **10**, 1530 (2017).

[39] Y. Xu, T. Gong, and J. N. Munday, Sci. Rep. **5**, 1 (2015).

[40] S. Rühle, Sol. Energy **130**, 139 (2016).

[41] J. R. Hauser and P. M. Dunbar, IEEE Trans. Electron Devices **24**, 305 (1977).

[42] P. Kowalczewski, L. Redorici, A. Bozzola, and L. C. Andreani, J. Opt. **18**, 1 (2016).

[43] F. Dimroth, M. Grave, P. Beutel, U. Fiedeler, C. Karcher, T. N. D. Tibbits, E. Oliva, G. Siefer, M. Schachtner, A. Wekkeli, A. W. Bett, R. Krause, M. Piccin, N. Blanc, C. Drazek,

E. Guiot, B. Ghyselen, T. Salvetat, A. Tauzin, T. Signamarcheix, A. Dobrich, T. Hannappel, and K. Schwarzburg, Prog. Photovoltaics Res. Appl. **22**, 277 (2014).

[44] I. Vurgaftman and J. R. Meyer, J. Appl. Phys. **89**, 5815 (2001).

[45] K. Tomioka, T. Tanaka, S. Hara, K. Hiruma, and T. Fukui, IEEE J. Sel. Top. Quantum Electron. **17**, 1112 (2011).

[46] H. Schmid, K. E. Moselund, M. T. Björk, M. Richter, H. Ghoneim, C. D. Bessire, and H. Riel, in 69th Device Res. Conf. (2011), pp. 181–182.

[47] B. Ganjipour, J. Wallentin, M. T. Borgström, L. Samuelson, and C. Thelander, ACS Nano **6**, 3109 (2012).

[48] A. W. Dey, B. M. Borg, B. Ganjipour, M. Ek, K. a. Dick, E. Lind, C. Thelander, and L. E. Wernersson, IEEE Electron Device Lett. **34**, 211 (2013).

[49] X. Zhao, A. Vardi, and J. A. del Alamo, in 2014 IEEE Int. Electron Devices Meet. (2014), p. 25.5.1-25.5.4.

[50] E. Memisevic, J. Svensson, M. Hellenbrand, E. Lind, and L.-. Wernersson, in *2016 IEEE Int. Electron Devices Meet.* (2016), p. 19.1.1-19.1.4.

[51] M. T. Borgström, J. Wallentin, M. Heurlin, S. Fält, P. Wickert, J. Leene, M. H. Magnusson, K. Deppert, and L. Samuelson, IEEE J. Sel. Top. Quantum Electron. **17**, 1050 (2011).

[52] A. Slade and V. Garboushian, 27 . 6 % Efficient Silicon Concentrator Solar Cells for Mass Production (2015).

[53] J. Zhu, Z. Yu, G. F. Burkhard, C.-M. Hsu, S. T. Connor, Y. Xu, Q. Wang, M. McGehee, S. Fan, and Y. Cui, Nano Lett. **9**, 279 (2009).

[54] E. Garnett and P. Yang, Nano Lett. **10**, 1082 (2010).

[55] F. Glas, Phys. Rev. B **74**, 1 (2006).

[56] H. Ye, P. Lu, Z. Yu, Y. Song, D. Wang, and S. Wang, Nano Lett. **9**, 1921 (2009).

[57] M. T. Borgstr, M. H. Magnusson, F. Dimroth, G. Siefer, H. Oliver, H. Riel, S. Member, H. Schmid, S. Wirths, M. Bj, S. Member, W. Peijnenburg, M. Vijver, M. Tchernycheva, and V. Piazza, IEEE J. Photovoltaics **8**, 733 (2018).

[58] N. Anttu, V. Dagytė, X. Zeng, G. Otnes, and M. Borgström, Nanotechnology **28**, 205203 (2017).

[59] R. Ferrini, G. Guizzetti, M. Patrini, A. Parisini, L. Tarricone, and B. Valenti, Eur. Phys. J. B **27**, 449 (2002).

[60] F. Ishizaka, K. Ikejiri, K. Tomioka, and T. Fukui, Jpn. J. Appl. Phys. **52**, 1 (2013).

[61] Y. Özen, N. Akin, B. Kinaci, and S. Özçelik, Sol. Energy Mater. Sol. Cells **137**, 1 (2015).

[62] G. E. Cirlin, V. G. Dubrovskii, I. P. Soshnikov, N. V. Sibirev, Y. B. Samsonenko, a. D.

Bouravleuv, J. C. Harmand, and F. Glas, Phys. Status Solidi - Rapid Res. Lett. **3**, 112 (2009).

[63] D. Spirkoska, J. Arbiol, A. Gustafsson, S. Conesa-Boj, F. Glas, I. Zardo, M. Heigoldt, M. H. Gass, a. L. Bleloch, S. Estrade, M. Kaniber, J. Rossler, F. Peiro, J. R. Morante, G. Abstreiter, L. Samuelson, and A. Fontcuberta I Morral, Phys. Rev. B - Condens. Matter Mater. Phys. **80**, 1 (2009).

[64] K. L. Kavanagh, Semicond. Sci. Technol. **25**, 1 (2010).

[65] C. Thelander, P. Agarwal, S. Brongersma, J. Eymery, L. F. Feiner, A. Forchel, M. Scheffler, W. Riess, B. J. Ohlsson, U. Goesele, and L. Samuelson, Mater. Today **9**, 28 (2006).

[66] S. L. Chen, W. M. Chen, F. Ishikawa, and I. A. Buyanova, Sci. Rep. **5**, 1 (2015).

[67] A. M. Sanchez, J. A. Gott, H. A. Fonseka, Y. Zhang, H. Liu, and R. Beanland, Nano Lett. **18**, 3081 (2018).

[68] W. T. Read, *Dislocations In Crystals* (Nabu Press, 2011).

[69] J. Johansson, L. S. Karlsson, C. Patrik T. Svensson, T. Mårtensson, B. a. Wacaser, K. Deppert, L. Samuelson, and W. Seifert, Nat. Mater. **5**, 574 (2006).

[70] Z. Su, C. Dickinson, Y. Wan, Z. Wang, Y. Wang, and W. Zhou, CrystEngComm **12**, 2793 (2010).

[71] S. Bouchoule and P. Roca, Nat. Commun. **5**, 1 (2014).

[72] E. Lind, E. Memisevic, A. W. Dey, and L.-E. Wernersson, J. ELECTRON DEVICE Soc. **3**, 96 (2015).

[73] C. Song, J. Wang, W. Lin, H. Mao, Q. Zhao, P. Yang, and H. Xing, J. Appl. Phys. **114**, 113704 (2013).

[74] M. Aghaeipour, N. Anttu, G. Nylund, and A. Berg, Opt. Express **23**, 1559 (2015).

[75] D. Cohen and C. B. Carter, J. Microsc. **208**, 84 (2002).

[76] J. Bolinsson, The Crystal Structure of III-V Semiconductor Nanowires: Growth and Characterization, 2010.

[77] H. Choi, in Semicond. Nanostructures Optoelectron. Devices, edited by G. C. Yi (Springer-Verlag Berlin Heidelberg, 2012), pp. 1–36.

[78] J. Wang, S. R. Plissard, M. A. Verheijen, L.-F. Feiner, A. Cavalli, and E. P. A. M. Bakkers, Nano Lett. **13**, 3802 (2013).

[79] U. Krishnamachari, M. Borgstrom, B. J. Ohlsson, N. Panev, L. Samuelson, W. Seifert, M. W. Larsson, and L. R. Wallenberg, Appl. Phys. Lett. **85**, 2077 (2004).

[80] V. T. Renard, M. Jublot, P. Gergaud, P. Cherns, D. Rouchon, A. Chabli, and V. Jousseaume, Nat. Nanotechnol. **4**, 654 (2009).

[81] J. E. Allen, E. R. Hemesath, D. E. Perea, J. L. Lensch-falk, Z. Y. Li, F. Yin, M. H. Gass, P. Wang, A. L. Bleloch, R. E. Palmer, and L. J. Lauhon, Nat. Nanotechnol. **3**, 1 (2008).

[82] J. B. Hannon, S. Kodambaka, F. M. Ross, and R. M. Tromp, Nature **440**, 69 (2006).

[83] M. de la Mata, C. Magen, P. Caroff, and J. Arbiol, Nano Lett. **14**, 6614 (2014).

[84] M. De La Mata, C. Magen, J. Gazquez, M. I. B. Utama, M. Heiss, S. Lopatin, F. Furtmayr, C. J. Fernández-Rojas, B. Peng, J. R. Morante, R. Rurali, M. Eickhoff, A. Fontcuberta I Morral, Q. Xiong, and J. Arbiol, Nano Lett. **12**, 2579 (2012).

[85] M. T. Borgstrom, M. A. Verheijen, I. George, T. de Smet, and E. P. A. Bakkers, Nanotechnology **17**, 4010 (2006).

[86] M. T. Björk, B. J. Ohlsson, T. Sass, A. I. Persson, C. Thelander, M. H. Magnusson, K. Deppert, L. R. Wallenberg, L. Samuelson, B. J. Ohlsson, T. Sass, A. I. Persson, C. Thelander, and M. H. Magnusson, Appl. Phys. Lett. **80**, 1058 (2002).

[87] Y. Wu, R. Fan, and P. Yang, Nano Lett. **2**, 83 (2002).

[88] M. S. Gudiksen, L. J. Lauhon, J. Wang, D. C. Smith, and C. M. Lieber, Nature **415**, 617 (2002).

[89] F. Qian, Y. Li, S. Gradec, and C. M. Lieber, Nano Lett. **4**, 1975 (2004).

[90] R. S. Wagner and W. C. Ellis, Appl. Phys. Lett. **4**, 89 (1964).

[91] K. Hiruma, M. Yazawa, T. Katsuyama, K. Ogawa, K. Haraguchi, M. Koguchi, H. Kakibayashi, K. Hiruma, M. Yazawa, T. Katsuyama, K. Ogawa, K. Haraguchi, and M. Koguchi, J. Appl. Phys. **77**, 447 (1995).

[92] T. Akiyama, K. Sano, K. Nakamura, and T. Ito, Jpn. J. Appl. Phys. **45**, 275 (2006).

[93] X. Li, J. Ni, and R. Zhang, Sci. Rep. **7**, 15029 (2017).

[94] S. A. Fortuna, J. Wen, I. S. Chun, and X. Li, Nano Lett. **8**, 4421 (2008).

[95] S. A. Fortuna and X. Li, IEEE Electron Device Lett. **30**, 593 (2009).

[96] X. Zhang, J. Zou, M. Paladugu, Y. Guo, Y. Wang, Y. Kim, H. J. Joyce, Q. Gao, H. H. Tan, and C. Jagadish, Small **5**, 366 (2009).

[97] S. A. Dayeh, E. T. Yu, and D. Wang, Nano Lett. **7**, 2486 (2007).

[98] M. A. Verheijen, G. Immink, T. De Smet, M. T. Borgstro, and E. P. A. M. Bakkers, J. Am. Chem. Soc. **128**, 1353 (2006).

[99] C. Soci, X. Bao, D. P. R. Aplin, and D. Wang, Nano Lett. **12**, (8AD).

[100] H. J. Joyce, Q. Gao, H. H. Tan, C. Jagadish, Y. Kim, M. a. Fickenscher, S. Perera, T. B. Hoang, L. M. Smith, H. E. Jackson, J. M. Yarrison-Rice, X. Zhang, and J. Zou, Adv. Funct. Mater. **18**, 3794 (2008).

[101] P. Caroff, K. a. Dick, J. Johansson, M. E. Messing, K. Deppert, and L. Samuelson, Nat.

Nanotechnol. **4**, 50 (2009).

[102] M. Heiss, S. Conesa-Boj, J. Ren, H.-H. Tseng, A. Gali, A. Rudolph, E. Uccelli, F. Peiró, J. R. Morante, D. Schuh, E. Reiger, E. Kaxiras, J. Arbiol, and A. Fontcuberta i Morral, Phys. Rev. B **83**, 045303 (2011).

[103] G. Dewey, J. Boardman, J. M. Fastenau, J. Kavalieros, R. Kotlyar, W. K. Liu, D. Lubyshev, M. Metz, N. Mukherjee, R. Pillarisetty, M. Radosavljevic, H. W. Then, and R. Chau, IEEE **3**, 785 (2011).

[104] J. Motohisa, J. Noborisaka, J. Takeda, M. Inari, and T. Fukui, J. Cryst. Growth **272**, 180 (2004).

[105] J. Noborisaka, J. Motohisa, and T. Fukui, Appl. Phys. Lett. **86**, 1 (2005).

[106] J. Johansson and K. a. Dick, CrystEngComm **13**, 7175 (2011).

[107] Y. Watanabe, H. Hibino, S. Bhunia, K. Tateno, and T. Sekiguchi, Phys. E Low-Dimensional Syst. Nanostructures **24**, 133 (2004).

[108] N. Panev, A. I. Persson, N. Sköld, and L. Samuelson, Appl. Phys. Lett. **83**, 2238 (2003).

[109] K. Tomioka, J. Motohisa, S. Hara, and T. Fukui, Nano Lett. **8**, 3475 (2008).

[110] K. Tomioka, Y. Kobayashi, J. Motohisa, S. Hara, and T. Fukui, Nanotechnology **20**, 145302 (2009).

[111] K. Tomioka, J. Motohisa, and T. Fukui, Int. Symp. VLSI Technol. Syst. Appl. Proc. **111**, 3 (2015).

[112] K. Tomioka and T. Fukui, Appl. Phys. Lett. **104**, 2012 (2014).

[113] K. Tomioka, M. Yoshimura, and T. Fukui, Nano Lett. **13**, 5822 (2013).

[114] K. Tomioka, M. Yoshimura, and T. Fukui, Symp. VLSI Technol. Dig. Tech. Pap. 47 (2012).

[115] M. Borg, H. Schmid, K. E. Moselund, G. Signorello, L. Gignac, J. Bruley, C. Breslin, P. Das Kanungo, P. Werner, and H. Riel, Nano Lett. **14**, 1914 (2014).

[116] M. Borg, H. Schmid, K. E. Moselund, D. Cutaia, and H. Riel, J. Appl. Phys. **117**, 144303 (2015).

[117] P. Das Kanungo, H. Schmid, M. T. Björk, L. M. Gignac, C. Breslin, J. Bruley, C. D. Bessire, and H. Riel, Nanotechnology **24**, 225304 (2013).

[118] P. Caroff, J. B. Wagner, K. a. Dick, H. a. Nilsson, M. Jeppsson, K. Deppert, L. Samuelson, L. R. Wallenberg, and L. E. Wernersson, Small **4**, 878 (2008).

[119] D. Cutaia, K. E. Moselund, B. Mattias, and H. Scmidt, Electron Devices Soc. **3**, (2015).

[120] H. Schmid, M. Borg, K. Moselund, L. Gignac, C. M. Breslin, J. Bruley, D. Cutaia, and H. Riel, Appl. Phys. Lett. **106**, 233101 (2015).

[121] K. Grens, Apiarium, *1625* (2015).

[122] A. van Leeuwenhoek, Philos. Trans. R. Soc. **22**, 509 (1700).

[123] L. Lambert and T. Mulvey, in edited by P. W. B. T.-A. in I. and E. P. Hawkes (Elsevier, 1996), pp. 2–62.

[124] R. Erni, M. D. Rossell, C. Kisielowski, and U. Dahmen, Phys. Rev. Lett. **102**, 96101 (2009).

[125] P. M. Petroff, J. Vac. Sci. Technol. **14**, 973 (1977).

[126] M. Hy, H. Bender, F. Houdellier, A. Claverie, and F. Hu, Phys. Rev. Lett. **100**, 1 (2008).

[127] K. Nomura, H. Ohta, K. Ueda, T. Kamiya, M. Hirano, and H. Hosono, Science (80-.). **300**, 1269 LP (2003).

[128] A. K. W. Chee, Sci. Rep. **8**, 5247 (2018).

[129] S. J. Pennycook, Scanning Vol. **30**, 287 (2008).

[130] G.-S. Park, Y. B. Kim, S. Y. Park, X. S. Li, S. Heo, M.-J. Lee, M. Chang, J. H. Kwon, M. Kim, U.-I. Chung, R. Dittmann, R. Waser, and K. Kim, Nat. Commun. **4**, 1 (2013).

[131] D. B. Williams and C. B. Carter, *The Transmission Electron Microscope* (2009).

[132] S. Rubanov and P. R. Munroe, J. Microsc. **214**, 213 (2004).

[133] O. Scherzer, J. Appl. Phys. **20**, 20 (1949).

[134] R. Erni, Aberration-Corrected Imaging in Transmission Electron Microscopy (IMPERIAL COLLEGE PRESS, 2010).

[135] R. F. Egerton, Ultramicroscopy **145**, 85 (2014).

[136] R. Erni and N. Browning, Transmission Electron Microscopy (2007).

[137] I. Lazi and E. G. T. Bosch, Analytical Review of Direct Stem Imaging Techniques for Thin Samples, 1st ed. (Elsevier Inc., 2017).

[138] S. J. Pennycook and P. D. Nellist, in Scanning Transm. Electron Microsc. (2011), pp. 91–116.

[139] G. Kothleitner, M. J. Neish, N. R. Lugg, S. D. Findlay, W. Grogger, F. Hofer, and L. J. Allen, Phys. Rev. Lett. **112**, 1 (2014).

[140] L. Jones, R. B. S. Lozano-perez, K. Baba-kishi, and P. D. Nellist, Microsc. Microanal. **21**, 1215 (2015).

[141] J. T. Held, K. I. Hunter, N. Dahod, B. Greenberg, D. Reifsnyder Hickey, W. A. Tisdale, U. Kortshagen, and K. A. Mkhoyan, ACS Appl. Nano Mater. **1**, 989 (2018).

[142] R. F. Egerton, Ultramicroscopy **107**, 575 (2007).

[143] M. Varela, S. D. Findlay, A. R. Lupini, H. M. Christen, A. Y. Borisevich, N. Dellby, O.

L. Krivanek, P. D. Nellist, M. P. Oxley, L. J. Allen, and S. J. Pennycook, Phys. Rev. Lett. **92**, 95502 (2004).

[144] M. D. Rossell, Q. M. Ramasse, S. D. Findlay, F. Rechberger, R. Erni, and M. Niederberger, ACS Nano **6**, 7077 (2012).

[145] S. J. Pennycook, M. Varela, A. R. Lupini, M. P. Oxley, and M. F. Chisholm, J. Electron Microsc. (Tokyo). **58**, 87 (2009).

[146] N. D. Browning, M. F. Chisholm, and S. J. Pennycook, Nature **366**, 143 (1993).

[147] F. S. Hage, R. J. Nicholls, J. R. Yates, D. G. McCulloch, T. C. Lovejoy, N. Dellby, O. L. Krivanek, K. Refson, and Q. M. Ramasse, Sci. Adv. **4**, eaar7495 (2018).

[148] D. Keller, S. Buecheler, P. Reinhard, F. Pianezzi, D. Pohl, A. Surrey, B. Rellinghaus, R. Erni, and A. N. Tiwari, Microsc. Microanal. **20**, 1246 (2014).

[149] J. A. Hachtel, A. R. Lupini, and J. C. Idrobo, Sci. Rep. **8**, 5637 (2018).

[150] P. A. Crozier, Ultramicroscopy **0**, 1 (2017).

[151] R. Egoavil, N. Gauquelin, G. T. Martinez, S. Van Aert, G. Van Tendeloo, and J. Verbeeck, Ultramicroscopy **147**, 1 (2014).

[152] O. L. Krivanek, T. C. Lovejoy, N. Dellby, T. Aoki, R. W. Carpenter, P. Rez, E. Soignard, J. Zhu, P. E. Batson, M. J. Lagos, R. F. Egerton, and P. A. Crozier, Nature **514**, 209 (2014).

[153] R. Egerton, Electron Energy-Loss Spectroscopy in the Electron Microscope, Springer U (Boston, MA, 2011).

[154] R. Senga and K. Suenaga, Nat. Commun. **6**, 7943 (2015).

[155] R. Erni and N. D. Browning, Ultramicroscopy **104**, 176 (2005).

[156] T. Malis, S. C. Cheng, and R. F. Egerton, J. Electron Microsc. Tech. **8**, 193 (2018).

[157] N. D. Browning, I. Arslan, R. Erni, and B. W. Reed, in Scanning Transm. Electron Microsc., edited by S. J. Pennycook and P. D. Nellist (Springer New York, 2011), pp. 659–688.

[158] J. Palisaitis, C.-L. Hsiao, M. Junaid, M. Xie, V. Darakchieva, J.-F. Carlin, N. Grandjean, J. Birch, L. Hultman, and P. O. Å. Persson, Phys. Status Solidi – Rapid Res. Lett. **5**, 50 (2010).

[159] a. M. Sanchez, R. Beanland, a. J. Papworth, P. J. Goodhew, and M. H. Gass, Appl. Phys. Lett. **88**, 1 (2006).

[160] L. H. G. Tizei, T. Chiaramonte, M. a Cotta, and D. Ugarte, Nanotechnology **21**, 295701 (2010).

[161] X. Kong, S. Albert, A. Bengoechea-Encabo, M. a Sanchez-Garcia, E. Calleja, A. Trampert, M. A. Sanchez-García, E. Calleja, and A. Trampert, Nanotechnology **23**, 485701 (2012).

[162] a. M. Sánchez, R. Beanland, M. H. Gass, a. J. Papworth, P. J. Goodhew, and M. Hopkinson, Phys. Rev. B - Condens. Matter Mater. Phys. **72**, 1 (2005).

[163] L. H. G. Tizei, T. Chiaramonte, M. A. Cotta, and D. Ugarte, Nanotechnology **21**, 1 (2010).

[164] I. Schubert, W. Sigle, P. A. van Aken, C. Trautmann, and M. E. Toimil-Molares, Nanoscale **7**, 4935 (2015).

[165] L. Gu, V. Srot, W. Sigle, C. Koch, P. van Aken, F. Scholz, S. B. Thapa, C. Kirchner, M. Jetter, and M. Rühle, Phys. Rev. B **75**, 195214 (2007).

[166] M. J. Lagos, A. Trügler, U. Hohenester, and P. E. Batson, Nature **543**, 529 (2017).

[167] B. Rafferty, S. J. Pennycook, and L. M. Brown, J. Electron Microsc. (Tokyo). **49**, 517 (2000).

[168] P. A. Midgley and R. E. Dunin-Borkowski, Nat. Mater. **8**, 271 (2009).

[169] M. I. Den Hertog, L. Rouviere, H. Schmid, D. Cooper, M. T. Björk, H. Riel, F. Dhalluin, P. Gentile, P. Ferret, F. Oehler, T. Baron, P. Rivallin, S. Karg, and W. Riess, J. Phys. Conf. Ser. **209**, (2010).

[170] D. Cooper, P. Rivallin, J. M. Hartmann, A. Chabli, and R. E. Dunin-Borkowski, J. Appl. Phys. **106**, (2009).

[171] D. Cooper, J. Phys. D. Appl. Phys. **49**, (2016).

[172] S. Yazdi, A. Berg, M. T. Borgström, T. Kasama, M. Beleggia, L. Samuelson, and J. B. Wagner, Small **11**, 2687 (2015).

[173] D. Cooper, J. Rouvière, and R. Dunin-borkowski, Microsc. Microanal. **20**, 254 (2014).

[174] M. I. Den Hertog, Nano Lett. **9**, 3837 (2009).

[175] L. Li, Z. Gan, M. R. Mccartney, H. Liang, H. Yu, W. Yin, Y. Yan, Y. Gao, J. Wang, and D. J. Smith, Adv. Mater. **26**, 1052 (2014).

[176] N. Shibata, S. D. Findlay, H. Sasaki, T. Matsumoto, H. Sawada, Y. Kohno, S. Otomo, R. Minato, and Y. Ikuhara, Sci. Rep. **5**, 2 (2015).

[177] R. E. Dunin-Borkowski and T. Kasama, in Hologr. - Differ. Fields Appl., edited by F. Monroy, InTech Ope (2011), pp. 53–80.

[178] M. J. Hÿtch, E. Snoeck, and R. Kilaas, Ultramicroscopy **74**, 131 (1998).

[179] E. Völkl and H. Lichte, Ultramicroscopy **32**, 177 (1990).

[180] C. Ton-That and M. R. Phillips, in Woodhead Publ. Ser. Electron. Opt. Mater., edited by J. Arbiol and Q. B. T.-S. N. Xiong (Woodhead Publishing, 2015), pp. 393–407.

[181] M. Hetzl, M. Kraut, J. Winnerl, L. Francaviglia, M. Döblinger, S. Matich, A. Fontcuberta i Morral, and M. Stutzmann, Nano Lett. **16**, 7098 (2016).

[182] K. Burke, J. Chem. Phys. **136**, 150901 (2012).

[183] J. Hafner, J. Comput. Chem. **29**, 2044 (2008).

[184] J. P. Perdew, Int. J. Quantum Chem. **28**, 497 (1985).

[185] S. Bernal, F. J. Botana, J. J. Calvino, C. López-Cartes, J. A. Pérez-Omil, and J. M. Rodríguez-Izquierdo, Ultramicroscopy **72**, 135 (1998).

[186] U. of C. J. A. Pérez-Omil, Ph.D. Thesis, 1994.

[187] P. Hohenberg and W. Kohn, Phys. Rev. **136**, B864 (1964).

[188] P. Agrawal, J. Guo, P. Yu, D. Passerone, R. Erni, and M. D. Rossell, Phys. Rev. B **94**, 1 (2016).

[189] M. Rossell, P. Agrawal, A. Borgschulte, C. Hébert, D. Passerone, and R. Erni, Chem. Mater. **27**, 3593 (2015).

[190] Y. Zhang, C. Guerra, I. Utke, J. Michler, P. Agrawal, M. Rossell, and R. Erni, Chem. Mater. **29**, 2232 (2017).

[191] W. Kohn and L. J. Sham, Phys. Rev. **140**, A1133 (1965).

[192] J. P. Perdew, K. Burke, and M. Ernzerhof, Phys. Rev. Lett. **77**, 3865 (1996).

[193] A. V. Krukau, O. A. Vydrov, A. F. Izmaylov, and G. E. Scuseria, J. Chem. Phys. **125**, 224106 (2006).

[194] K. Tomioka, K. Ikejiri, T. Tanaka, J. Motohisa, S. Hara, K. Hiruma, and T. Fukui, J. Mater. Res. **26**, 2127 (2011).

[195] K. Hiruma, M. Yazawa, T. Katsuyama, K. Ogawa, K. Haraguchi, M. Koguchi, and H. Kakibayashi, J. Appl. Phys. **77**, 447 (1995).

[196] T. Nishinaga, J. Cryst. Growth **237–239**, 1410 (2002).

[197] L. Jastrzebski, J. F. Corboy, J. T. McGinn, and J. R. Pagliaro, J. Electrochem. Soc. **130**, 1571 (1983).

[198] S. N. and T. N. and M. T. and Hidehumi Mori, Jpn. J. Appl. Phys. **34**, L1432 (1995).

[199] H. Asai and S. Ando, J. Electrochem. Soc. **132**, 2445 (1985).

[200] H. Asai, J. Cryst. Growth **80**, 425 (1987).

[201] K. Tomioka, P. Mohan, J. Noborisaka, S. Hara, J. Motohisa, and T. Fukui, J. Cryst. Growth **298**, 644 (2007).

[202] M. Borg, H. Schmid, J. Gooth, M. D. Rossell, D. Cutaia, M. Knoedler, N. Bologna, S. Wirths, K. E. Moselund, and H. Riel, ACS Nano **11**, 2554 (2017).

[203] F. Ernst and P. Pirouz, J. Appl. Phys. **64**, 4526 (1988).

[204] Y. Ping Wang, J. Stodolna, M. Bahri, J. Kuyyalil, T. Nguyen Thanh, S. Almosni, R. Bernard, R. Tremblay, M. Da Silva, A. Létoublon, T. Rohel, K. Tavernier, L. Largeau, G. Patriarche, A. Le Corre, A. Ponchet, C. Magen, C. Cornet, and O. Durand, Appl. Phys.

Lett. **107**, 191603 (2015).

[205] A. Beyer, I. Németh, S. Liebich, J. Ohlmann, W. Stolz, and K. Volz, J. Appl. Phys. **109**, 83529 (2011).

[206] C. Junesand, H. Kataria, W. Metaferia, N. Julian, Z. Wang, Y.-T. Sun, J. Bowers, G. Pozina, L. Hultman, and S. Lourdudoss, Opt. Mater. Express **3**, 1960 (2013).

[207] K. Zaima, R. Hashimoto, M. Ezaki, M. Nishioka, and Y. Arakawa, J. Cryst. Growth **310**, 4843 (2008).

[208] M. Deura, Y. Kondo, M. Takenaka, S. Takagi, Y. Nakano, and M. Sugiyama, J. Cryst. Growth **312**, 1353 (2010).

[209] H. Yoshida, K. Ikejiri, T. Sato, S. Hara, K. Hiruma, J. Motohisa, and T. Fukui, J. Cryst. Growth **312**, 52 (2009).

[210] J. N. Shapiro, A. Lin, C. Ratsch, and D. L. Huffaker, Nanotechnology **24**, 475601 (2013).

[211] M. J. L. Sourribes, I. Isakov, M. Panfilova, H. Liu, and P. A. Warburton, Nano Lett. **14**, 1643 (2014).

[212] J. Wallentin, M. Ek, L. R. Wallenberg, L. Samuelson, and M. T. Borgström, Nano Lett. **12**, 151 (2012).

[213] A. D. Schricker, F. M. Davidson III, R. J. Wiacek, and B. A. Korgel, Nanotechnology **17**, 2681 (2006).

[214] A. M. Sanchez, Y. Zhang, E. W. Tait, N. D. M. Hine, H. Liu, and R. Beanland, Nano Lett. **17**, 2454 (2017).

[215] C. Li, Y. Wu, A. R. Lupini, A. Mouti, J. Poplawsky, W. Yin, N. Paudel, M. Al-Jassim, Y. Yan, and T. J. Pennycook, Microsc. Microanal. **19**, 334 (2013).

[216] a. Mouti, C. Li, and S. J. Pennycook, Microsc. Microanal. **18**, 1332 (2012).

[217] L. Li, Z. Gan, M. R. Mccartney, H. Liang, H. Yu, Y. Gao, J. Wang, and D. J. Smith, 1 (2013).

[218] Y. Arroyo Rojas Dasilva, R. Kozak, R. Erni, and M. D. Rossell, Ultramicroscopy **176**, 11 (2016).

[219] N. W. Ashcroft and D. N. Mermin, Solid State Physics (Cengage Learning, 1976).

[220] D. Prendergast, J. C. Grossman, and G. Galli, J. Chem. Phys. **123**, 14501 (2005).

[221] A. C. Meng, J. Cheng, and M. Sprik, J. Phys. Chem. B **120**, 1928 (2016).

[222] M. Gibertini and N. Marzari, Nano Lett. **15**, 6229 (2015).

[223] J. Lin, M. Wu, M. Jou, C. Chang, C. Chen, and B. Lee, J. Appl. Phys. **74**, 1781 (1993).

[224] A. Berg, F. Lenrick, N. Vainorius, J. P. Beech, L. R. Wallenberg, and M. T. Borgström, Nanotechnology **26**, 1 (2015).

[225] D. S. Oliveira, L. H. G. Tizei, A. Li, T. L. Vasconcelos, C. A. Senna, B. S. Archanjo, D. Ugarte, and M. A. Cotta, Nanoscale **7**, 12722 (2015).

[226] C. P. T. Svensson, T. Mårtensson, J. Trägårdh, C. Larsson, M. Rask, D. Hessman, L. Samuelson, and J. Ohlsson, Nanotechnology **19**, 1 (2008).

[227] D. Jacobsson, J. M. Persson, D. Kriegner, T. Etzelstorfer, J. Wallentin, J. B. Wagner, J. Stangl, L. Samuelson, K. Deppert, and M. T. Borgström, Nanotechnology **235601**, 1 (2012).

[228] N. Kornienko, D. D. Whitmore, Y. Yu, S. R. Leone, and P. Yang, ACS Nano **9**, 3951 (2015).

[229] G. Otnes, M. Heurlin, X. Zeng, and M. T. Borgström, Nano Lett. **17**, 702 (2017).

[230] R. E. Algra, M. A. Verheijen, M. T. Borgström, L.-F. Feiner, G. Immink, W. J. P. van Enckevort, E. Vlieg, and E. P. A. M. Bakkers, Nature **456**, 369 (2008).

[231] I. Regolin, C. Gutsche, A. Lysov, K. Blekker, Z. A. Li, M. Spasova, W. Prost, and F. J. Tegude, J. Cryst. Growth **315**, 143 (2011).

[232] C. Gutsche, I. Regolin, K. Blekker, A. Lysov, W. Prost, and F. J. Tegude, J. Appl. Phys. **105**, (2009).

[233] T. Haggren, J. P. Kakko, H. Jiang, V. Dhaka, T. Huhtio, and H. Lipsanen, 14th IEEE Int. Conf. Nanotechnology, IEEE-NANO 2014 825 (2014).

[234] A. Berg, P. Caroff, N. Shahid, M. N. Lockrey, X. Yuan, M. T. Borgström, H. H. Tan, and C. Jagadish, Nano Res. **10**, 672 (2017).

[235] O. Salehzadeh, C. He, W. Benyon, and A. J. SpringThorpe, J. Cryst. Growth **445**, 110 (2016).

[236] X. Kong, S. Albert, A. Bengoechea-Encabo, M. a Sanchez-Garcia, E. Calleja, A. Trampert, M. A. Sanchez-García, E. Calleja, and A. Trampert, Nanotechnology **23**, 1 (2012).

[237] D. Auvergne, P. Merle, and H. Mathieu, Solid State Commun. **21**, 437 (1977).

[238] I. Vurgaftman, J. R. Meyer, and L. R. Ram-Mohan, J. Appl. Phys. **89**, 5815 (2001).

[239] M. D. Dawson and G. Duggan, Phys. Rev. B **47**, 12598 (1993).

[240] B. Ketterer, E. Mikheev, E. Uccelli, and A. Fontcuberta I Morral, Appl. Phys. Lett. **97**, 1 (2010).

[241] M. Hetzl, M. Kraut, J. Winnerl, L. Francaviglia, M. Döblinger, S. Matich, A. Fontcuberta i Morral, and M. Stutzmann, Nano Lett. **16**, 7098 (2016).

[242] L. C. Su, S. T. Pu, G. B. Stringfellow, J. Christen, H. Selber, and D. Bimberg, J. Electron. Mater. **23**, 125 (1994).

[243] J. Wallentin, M. Ek, L. R. Wallenberg, L. Samuelson, K. Deppert, and M. T. Borgström, Nano Lett. **10**, 4807 (2010).

[244] P. Kruse, A. Rosenauer, and D. Gerthsen, Ultramicroscopy **96**, 11 (2003).

[245] D. Wolf, R. Hübner, T. Niermann, S. Sturm, P. Prete, N. Lovergine, B. Büchner, and A. Lubk, Nano Lett. **18**, 4777 (2018).

[246] H. Lichte and M. Lehmann, Reports Prog. Phys. **71**, 16102 (2007).

[247] A. Darbandi, J. C. McNeil, A. Akhtari-Zavareh, S. P. Watkins, and K. L. Kavanagh, Nano Lett. **16**, 3982 (2016).

[248] L. Z.-Y. Liu, D. V. S. Rao, M. J. Kappers, C. J. Humphreys, and D. Geiger, J. Phys. Conf. Ser. **209**, 12012 (2010).

[249] H. Yoshida, H. Kohno, S. Ichikawa, T. Akita, and S. Takeda, Mater. Lett. **61**, 3134 (2007).

[250] A. G. Cullis and R. Beanland, Microscopy of Semiconducting Materials (1999).

[251] P. Formanek and M. Kittler, Solid State Phenom. **108–109**, 603 (2005).

[252] M. R. McCartney and M. Gajdardziska-Josifovska, Ultramicroscopy **53**, 283 (1994).

[253] M. Gajdardziska-Josifovska, Interface Sci. **2**, 425 (1995).

[254] M. den Hertog, F. Donatini, R. McLeod, E. Monroy, C. Sartel, V. Sallet, and J. Pernot, Nanotechnology **29**, 25710 (2017).

[255] A. C. Twitchett, R. E. Dunin-Borkowski, R. J. Hallifax, R. F. Broom, and P. A. Midgley, J. Microsc. **214**, 287 (2004).

[256] P. K. Somodi, A. C. Twitchett-Harrison, P. A. Midgley, B. E. Kardynał, C. H. W. Barnes, and R. E. Dunin-Borkowski, Ultramicroscopy **134**, 160 (2013).

[257] P. F. Fazzini, P. G. Merli, G. Pozzi, and F. Ubaldi, Phys. Rev. B **72**, 85312 (2005).

[258] L. Houben, M. Luysberg, and T. Brammer, Phys. Rev. B **70**, 165313 (2004).

[259] M. Beleggia, P. F. Fazzini, P. G. Merli, and G. Pozzi, Phys. Rev. B **67**, 45328 (2003).

[260] D. Cooper, A. C. Twitchett-Harrison, P. A. Midgley, and R. E. Dunin-Borkowski, J. Appl. Phys. **101**, 94508 (2007).

[261] R. E. Dunin-Borkowski, S. B. Newcomb, T. Kasama, M. R. McCartney, M. Weyland, and P. A. Midgley, Ultramicroscopy **103**, 67 (2005).

[262] D. Cooper, J. Barnes, J.-M. Hartmann, and F. Bertin, Off-Axis Electron Holography of Si Semiconductors Prepared Using FIB Milling (2010).

[263] J. Gooth, V. Schaller, S. Wirths, H. Schmid, M. Borg, N. Bologna, S. Karg, and H. Riel, Appl. Phys. Lett. **110**, 83105 (2017).

Curriculum Vitae

Nicolas Bologna, Doctoral scientist

Birth date: 17/11/1988
Nationality: Italian
Address: 6 Wehntalerstrasse, Zürich, ZH 8057
Mobile: +41 (0)71 865 53 34
E-mail: nicolas.bologna6@gmail.com
Website: https://www.linkedin.com/in/Nicolas.Bologna
https://scholar.google.com/Nicolas.Bologna

SUMMARY A hard-working, creative and ambitious doctoral scientist with a deep knowledge on several technological fields and a strong willingness to contribute to the development of engineering product.

WORKING EXPERIENCE

June 2015 - May 2019 **Empa/ IBM Research** **Dübendorf/Rüschlikon, ZH, Switzerland**
R&D Project Engineer

- Development of joint project between Empa's Electron Microscopy Center and IBM's M.I.N.D. group
- Characterization of III-V semiconductor nanowires for electronic and optoelectronic devices
- Investigation of crystal structures, defects and the effect induced on electrical and optical properties by TEM and modeling techniques
- Presenter at international scientific conferences (Switzerland, France, Australia)
- Attendance of different digital solution symposia (Blockchain, FinTech, IoT, Cryptocurrency)

Additional references: Dr. Marta D. Rossell, Senior Scientist EMC
Dr. Heike Riel, S&T Department Head

February 2014 - December 2014 **Mubadala Investment Company – Masdar Institute** **Abu Dhabi, UAEAD, U.A.E**
Assistant researcher

- Characterization of carbon nanotube sheets for desalination, aerospace and Oil&Gas industry
- Study of the surface morphology and dielectric properties by AFM and spectroscopy techniques
- Publications in peer-reviewed journals on the mathematical modeling of nanoscale interactions
- Project funded by ADNOC (government institution) and Lockheed Martin (Aeronautics)

Side activity:

- I was temporarily hired by Innovation Norway (one of the group's investors) as a Staff Member at the 30th Abu Dhabi International Petroleum Exhibition and Conference (ADIPEC 2014) from November 10th to November 13th.

EDUCATION

June 2015 - May 2019

École Polytechnique Fédérale de Lausanne (EPFL) **Lausanne, VD, Switzerland**
Doctoral school of Materials Science and Engineering
PhD Thesis: Growth of III-V nanostructures in 3D templates and their characterization

- Member of the Laboratory of Semiconductor Materials led by Prof. Dr. Anna Fontcuberta i Morral
- Attendance and successful examination of core course “Crystal growth by epitaxy”
- Attendance in 2016 at the Arizona State University (ASU) in Phoenix (U.S.A.) of the Winter School of Leroy Eyring Center for Solid State Science for trainings and networking
- Visiting student in 2016 at the Istitut Catala de Nanociencia i Nanotecnologia (ICN2) in Barcelona (Spain) at the Advanced Electron Nanoscopy group for atomic-modeling of semiconductor materials

Side activities:

- Acquired notions and analytical skills in “Economics of innovation and technological change” course
- Acquired notions and analytical skills in “Risk and Insurance Economics” course at ETHZ
- Member of “The Consulting Society” and “The Graduate Consulting Club”: solving business cases on a wide range of industries

October 2012 - December 2014

Polytechnic University of Milan (PoliMi) **Milano, Mi, Italy**
Master of Science in Materials Engineering, Nanotechnology and Industrial Processes
M.Sc. Thesis: Characterization and application of carbon nanotube sheets as electrodes for capacitive deionization

- Acquired analytical and soft skills to develop projects for new materials technologies
- GPA: 3.73/4 (28/30) with final graduation score (107/110) in the top 5% over 100 students of the 2012/2013 academic year
- The M.Sc. thesis was developed at Mubadala Investment Company – Masdar Institute in UAE

October 2007 - October 2012

University Milano-Bicocca (UNIMIB) **Milano, Mi, Italy**
Bachelor of Science in Materials Science
B.Sc. Thesis: Investigation and application of inorganic gallium oxides for telecommunication

- Study of core courses concerning physics, chemistry and mathematics to be applied to material technologies
- Active participation in university events and career fairs

COMMUNICATION AND PROGRAMMING SKILLS

- Italian Level: mother tongue
- English Level: fluent C1 (certified)
- German Level: intermediate B1 (attending semi-intensive Deutschkurs B2.1 in Zürich)
- Spanish Level: basic A2

- Microsoft Office: Word, PowerPoint, Excel (certified by PWC), OneNote, Access
- Programming: C++, MATLAB, Python, Stem_Cell for atomistic simulation and modeling
- Advanced data analytics: OriginLab, Excel and Tableau (financial modeling tools included)

SCHOLARSHIPS AND AWARDS

- Winner of European Microscopy Society (EMS) scholarship (April 2017)
- Winner of one of the 79 (out of over 1500 candidates) “Thesis Abroad Scholarship 2014” distributed by Polytechnic University of Milan to innovative Master of Science thesis (December 2013)

Ce document a été imprimé au Centre d’impression EPFL,
imprimerie climatiquement neutre, certifiée myClimate.